$K^+\Sigma^-$ Photoproduction at Forward Angles at the BGOOD Experiment

Dissertation
zur
Erlangung des Doktorgrades (Dr. rer. nat.)
der
Mathematisch-Naturwissenschaftlichen Fakultät
der
Rheinischen Friedrich-Wilhelms-Universität Bonn

vorgelegt von
Johannes Groß
aus
Troisdorf

Bonn, 2025

Angefertigt mit Genehmigung der Mathematisch-Naturwissenschaftlichen Fakultät
der Rheinischen Friedrich-Wilhelms-Universität Bonn

Gutachter/Betreuer:	Prof. Dr. Hartmut Schmieden
Gutachter:	Prof. Dr. Klaus Desch
Tag der Promotion:	22.12.2025
Erscheinungsjahr:	2026

Abstract

Already when the quark model was introduced in 1964, Gell-Mann suggested that hadrons might be composed of more than three quarks. This idea is experiencing a renaissance during the last decade. In 2016, the $\Lambda(1405)$ hyperon has finally been assigned a $\bar{K}N$ - meaning five-quark - molecular-like structure by the Particle Data Group, based on overwhelming evidence from experiment and theory. Since 2015, LHCb unambiguously revealed the pentaquarks $P_c(4312)^+$, $P_c(4440)^+$ and $P_c(4457)^+$ in the charm sector, which are located close to production thresholds of $\Sigma_c\bar{D}$ states. The same model that predicted those pentaquarks also predicts analogous structures in the strange sector such as the $N^*(2030)$ resonance, which is thought to be a dynamically-generated $K^*\Sigma$ state. For the reaction $\gamma n \to K^0\Sigma^0$, this state is expected to magnify the constructive interference of amplitudes driven by intermediate $K^*\Lambda$ and $K^*\Sigma$ channels and thus giving rise to a resonant peak in the spectrum just below the $K^*\Sigma$ threshold. In the past, corresponding differential cross section data has been measured at BGOOD but no firm conclusion was possible regarding a peak around the $K^*\Sigma$ threshold due to limited statistics. Similar structures might occur in the charge-conjugate channel $\gamma n \to K^+\Sigma^-$, providing the motivation for a measurement of this reaction using the BGOOD experiment at ELSA.

The differential cross section of the reaction $\gamma n \to K^+\Sigma^-$ has been measured in an angular range of $\cos(\theta_{\mathrm{CM}}) > 0.9$ at centre-of-mass energies ranging from threshold up to $W = 1\,942\,\mathrm{MeV}$. Combining this dataset with LEPS data at higher energies reveals a prominent peak located at $M = 1\,924\,\mathrm{MeV}$ with a width of $\Gamma = 72\,\mathrm{MeV}$. This is in good accordance with predictions of a K^+K^-N bound state just below the K^+K^-N threshold. The LEPS data shows a further jump in the differential cross section at $W = 2\,040\,\mathrm{MeV}$, which tends to agree with the previously acquired BGOOD data of $\gamma n \to K^0\Sigma^0$ in search for the peak predicted analogously to the LHCb pentaquarks. These findings corroborate the possibility of the existence of dynamically-generated molecular-like states near production thresholds in the strange sector.

Contents

CHAPTER 1

Introduction

The rapid progress of accelerator and detector technology in the first half of the 20th century provided experimental physicists with the necessary tools to discover a wide range of previously unknown particles - a multitude so extensive that it was referred to as the 'particle zoo'. On the theoretical side, classifying the particle zoo turned out to be an opaque and complex endeavour, as the sheer number of particles appeared too great for all of them to be considered elementary, and most models failed to provide rigorous explanations. An early attempt to describe the π as a composite particle formed by the association of a N and an $\bar{N}$ was made by Fermi and Yang in 1949 [1]. The idea of particles as compound objects was further developed by Sakata, who suggested in 1956 that particles might consist of p, n, Λ and their corresponding antiparticles [2], which was later experimentally disproven [3]. Finally, Gell-Mann came up with an ordering scheme in 1961, his so-called 'eightfold way' [4], in which he combined SU(2) isospin symmetry with U(1) strangeness symmetry in order to form SU(3) symmetry, which allowed for sorting the particles into meson and baryon multiplets. At the same time as Okubo, he developed what would later become known as the 'Gell-Mann-Okubo mass formula' [4][5][6], which enabled the prediction of the subsequently observed Ω^- [7]. In 1964, Gell-Man and Zweig simultaneously proposed to describe these particles as a composition of even more fundamental objects, the 'quarks' [8][9]. Both the sorting of the eightfold way and the corresponding underlying quark content are depicted in figure 1.1 for meson and in figure 1.2 for baryon multiplets.

It is today's textbook knowledge that mesons consist of a quark-antiquark pair and baryons of three quarks. But already in his 1964 paper, Gell-Mann wrote:

'Baryons can now be constructed from quarks by using the combinations (qqq)*,* $(qqqq\bar{q})$*, etc., while mesons are made out of* $(q\bar{q})$*,* $(qq\bar{q}\bar{q})$*, etc.'* [8]

Gell-Mann thus anticipated the possible existence of multi-quark states beyond the basic configurations. He went on to be awarded the Nobel prize in physics in 1969 *'for his contributions and discoveries concerning the classification of elementary particles and their interactions'* [10]. In the following decades, 'colour' was introduced based on symmetry considerations as the charge of the strong interaction [11], the basis of quantum chromodynamics was developed [12], the c-quark [13][14][15], b-quark [16] and t-quark [17] were observed and the asymptotic freedom of the strong interaction was discovered [18][19], leading to the current picture within science, the Standard Model of particle physics.

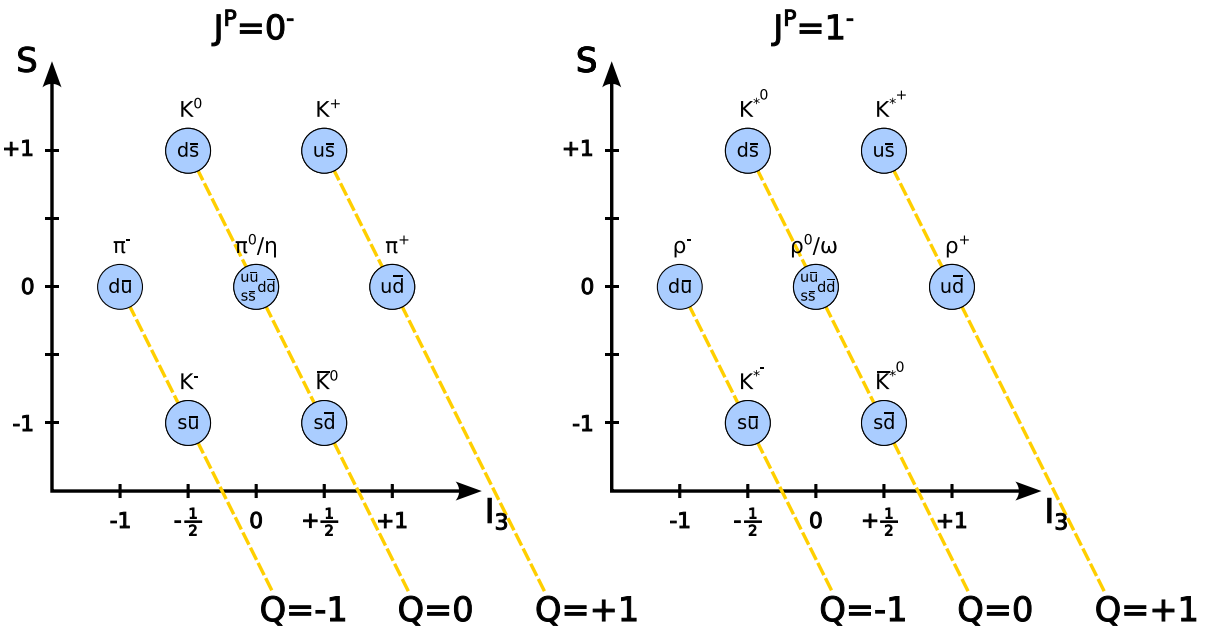

Figure 1.1: Multiplets of pseudo-scalar mesons with $J^P = 0^-$(left) and vector mesons with $J^P = 1^-$ (right) sorted by strangeness S and third isospin component I_3 as described in the eightfold way. Additionally, the quark flavours of the underlying SU(3) flavour symmetry are given. The diagonal lines describe the charge Q.

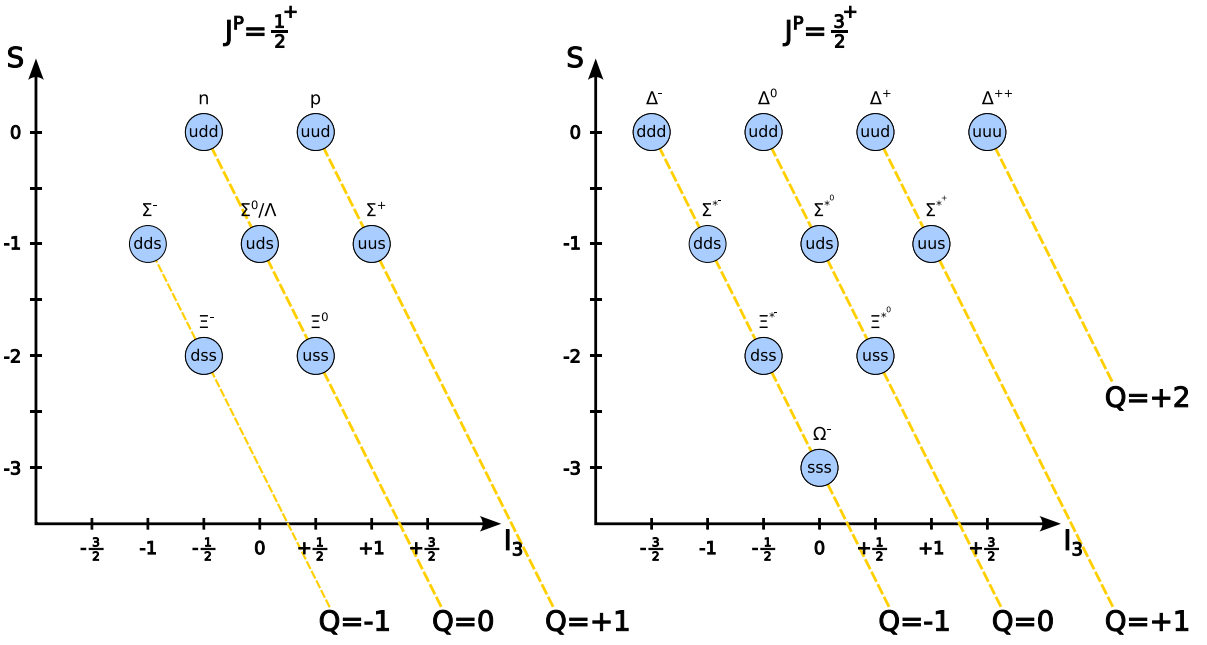

Figure 1.2: Multiplets of baryons with $J^P = \frac{1}{2}^+$ (left) and baryons with $J^P = \frac{3}{2}^+$ (right) sorted by strangeness S and third isospin component I_3 as described in the eightfold way. Additionally, the quark flavours of the underlying SU(3) flavour symmetry are given. The diagonal lines describe the charge Q.

While the Standard Model in itself can be considered an enormous scientific success and makes extremely accurate predictions in the perturbative description of quantum electrodynamics (QED), providing a rigorous explanation of quantum chromodynamics (QCD) remains elusive due to persistent complications. Unlike the photons in QED, the gluons in QCD undergo a first-order self-interaction. Thus, the Feynman diagrams of QCD processes involve quark-antiquark-gluon vertices, three-gluon and four-gluon vertices, and integrating over all of these possible final states leads to collinear and soft divergences that can no longer be solved analytically [20][21]. A widely-used method to circumvent these issues are constituent quark models (CQM), which describe the formation of hadronic states as quarks confined within a specific potential. This includes the states classified by the eightfold way as well as higher-lying resonances, the latter being described as excitations of two- or three-quark systems. In general, such models exhibit specific difficulties in describing the baryon excitation spectra:

- The parity between the two lowest-lying N excitations, namely $N(1440)\frac{1}{2}^+$ and $N(1535)\frac{1}{2}^-$, is reversed. This is depicted in figure 1.3, which shows masses of theoretically predicted and discovered N resonances depending on their quantum numbers. Naturally, one would expect the lowest state above the ground state to have negative parity [22].

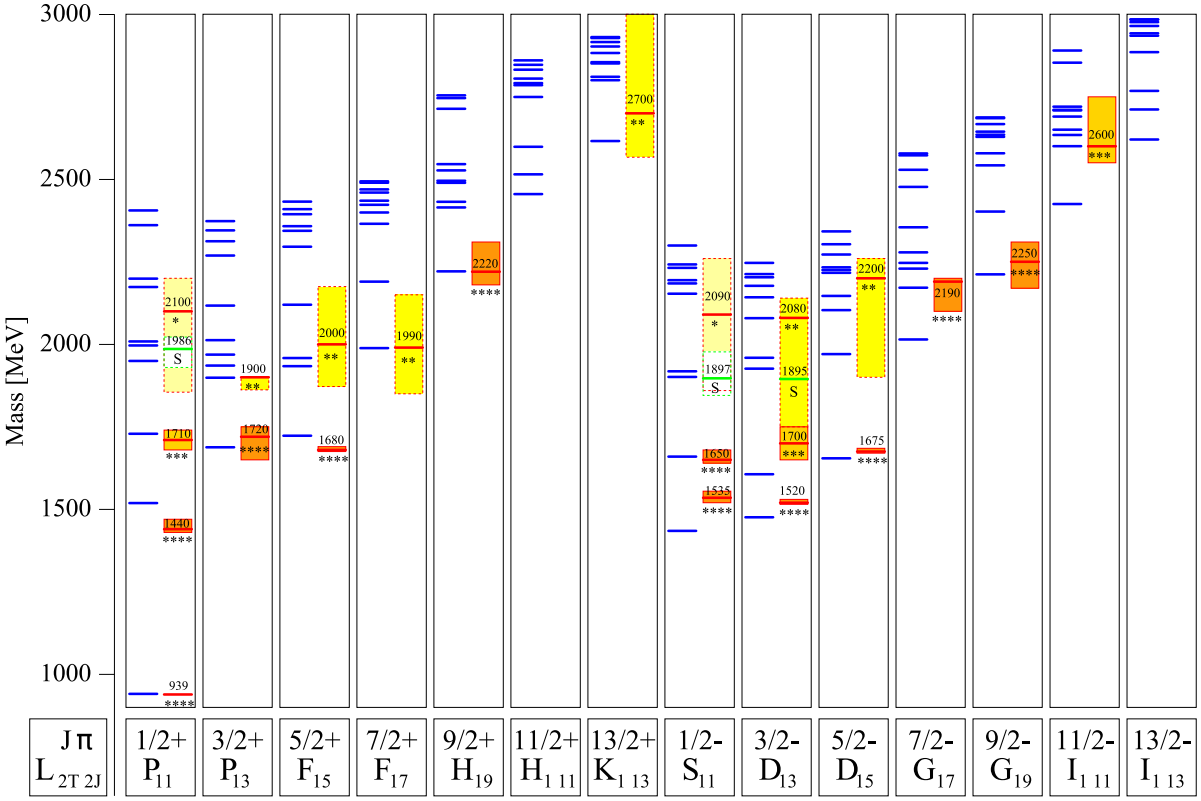

Figure 1.3: N resonances in a generic relativistic CQM [23]. The x-axis describes the baryon quantum numbers, the y-axis depicts their masses. Blue lines correspond to theoretically predicted resonances. Coloured boxes correspond to experimental findings, where the sizes of the boxes specify the error ranges.

- The masses between the two lowest-lying negative parity states in the strange- and non-strange sector – the $\Lambda(1405)$ shown in figure 1.4 and the $N(1535)\frac{1}{2}^-$ shown in figure 1.3 - are reversed. One would expect the heavier state to contain the s quark [22], despite the $\Lambda(1405)$ being a singlet state.

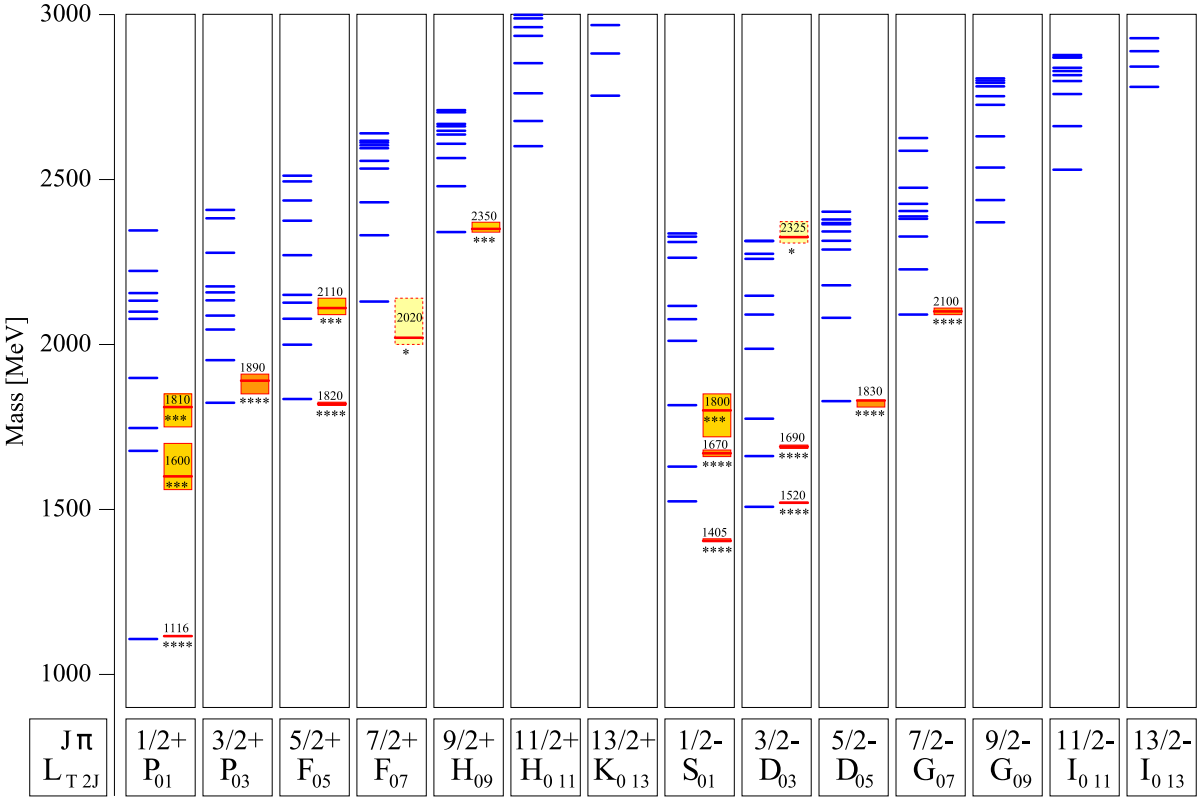

Figure 1.4: Λ resonances in a generic relativistic CQM [24]. The same colouring scheme as in figure 1.3 is used.

- In addition to these serious issues regarding the low-lying states, the number of high-lying states is also a matter of concern. Generic CQMs predict many more high-mass resonances than have been found experimentally. This is known as the 'missing resonance problem' and illustrated in figure 1.3 and 1.4. It is apparent that most of the predictions for high-mass resonances are not backed by experimental data. The validity of the theoretical predictions is still under debate, as most of the CQMs are unable to compute the decay widths of the associated resonances, lacking any coupling to the continuum [23][25].

Several approaches to solve these open problems exist. One of these is lattice quantum chromodynamics (LQCD) [26], which is a non-perturbative ab initio theory that discretizes Euclidean space time, usually in a hypercubic lattice, and locates quark fields on the sites of the lattice and gauge fields on the links between sites. The lattice spacing takes the role of the cutoff criterion for high-energy short-time effects. In the limit of vanishing lattice spacing, the continuum theory can be recovered. A major challenge for LQCD-based models is that, similar to perturbative-based CQMs, the quark masses and the strong coupling constant enter as free parameters and require a delicate fine-tuning to experimental data. Additionally, LQCD-based models require immense computational resources. While LQCD has improved over the last decades, foremost

in the description of hadronic ground states, there is still ongoing debate about the methodology and a description of decays of baryonic resonances to more than two daughter particles is still out of reach [27].

Another approach to resolve these issues is through quark models that allow for 'unconventional' quark arrangements, allowing baryons to be composed of more than three quarks as formerly suggested by Gell-Mann in his 1964 paper [8]. One possible manifestation would be the arrangement of quarks in colourless, molecular-like meson-meson or meson-baryon formations near production thresholds [22][28]. Compared to conventional three-quark CQMs, dynamic meson-baryon interactions would reduce the degrees of freedom from three down to two, which would restrict the amount of existing baryonic resonances. The force between the neutral meson and baryon could be mediated by the Goldstone bosons resulting from the symmetry breaking within this model, which enter as effective 'elementary' objects [29]. A counterpiece to these molecular-like configurations would be genuine tetraquark or pentaquark states [30], in which all quarks interact mutually with each other through gluon exchange. Prominent examples for aforementioned unconventional states are:

- The enigmatic $\Lambda(1405)$, which has stirred up discussions about its structure since its discovery in 1961 [31]. The particle data group (PDG) made following statement in 2010:

  '[…] to settle the decades-long discussion about the nature of the $\Lambda(1405)$ - true 3-quark state or mere $\bar{K}N$ threshold effect? - unambiguously in favor of the first interpretation [...]' [32]

  Then, after intense experimental and theoretical efforts, the full roll backwards came in 2016, as the PDG wrote about the $\Lambda(1405)$:

  'It is the archetype of what is called dynamically generated resonance, as pioneered by Dalitz and Tuan [33].' [34]

- The pentaquark states $P_c(4312)^+$, $P_c(4440)^+$ and $P_c(4457)^+$. After controversial predictions and false measurements in the early 2000s [35], the first unambiguous pentaquark states were discovered at LHCb in 2015 [36] while observing the decay $\Lambda_b^0 \to J/\Psi K^- p$. For the Λ_b^0, two decay mechanism are possible: Directly to $J/\Psi\Lambda^*$ as shown in figure 1.5 (a) or via the pentaquark formation $P_c^+ K^-$ as shown in figure 1.5 (b). A fit based on decay (a) using all 14 Λ^* states listed by the PDG proved unsuccessful, while a fit based on decay (b) using the well-established Λ^* and two pentaquark states yielded the best description of the data [36]. After a further analysis of an improved dataset, pentaquark states located at 4312MeV, 4440MeV and 4457MeV could be established [37]. The invariant mass spectrum of the $J/\Psi p$ system together with the pentaquark fit functions is shown in figure 1.5 (c). It can be seen that the pentaquark states lay just at the hadronic thresholds of $\Sigma_c^+\bar{D}^0$ and $\Sigma_c^+\bar{D}^{*0}$.

If the formation of pentaquarks is not a unique feature of the charm sector, but a universal feature of the strong interaction, one should be able to find analogous states in the strange sector. A natural approach would be to exchange the c quark of the $\Sigma_c\bar{D}$ states with a s quark, leading to the ΣK states which are listed in table 1.1.

Indeed, the same model that predicted the LHCb pentaquark also predicts certain structures in the strange sector [38]. One of such states equivalent to the charm sector is the $N^*(2030)$ resonance, which is thought to be a dynamically-generated $K^*\Sigma$ state. The $N^*(2030)$ is expected to magnify the destructive interference of amplitudes driven by intermediate $K^*\Lambda$ and $K^*\Sigma$ channels, and thus causing a cusp-like structure observed

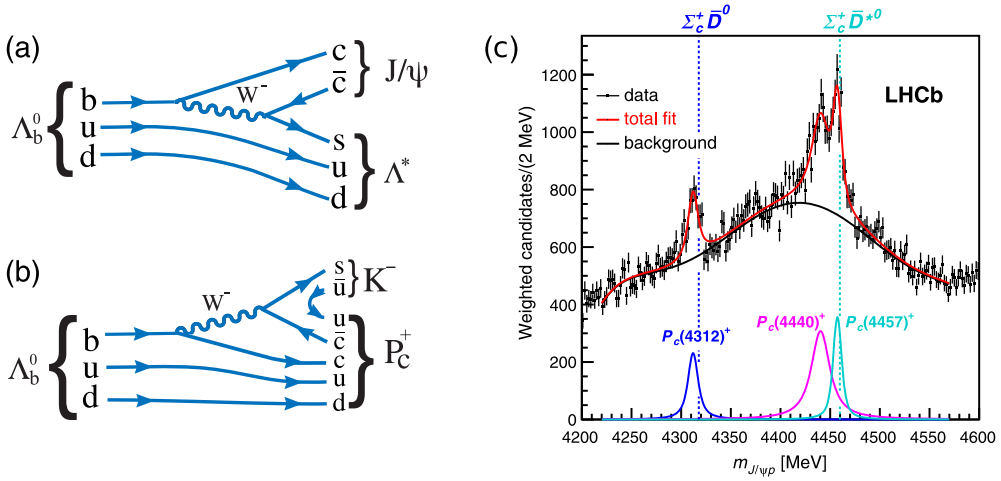

Figure 1.5: (a) Feynman diagram for $\Lambda_b^0 \to J/\Psi\Lambda^*$ (b) Feynman diagram for $\Lambda_b^0 \to P_c^+ K^-$ (c) Invariant mass distribution of the $J/\Psi p$ system including fit functions and production thresholds of $\Sigma_c^+\bar{D}^0$ and $\Sigma_c^+\bar{D}^{*0}$ [36][37].

J^P	Charm sector		Strange sector	
	Threshold	State	Threshold	Evidence for state
$\frac{1}{2}^-$	$\Sigma_c^+\bar{D}^0$	$P_c(4312)$	$\Sigma^0 K^+$	Possibly $N^*(1535)$
$\frac{3}{2}^-$	$\Sigma_c^{*+}\bar{D}^0$	$P_c(4380)$	$\Sigma^0(1385)K^+$	Peak in $K^+\Sigma^0$
$\frac{3}{2}^-$	$\Sigma_c^+\bar{D}^{*0}$	$P_c(4457)$	$\Sigma^0 K^{*+}$	$N^*(2030)$-related effects
$\frac{1}{2}^-/\frac{5}{2}^-$	$\Sigma_c^{*+}\bar{D}^{*0}$	-	$\Sigma^0(1385)K^{*+}$	-

Table 1.1: Analogies of unconventional states between the charm and strange sector [39][40]

in the $\gamma p \to K^0\Sigma^+$ cross section at about 2 GeV [41]. In contrast to that, regarding the reaction $\gamma n \to K^0\Sigma^0$, this interference is mitigated by the dominance of the amplitude that drives the intermediate $K^*\Sigma$ channel, and is expected to give rise to a resonant peak in the spectrum. This would be considered a smoking gun signal for the existence of these dynamically-generated meson-baryon states [40]. Both the predictions for $K^0\Sigma^+$ and $K^0\Sigma^0$ as well as the measurement for $K^0\Sigma^+$ are shown in figure 1.6, exhibiting a good match for the $K^0\Sigma^+$ channel. Still, more data of kaon-hyperon photoproduction is needed, which must be measured by experiments which can access the specific involved kinematics.

In general, relatively loosely bound molecular-like states are expected to be produced during low-t processes, where the momentum transfer is lower than the internal momenta of the baryonic system, allowing it to not break up immediately. For associated strangeness production, e.g. $\gamma n \to K^+\Lambda$, the K^+ then takes most of the momentum and goes to forward angles.

The BGOOD experiment at the ELSA accelerator at the University of Bonn is especially designed for these kind of investigations due to its combination of a large-aperture forward spectrometer complemented by a central BGO calorimeter with almost 4π angular acceptance. Amongst others, recent results of the BGOOD collaboration are:

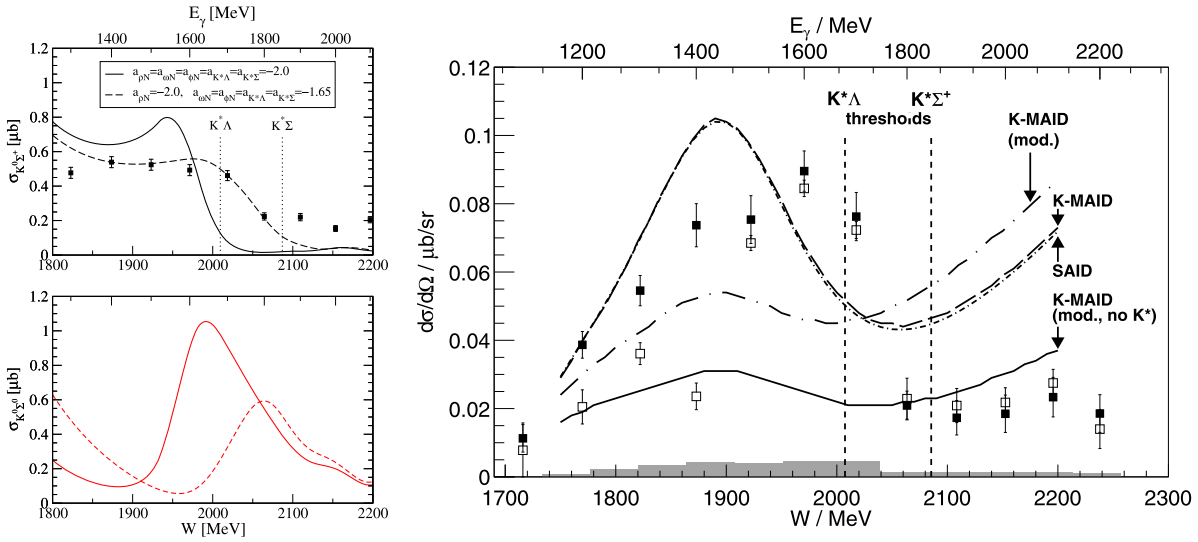

Figure 1.6: Left: Prediction for the differential cross section of $K^0\Sigma^+$ (top) showing a cusp and $K^0\Sigma^0$ (bottom) showing a peak at about 2 GeV [38]. Right: Differential cross section of $K^0\Sigma^+$ photoproduction as a function of W at $0.66 < \cos(\theta_{\mathrm{CM}}) < 1$ (full squares) showing a cusp at about 2 GeV [41].

- Measurement of the differential cross section (DCS) of the smoking gun reaction $\gamma n \to K^0\Sigma^0$ mentioned earlier, which is shown in figure 1.7. The model that predicted the LHCb pentaquark also predicts a peak at the K^* threshold [38]. Due to limited statistics, the new data neither exclude nor confirm a structure at $W \approx 2\,040$ MeV [42]. More data is needed to make a firm statement.

- Measurement of the integrated cross section and DCS of the reaction $\gamma p \to K^+\Lambda(1405)$, showing a significant suppression for extreme forward K^+ angles around a centre-of-mass energy of $W \approx 2\,100$ MeV, which supports the involvement of a triangle singularity induced by the $N^*(2030)$ resonance. Figure 1.8 depicts the integrated cross section together with models including and excluding the triangle singularity [43].

- Measurement of the DCS of the reaction $\gamma p \to K^+\Sigma^0$, showing a cusp-like structure most pronounced at extreme forward K^+ angles, which might be indicative of rescattering effects close to open and hidden strange thresholds [45]. An extrapolation to the minimum momentum transfer t_{min} is shown in figure 1.9.

More data, especially on the smoking gun reaction, is needed to gain further insight into the possibility of the existence of dynamically-generated molecular-like states. If the smoking gun reaction should indeed exhibit a peak in the DCS, one may naturally expect analogous structures in the DCS of its charge-conjugated counterpart, namely the reaction $\gamma n \to K^+\Sigma^-$. The measurement of the DCS of the reaction $\gamma n \to K^+\Sigma^-$ at extreme forward angles, where molecular-like states are most likely to appear, is the subject of this thesis. A further aspect is that recent effective Lagrangian approaches [46] struggled to produce a fit that satisfies both the complementary $\gamma n \to K^0\Sigma^0$ dataset provided by the A2 Collaboration [47] and the one of the BGOOD collaboration [42] simultaneously, while being in good agreement with $\gamma n \to K^+\Sigma^-$ data. Providing more data will constrain the fits from effective Lagrangian approaches made by different theoretical groups [46][48][49] and will help to disentangle this situation.

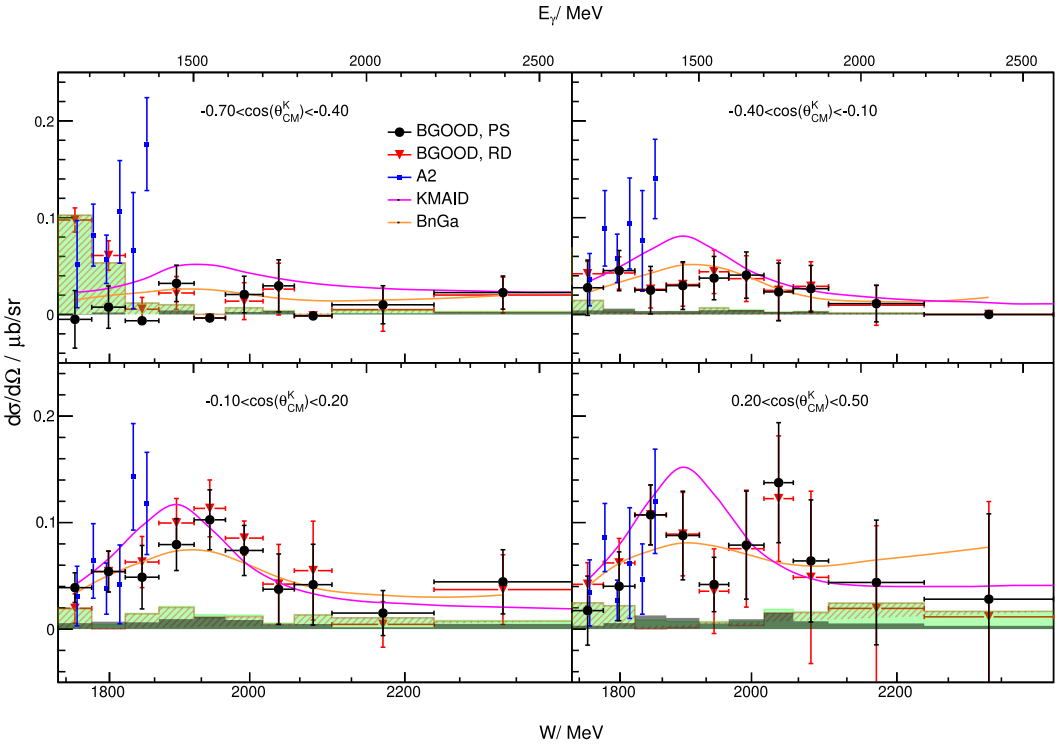

Figure 1.7: DCS of $\gamma n \to K^0\Sigma^0$ as a function of W in four bins in $\cos(\theta_{\mathrm{CM}})$ for two different analysis methods (black and red, respectively). Due to limited statistics, the new data can neither exclude nor confirm a structure at about $W \approx 2\,040$ MeV in the most forward angular bin $0.20 < \cos(\theta_{\mathrm{CM}}) < 0.50$ [42].

Currently, DCS data for $\gamma n \to K^+\Sigma^-$ is very scarce. Only one dataset by CLAS [50] at the less forward angle $0.8 < \cos(\theta_{\mathrm{CM}}) < 0.9$ as well as one very small dataset by LEPS [51] are available. In this thesis, measurements in previously unexplored kinematic regions will be provided and existing datasets will be complemented with data of unprecedented statistical accuracy. This thesis is structured as follows:

Chapter 2 provides a description of the particle accelerator ELSA and the BGOOD experiment. Chapter 3 elucidates the calibrations that were applied to all used datasets. Chapter 4 specifies all steps of the analysis procedure that were taken in order to extract the DCS of $\gamma n \to K^+\Sigma^-$, the associated statistical and systematic uncertainties are described in the subsequent chapter 5. The final results are presented and interpreted in chapter 6. A summary is given in the last chapter 7.

Throughout the thesis, natural units are used, setting $\hbar = c = 1$.

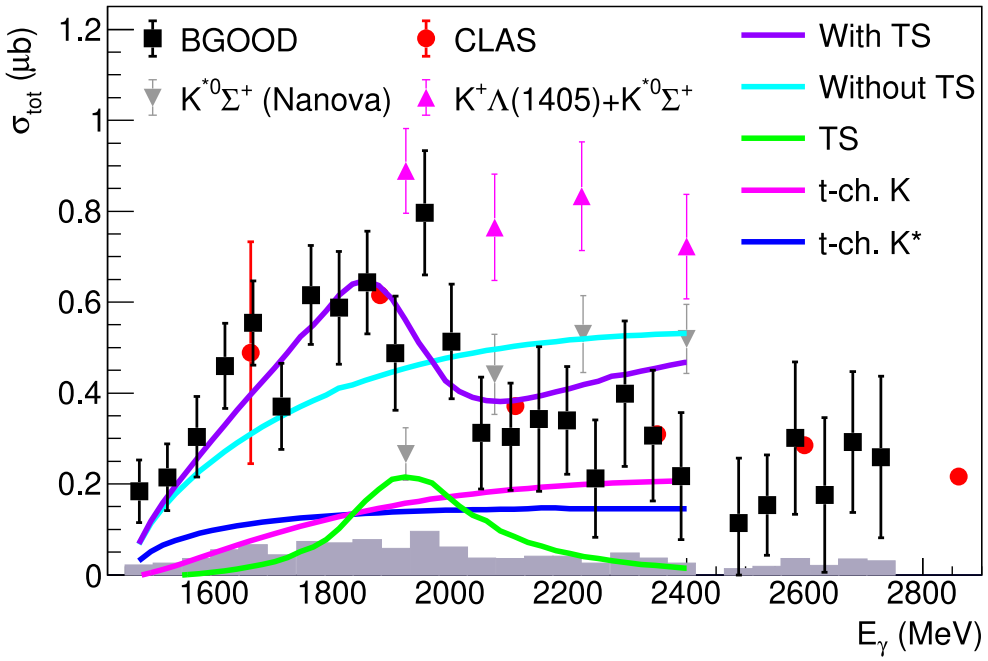

Figure 1.8: Integrated $\gamma p \to K^+\Lambda(1405)$ cross section (black squares) [43] together with theoretical models including and excluding a triangle singularity as described by reference [44].

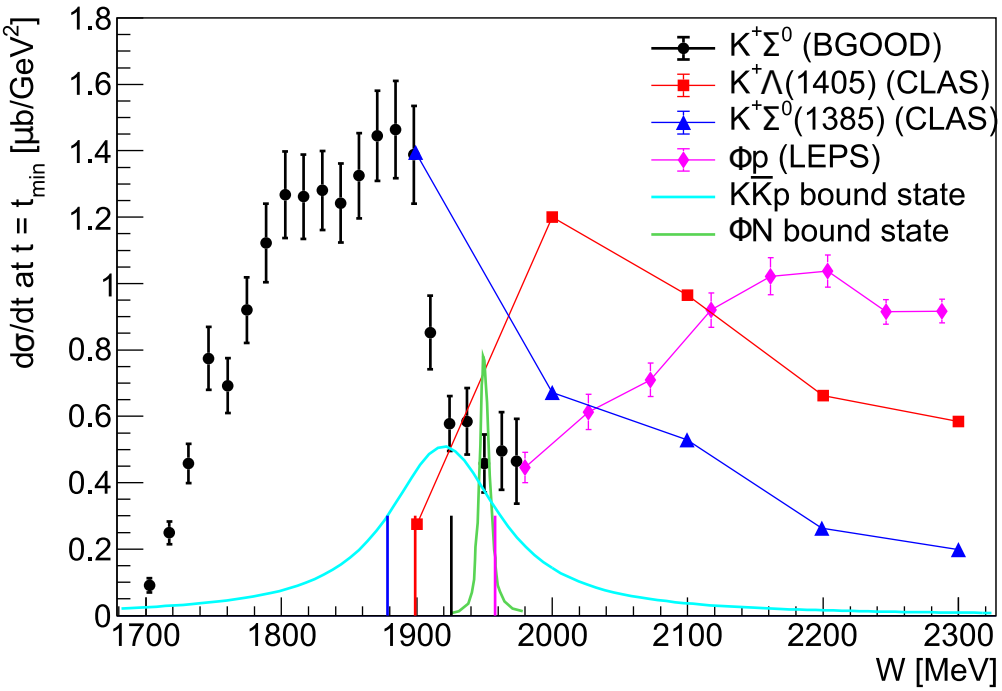

Figure 1.9: DCS $\frac{d\sigma}{dt}$ of $\gamma p \to K^+\Sigma^0$ extrapolated to t_{min} versus W (filled black circles). Vertical lines indicate production thresholds. The DCSs of $K^+\Sigma^0$ and $K^+\Sigma^0(1385)$ drop as the $K^+\Lambda(1405)$ and ϕp channels open up [45].

CHAPTER 2

Experiment

The BGOOD experiment located at the ELSA facility at the Rheinische Friedrich-Wilhelms-Universität Bonn is a fixed-target experiment designed for the investigation of meson photoproduction for t-channel processes at low momentum transfer to the residual baryonic system. The combination of a tagging system, a central calorimeter with almost 4π acceptance and a large-aperture forward spectrometer allows for precise measurements of reactions involving forward-going mesons. The material of the calorimeter, 'BGO', and the Open Dipole magnet of the spectrometer, called 'OD', are eponymous for the acronym 'BGOOD'.

An exhaustive description of the experimental setup is given in the technical paper 'The BGOOD experimental setup at ELSA' which was published in The European Physics Journal A [52]. Therefore, this chapter will only give a brief overview of the most important features and relies heavily on the given paper.

2.1 ELSA

The Electron Stretcher Accelerator (ELSA) [53] is a three-stage electron accelerator at the Physikalisches Institut. It is able to deliver electron beams up to a maximum energy of 3.2 GeV and supply BGOOD with a continuous beam current up to several nA. Figure 2.1 shows an overview of the three stages of the accelerator.

The first stage of ELSA is a linear accelerator, LINAC2, which provides an electron beam with an energy up to 26 MeV, either unpolarized or with a maximum degree of polarization of approximately 80%. In figure 2.1, LINAC2 is located in the lower left corner.
The electron beam is then fed to the second stage, the booster synchrotron, which operates with a pulsed beam and is able to accelerate electrons to energies ranging from 0.5 GeV to 1.6 GeV at a repetition rate of 50 Hz and maximum beam current of 500 nA.
When the electrons reach their maximum energy, a septum magnet is used to inject the beam into the third stage, the stretcher ring, where it is converted into a quasi-continuous beam. The stretcher ring has a circumference of 164.4 m and is capable of generating beam energies ranging from 0.5 GeV to 3.2 GeV using radio frequency cavities in combination with alternating-gradient focusing in FODO configurations. It can be operated in three different modes: In stretcher mode, the electron energy is being kept at the constant level of the booster synchrotron. In post-accelerating mode, extraction is paused while the stretcher ring is receiving several injections from the booster synchrotron and increases their energies. Furthermore, storage

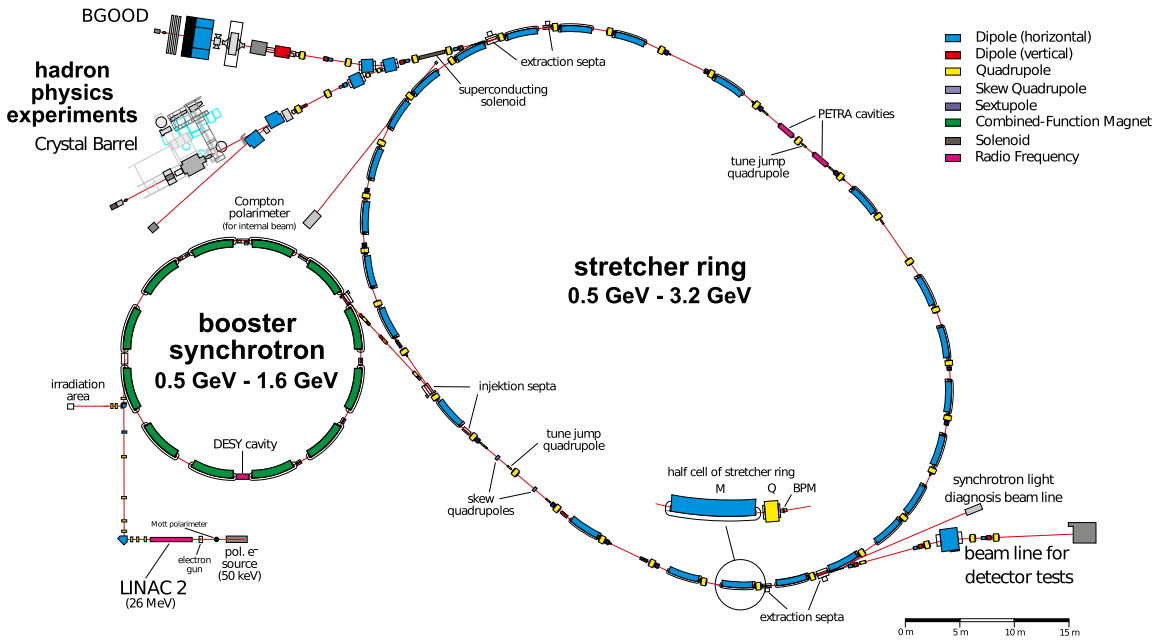

Figure 2.1: Overview of ELSA. LINAC2 is located in the lower left corner, BGOOD in the upper left corner. Figure adapted from reference [54].

mode allows the beam to be stored for several hours and used for synchrotron light experiments. Betatron extraction is used to extract a beam current of a few nA with a microscopic duty factor of about 85% and then lead it to the two associated experiments, BGOOD and Crystal Barrel, which can be seen in figure 2.1 in the upper left corner. The standard deviation of the Gaussian beam profile in horizontal direction is typically 1.2 mm and in vertical direction 0.3 mm [52][53][55].

2.2 BGOOD

The BGOOD experiment is illustrated in figure 2.2, in which the electron beam provided by ELSA enters from the lower right corner. A brief overview of the mode of operation shall be given here, whereas the following sections describe the individual detectors in more detail.

The electrons that were extracted from ELSA hit a dedicated radiator within the goniometer and are converted into bremsstrahlung photons, whose energies can be measured in the subsequent tagging system consisting of dipole magnet and tagger. The photon beam is collimated and enters the central detector, where it impinges on the target cell. The target cell is almost entirely enclosed by the barrel and the BGO ball calorimeter which allow for charge detection and energy and position measurements, except for a small opening in forward direction, through which particles can pass towards the forward spectrometer. These particles then traverse the positional detectors MOMO and SciFi, the enormous Open Dipole magnet and the driftchambers, which allows for momentum reconstruction. In combination with the following time of flight walls, which are used for β measurements, the invariant masses of the particles can be determined. A flux monitor is located at the very end of the experiment [52]. Figure 2.3 shows the coordinate system that is utilized in the BGOOD experiment.

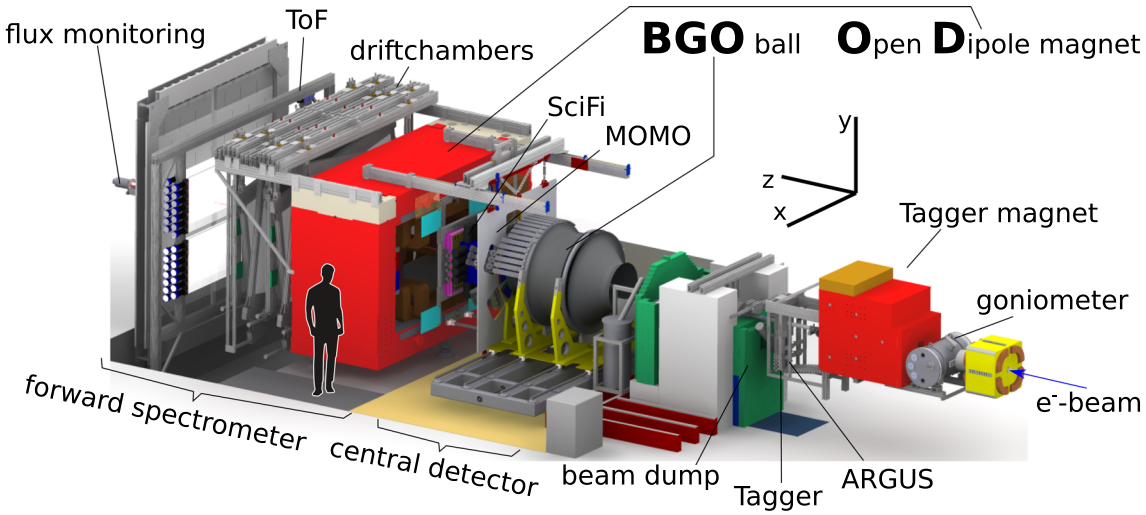

Figure 2.2: Overview of the BGOOD experiment. The electron beam provided by ELSA enters from the lower right corner [52].

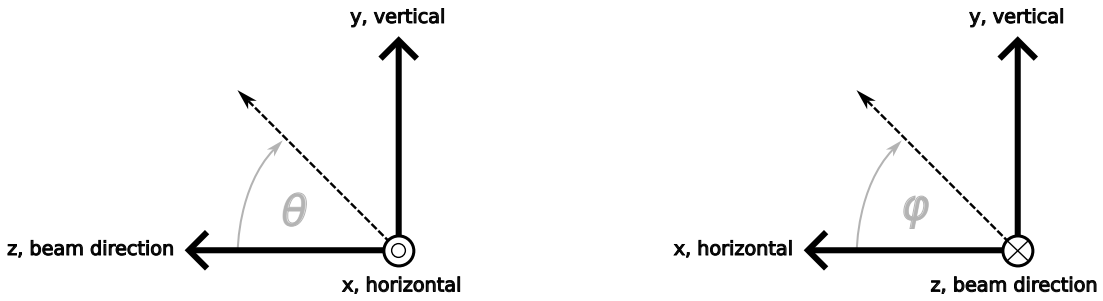

Figure 2.3: Right-handed coordinate system of the BGOOD experiment. The z-axis describes the beam direction, θ is the angle that spans from the positive z-axis towards the positive y-axis, ϕ is the angle that spans from the positive x-axis towards the positive y-axis.

In the following chapters, the individual detectors will be described in more detail.

2.2.1 Photon Tagging System

The tagging system serves two purposes: It determines the energy of a single bremsstrahlung photon by measuring the corresponding energy of the electron it originated from and it provides the time reference for all following detector signals, enabling an assignment to the same hadronic event. A side view of the tagging system can be seen in figure 2.4.

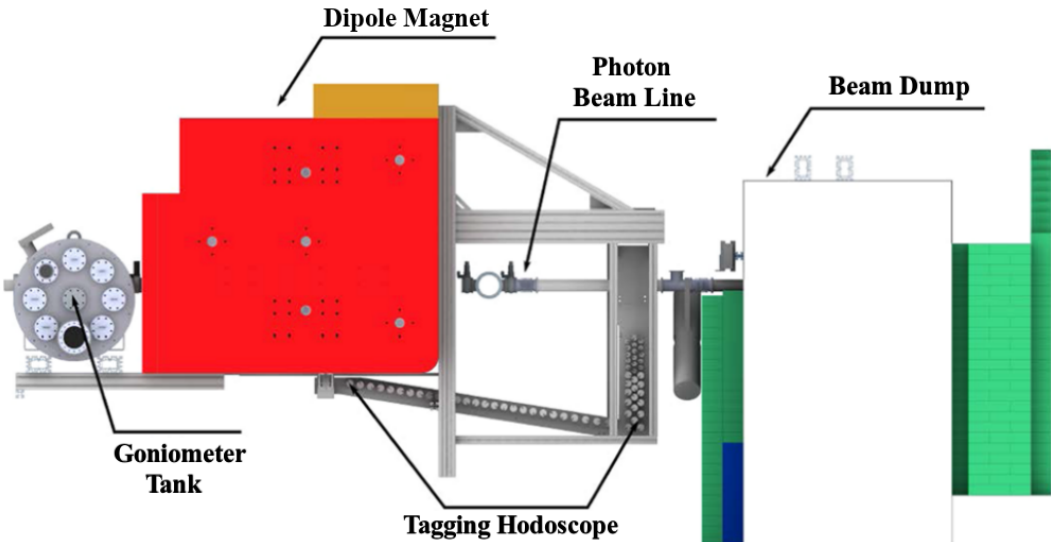

Figure 2.4: Side view of the tagger system. The electron beam provided by ELSA enters from the left side. Figure adapted from reference [52].

Goniometer

First, the primary electron beam of ELSA with a known energy E_0 is guided into a vacuum tank and irradiated onto a thin bremsstrahlung target, the radiator, which can precisely be aligned by the goniometer. Besides exact three-dimensional orientation, the goniometer provides a selection of different radiators and diagnostic tools for beam profile assessment. Amorphous radiators, such as copper plates with varying thickness, can be used to measure incoherent bremsstrahlung spectra in order to normalise the degree of polarization. A linearly polarized photon beam can be achieved by using a diamond radiator of 560 µm thickness and manipulating its orientation so that the recoil momentum is distributed over the full crystal lattice. Contrary to this coherent bremsstrahlung which produces a peak in the E_γ spectrum, incoherent bremsstrahlung occurs when the recoil momentum is transferred to a single atom, which follows a $\frac{1}{E_\gamma}$ distribution [52].

Tagger and Tagging Principle

The tagging principle is illustrated in figure 2.5. The incoming electrons are decelerated in the Coulomb field of the radiator nuclei, where each electron emits a single bremsstrahlung photon of energy E_γ. The energy of the bremsstrahlung photon can then be determined by measuring the energy E_{e^-} of the electron that had been involved in the bremsstrahlung process:

$$E_\gamma = E_0 - E_{e^-} \, .$$

This is achieved by the combination of a dipole magnet followed by a tagging hodoscope. Both post-bremsstrahlung electron and corresponding photon enter the dipole magnet that generates a maximum magnetic field of $B_{\text{max}} = 2\,\text{T}$. While the photon traverses the magnet unaffected, the electron is affected by the Lorentz force and experiences a circular deflection, where the trajectory's radius depends on the electron

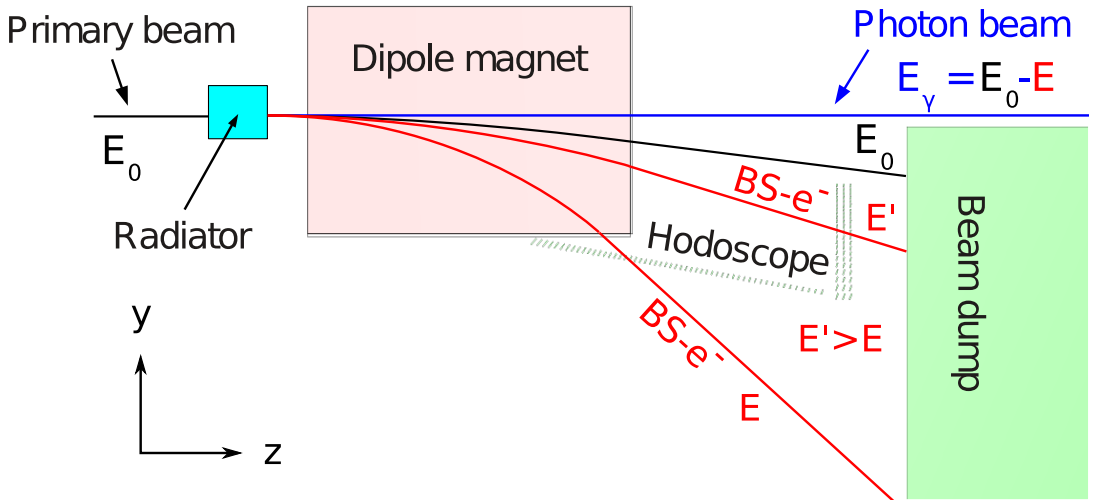

Figure 2.5: Operating principle of the tagger. The electron beam provided by ELSA enters from the left side [56].

momentum. As different radii lead to different impact points on the position-sensitive hodoscope, the momentum and thus the energy E_{e^-} of the post-bremsstrahlung electron can be determined. The hodoscope uses 120 plastic scintillators to cover an energy range of $10\%E_0$ to $90\%E_0$. Out of the 120 plastic scintillators, 54 are positioned horizontally, while 66 are positioned vertically at the point where the focal plane of the dipole magnet lies within the beam dump, rendering a horizontal alignment impossible. For the detection of an electron, a coincidence of adjacent scintillators is necessary, which are arranged with 55% overlap to each other. A coincidence channel provides an energy resolution of $0.40\%E_0$ in the horizontal plane and $0.60\%E_0$ to $1.70\%E_0$ in the vertical plane with a time resolution of 210 ps. The time information of the tagging system is used as the time reference for the BGOOD experiment. Electrons that did not produce bremsstrahlung are led to the beam dump. Within the evacuated beam pipe, the generated photons are collimated in a first collimator. Charged particles that were created as the photons hit the collimator are removed by a subsequent sweeping magnet. The photons are then again collimated in a second collimator and led to the target [52][56].

ARGUS

The energy resolution of the vertical part of the tagger is further improved to be in-between $0.08\%E_0$ to $0.45\%E_0$ by ARGUS, which is a scintillating fibre detector with a total of 480 fibres that cover smaller regions than the initial tagger scintillators. The energy range covered by ARGUS reaches from $30\%E_0$ to $66\%E_0$. ARGUS also decreases the systematic error in the determination of the degree of polarization by one order of magnitude [52][57][58].

2.2.2 Central Detector and Target

The energy-tagged photons impinge on the target within the evacuated beam pipe located at the centre of the BGO calorimeter. The target cell is surrounded by the central detector, a slice view of which can be seen in figure 2.6. The innermost layer surrounding the target is the Multi Wire Proportional Chamber (MWPC), which was out of commission at the writing of this thesis. It is followed by the scintillator barrel, which allows for charged particle identification, and the BGO crystal calorimeter, which allows for energy and po-

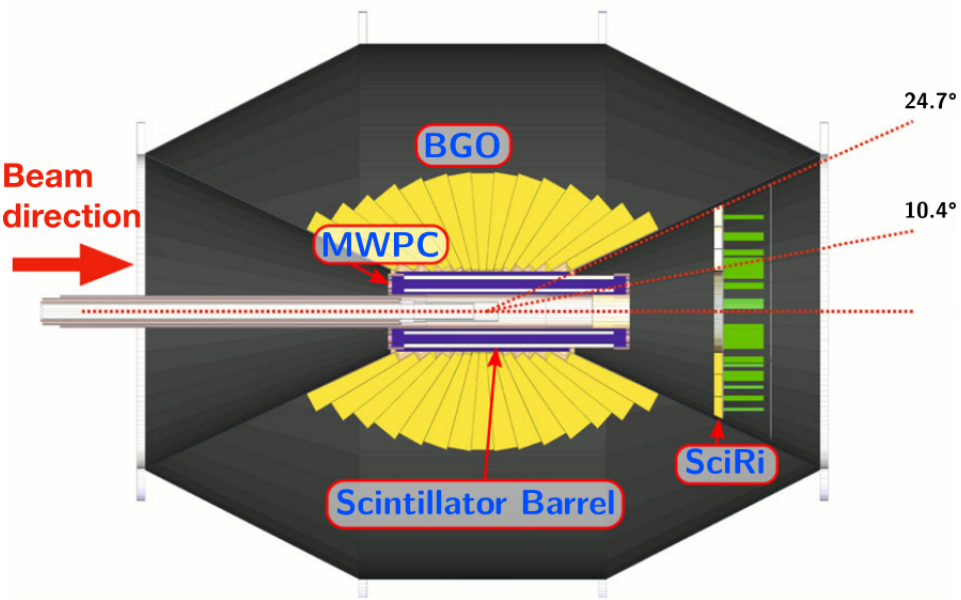

Figure 2.6: Slice view of the central detector. The photons enter the target from the left. The acceptance gap on the right leads towards the forward spectrometer. Figure adapted from reference [52].

sition measurements. The central detector covers the full azimuthal ϕ range and a polar range from $\theta = 25°$ to 155°.

Target

Either solid state targets, such as carbon, or cryogenic liquid targets, such as liquid hydrogen (H_2) at a temperature of 18.0 K or liquid deuterium (D_2) at a temperature of 21.5 K, can be used. The cryogenic target cell is a hollow aluminium cylinder of 4 cm diameter and 0.5 mm wall thickness. Target cells with effective lengths of 6 cm and 11 cm can be chosen. Beam entrance and exit windows consist of Mylar foil with a thickness of 0.1 mm [52].

Scintillator Barrel

The scintillator barrel, also called 'barrel', consists of 32 plastic scintillators made from BC448 with a thickness of 5 mm arranged in a cylinder. The detection efficiency for charged particles is about 98% and the ones of photons and neutrons below 1%, which allows for a differentiation of charged and uncharged particles in combination with energy measurements in the BGO calorimeter [52][59].

BGO Calorimeter

The main component of the central detector is the BGO calorimeter, also called 'BGO rugby ball', which is located at the outermost layer. It measures the energy deposition and location of traversing particles. The BGO calorimeter consists of a total of 480 crystals made from bismuth germanate, $Bi_4(GeO_4)_3$, of 24 cm length, which corresponds to approximately 21 radiation lengths. The crystals are arranged in 15 ring-shaped

crowns of 32 crystals each and cover the full azimuthal ϕ range, whereas the polar θ range is covered from 25° to 155°. The Gaussian invariant mass peak from the decay $\pi \rightarrow \gamma\gamma$ can be resolved with an energy resolution of 15 MeV. A time resolution of 2 ns can be achieved by reading out the sharp rising edge of the signal inside the BGO material using photomultiplier tubes (PMTs) fixed at the end of the crystals in combination with sampling ADCs [52][59]. The clustering algorithm works as follows: If an energy deposit in a single crystal surpasses the hit energy threshold of 1.5 MeV, it is registered as a hit. Adjacent hits which are coincident in time form a cluster, if the energy sum of these hits surpasses the cluster energy threshold of 25 MeV. The energy sum is assigned as the cluster energy. The position vectors of the hits are weighted with their energy and the mean over these position vectors is assigned as the cluster position vector. If the barrel detected a charged particle within 20° in ϕ to the cluster position vector which is coincident in time, the cluster is marked as charged.

Scintillating Ring

The scintillating ring (SciRi) covers a small acceptance gap from $\theta = 10°$ to $\theta = 25°$ between the open forward cone of the BGO ball and the rectangular magnet gap of the forward spectrometer. The 20 mm thick plastic scintillators detect charged particle positions but do not allow for an accurate energy measurement. Thus, SciRi is used as a veto detector for the presence of charged particles [52][60].

2.2.3 Forward Spectrometer

A forward-going particle that leaves the central detector through the acceptance gap can be detected in the forward spectrometer (FS), a slice view of which can be seen in figure 2.7. The FS covers a polar range of approximately $\theta = 1.5°$ to $\theta = 10°$. Detecting a particle in MOMO or SciFi and assuming that it originated from the target centre allows for reconstructing the particle's track in front of the Open Dipole magnet. As a charged particle traverses the magnetic field, it is deflected. Behind the Open Dipole magnet, its track is measured in the eight driftchambers. Knowing the particle's tracks in front of and behind the Open Dipole magnet as well as the magnetic field strength allows for reconstructing its trajectory, the corresponding deflection radius and thus the momentum p. In a momentum range of approximately $p = 400\,\text{MeV}$ to $p = 1\,100\,\text{MeV}$, a momentum resolution of 3% can be achieved. Hits in at least two different walls of the Time of Flight Spectrometer allow for a determination of the particle's velocity and thus β. Knowing p and β, a measurement of the particle's mass is possible by using equation 2.1:

$$m_{\text{ToF}} = p\frac{\sqrt{1-\beta^2}}{\beta}\,. \tag{2.1}$$

This term is denoted as 'time of flight mass'. Figure 2.8(a) shows the relation between β and p and figure 2.8(b) a typical time of flight mass spectrum.

MOMO and SciFi

MOMO and SciFi are scintillating fibre detectors that are used to measure the particle's position and direction in front of the Open Dipole magnet. The fibres of MOMO are arranged in six rotated, overlapping modules, while the fibres of SciFi are orientated horizontally and vertically. MOMO achieves a particle position reconstruction efficiency of about 80%, whereas SciFi achieves 97.5%. A 4 cm × 4 cm hole at the

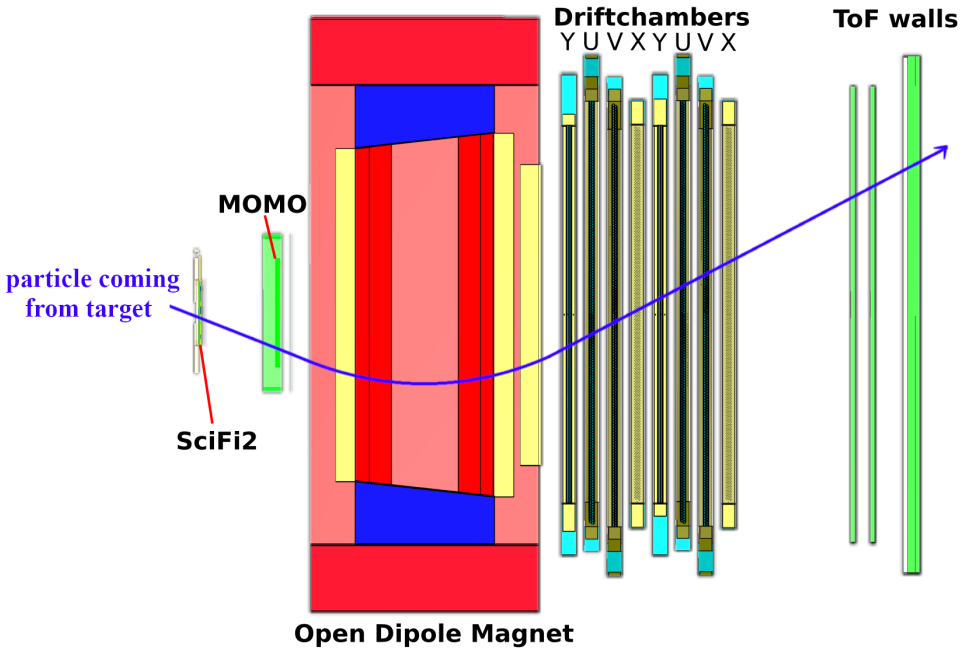

Figure 2.7: Slice view of the forward spectrometer. The particles from the target enter from the left. Figure adapted from reference [61].

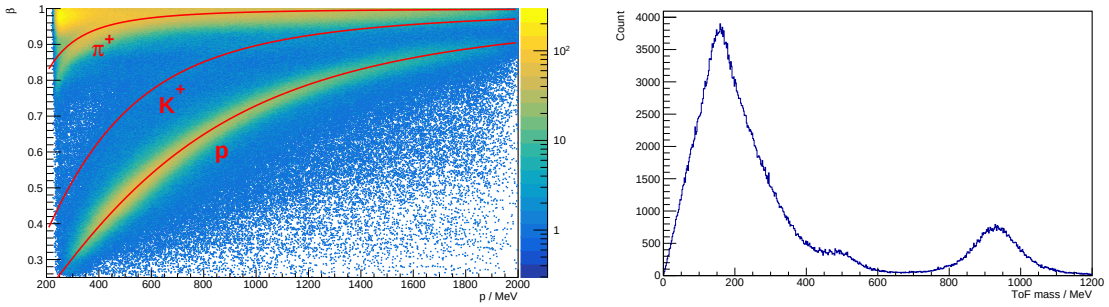

(a) β vs. p for positively charged tracks

(b) Time of flight mass spectrum

Figure 2.8: Figure (a) shows β vs. p for positively charged tracks, the red lines correspond to the masses of the π^+, K^+ and proton. A typical time of flight mass spectrum originating from equation 2.1 is illustrated in figure (b), showing peaks corresponding to π^+, K^+ and proton from left to right.

centre allows photons that did not interact with the target to pass through [52][62].

Open Dipole

The heart of the forward spectrometer is the Open Dipole Magnet (OD) that is able to generate a maximum magnetic field strength of $B_{\text{max}} = 0.53\,\text{T}$ at a bending power of $\int Bdl \approx 0.71\,\text{T m}$. It has a weight of 94 t and a size of 2.8 m (height) × 3.9 m (width) × 1.5 m (length). Three-dimensional field maps including the fringe

field have been measured at a step size of 1 cm for different field strengths and have also been modeled in simulation [52][63].

Driftchambers

After the particles have been deflected inside the OD, their resulting positions and directions are measured with eight driftchambers (DCs) that each have two layers of hexagonal drift cells. To improve spatial resolution, two DCs are rotated by 90° and four by 9°, covering a total area of 2.5 m × 1.2 m. The DCs are filled with a gas mixture of 70% argon and 30% CO_2 and are operated at a high voltage of about −2.8 kV, which allows for a drift velocity of about $v_D = 7\ \frac{cm}{\mu s}$. The centre of the DCs have been made insensitive in order to avoid a saturation of the signal caused by the photons that did not interact with the target [52][64].

Time of Flight Spectrometer

The Time of Flight Spectrometer (ToF) is located behind the DCs and is used to determine the β of the traversing particle by combining its own time measurement, which possesses a time resolution of 0.34 ns, with the time information provided by the tagger. The invariant mass of the particles can be determined by combining the β measurement with the momentum measurement that utilized the deflection of the particle's trajectory within the magnet. ToF consists of three walls of horizontal plastic scintillator bars. The horizontal position of traversing particles can be assessed by analysing the time difference beween the readouts of the two PMTs that are placed at the ends of the scintillator, whereas the vertical position is determined by the position of each individual scintillator bar itself [52][65].

2.2.4 Photon Monitoring System

The photon monitoring system is located behind the ToF walls at the very end of the experiment. It consists of the Gamma Intensity Monitor as well as the Flux Monitor and allows for a measurement of the collimated photon flux present at the target, which is necessary for normalization, for example for cross section measurements. The photon monitoring system reduces the systematic error of the flux measurement to 5.7%.

Gamma Intensity Monitor

The Gamma Intensity Monitor (GIM) is a 14 cm × 14 cm × 28 cm block of fully absorbing lead glass that can measure the Cerenkov light produced by traversing photons. Due to radiation damage, it can not be kept inside of the beam continuously. It is therefore used to calibrate the Flux Monitor [52][66].

Flux Monitor

The Flux Monitor (FluMo) is a 5.0 cm × 5.0 cm × 0.5 cm plastic scintillator that is kept in the beam continuously and measures only a fraction of the full flux, but contrary to GIM, up to very high rates without radiation damage [52][66].

2.3 Trigger System

A trigger system distinguishes between low-energetic background and relevant physical events, only enabling recording of the latter. The trigger system has been implemented in a two-layered approach, consisting of local triggers and global triggers. Once the global trigger fired, the signals of all involved detectors need to be saved. This is done by the Data Aquisition. For a detailed description, also covering the corresponding electronic modules, see references [52], [67] and [68].

2.3.1 Local and Global Triggers

The first layer consists of local triggers, which engage when certain conditions within the same detector are met. A list of local trigger conditions is given in table 2.1.

Detector	Local Trigger Condition
Tagger	Coincidence of two or three adjacent channels
Scintillator Barrel	OR of all channels
BGO Calorimeter	Energy sum above low or high threshold
SciRi	OR of all channels
SciFi	OR of all channels
ToF	Coincidence between PMTs in a single bar
FluMo	Detector hit
GIM	Detector hit

Table 2.1: Table of detectors and corresponding local trigger conditions

The second layer is the global trigger, which engages once a certain combination of local trigger combinations is met. The global trigger conditions can be seen in table 2.2. Prior to datataking, a trigger alignment has to be performed, assuring that signals arising from a single event make it through the different trigger gates. This is described in chapter 3.1. The effective trigger rate is approximately 1 kHz [52].

Label	Global Trigger Condition
0	Tagger AND High BGO energy sum threshold ($E_{\mathrm{BGO}} \geq 120\,\mathrm{MeV}$)
1	Tagger AND SciRi AND Low BGO energy sum threshold ($E_{\mathrm{BGO}} \geq 75\,\mathrm{MeV}$)
3	Tagger AND SciRi AND SciFi AND ToF
4	Tagger AND SciFi AND ToF AND Low BGO energy sum threshold ($E_{\mathrm{BGO}} \geq 75\,\mathrm{MeV}$)

Table 2.2: Table of global trigger conditions

2.3.2 Data Aquisition

Once the global trigger fired, the signals of all involved detectors need to be saved, which is done by the Data Aquisition (DAQ). The analogue signals of the individual detectors are digitized and read out. During the readout process, a buffer is utilized, which allows the DAQ to still accept trigger attempts in the meantime. The raw data are then combined to a single event and saved in a ROOT file format on disk. The deadtime is heavily dependent on the running conditions of the experiment, a rough estimate is of the order of 200 ms to 400 ms [52][67][68]. From this stage on, the analysis using the ExPlORA framework starts, which is described in section 2.4.2.

2.4 Analysis Frameworks

Most of the analysis at BGOOD is performed using the ExPlORA framework, which is based on the ROOT framework. This chapter briefly describes the two frameworks and how the raw data that has been stored by the DAQ is converted to a usable format.

2.4.1 ROOT

ROOT is a C++ based framework that was developed at CERN and is widely used in high-energy physics. Prominent features of ROOT are efficient data structures, convenient functionalities for manipulating four-vectors, fitting routines and data visualization [69]. The raw data taken by the DAQ is saved in the ROOT file format. ROOT also provides the RooFit library, which is a toolkit for fitting to and modeling of event distributions in physics analyses [70].

2.4.2 ExPlORA

ExPlORA (Extended Pluggable Objectoriented ROOTified Analysis) was originally developed by the CBELSA/TAPS collaboration and subsequently adjusted for the use for BGOOD [71]. It converts the raw data stored by the DAQ into 'hits', 'clusters', 'tracks' and 'fitted tracks', which can then be used as a basis for more complex individualized analyses. A detailed description of ExPlORA can be found in reference [68].

As a first step, ExPlORA decodes the raw data and combines them with data from a PSQL database, mapping the raw channel numbers to the detector channels and applying channel-specific calibrations. Further information on the calibrations can be found in chapter 3.
On an event-by-event basis, detector-channel-specific data such as energy deposit in that channel, time and location are grouped into hit objects. Taking the BGO calorimeter as an example, a single hit would correspond to all information associated with a single crystal for a single event.
Detector-specific algorithms are then applied to all hits and sort them into clusters if they meet specific cut criteria. The energy, time and position of the cluster as a whole are then recalculated from its associated hits. For the BGO calorimeter, a cluster is a group of adjacent hits that are coincident in time and above a certain threshold energy.
Subsequently, different clusters are combined to tracks, which describe the trajectory of traversing particles. Generally speaking, in order to form tracks, clusters must be coincident in time and in proximity. A cluster from the BGO and a cluster from the barrel can be combined to a central track that is assumed to originate from the centre of the target if their relative angle is not too big.
Tracks can further be converted to 'fitted tracks' if an assumption of a specific particle type is made. For example, as the BGO calorimeter can only measure the energy, but not the momentum, the momentum that is assigned to the fitted track is a result of assuming that the signal originated from a certain particle type with known mass and utilizing energy-momentum conservation [67][68].
These established data types build a convenient base for more complex analyses of individual reaction channels.

ExPlORA is not only used to analyze real data. In order to perform accurate simulations of the experiment, a virtual three-dimensional model of the entire setup has been created, including the magnetic field and fringe field of the OD. ExPlORA first simulates the initial state of a reaction channel including the detection of the

post-bremsstrahlung electron. The conversion of the initial state to the final state can be modeled under the assumption that the transition probability follows a simple phase space distribution or under the assumption that it depends on a specific cross section. The subsequent particle decay is simulated using Monte Carlo methods. The passage through matter is accurately modeled using Geant4 [72], including the response of the detector material, the readout electronics and the trigger. From this stage, the data can then be analyzed just like real data [68].

CHAPTER 3

Detector Calibrations

In order to extract the DCS of the reaction $\gamma n \rightarrow K^+ \Sigma^-$, data is required off both a deuterium and a hydrogen target in order to separate reactions off the neutron and proton. For each target, data was acquired during an individual beamtime, as described in detail in chapter 4. Between the beamtimes, hardware conditions such as applied voltages, detector positions, magnetic field strengths and trigger efficiencies could potentially have altered. In order to enable an adequate comparison of the beamtimes, it must be ensured that all detectors are calibrated in the same way.

In the scope of this thesis, the calibrations of both beamtimes have been meticulously checked and recalibrated if necessary. This chapter shall give a brief overview over all relevant calibration procedures and the results for each beamtime.

3.1 Trigger Alignment and T0 Calibration

The trigger system is described in chapter 2.3. Only the basics of the associated calibrations shall be covered here, a thorough description can be found in reference [68]. At the beginning of each beamtime, adjusting the time information utilized by the trigger system is the very first and most important calibration that needs to be done. It must be distinguished between two crucial operations:

- **Aligning** corresponds to the delaying of signals in order to let them arrive simultaneously as inputs for a consecutive process, while the time information of the signals themselves stay unaffected.
- **Shifting** corresponds to the alteration of time information by adding an offset.

For the calibration of the time information originating from specific detector channels, the signals from the channels as well as the subsequent trigger signals are aligned first at a local and then at a global level, which is trivially termed 'trigger alignment', and then the time information are subsequently shifted to a common starting point, which is termed 'T0 calibration'. Once the data is taken, the trigger alignment can not be corrected in software afterwards, while the T0 calibration can.

Local Trigger Alignment

It must be assured that the signals from all individual detector channels arrive at the same time as an input for the detector-specific local triggers. Thus, the time spectra for the single channels are fitted with Gaussian distributions and the minimal necessary delays to move the prompt peaks to a common absolute time are registered for each individual channel, where 'prompt peaks' are defined as the signals arising from relevant physical events. The delays can be stored on the local trigger's field programmable gate array registers and adjusted via coarse time steps of 5 ns and fine time steps of 5/6 ns. They can then be applied to the signals. Once the detector channels are aligned as input for the local triggers, the local trigger logic is able to filter out events that match the local trigger conditions as listed in table 2.1.

A special case is the local trigger alignment for the tagger: During the beamtimes, dedicated runs are used to determine the time differences between tagger channel hits and FluMo hits, both relating to the same photon, which allows for a more precise determination of the necessary delays of the prompt peaks. Figure 3.1 illustrates the local trigger alignment using the tagger as an example for deuterium beamtime 2018-06. Prior to any alignment, individual tagger channels can vary in time by up to 10 ns. After alignment, they arrive with a jitter of 5/6 ns. Each picture shows the horizontal part of the tagger on its left and the vertical part of the tagger on its right side, which both have their own calibration, thus the spectra can show an offset to each other along the y axis.

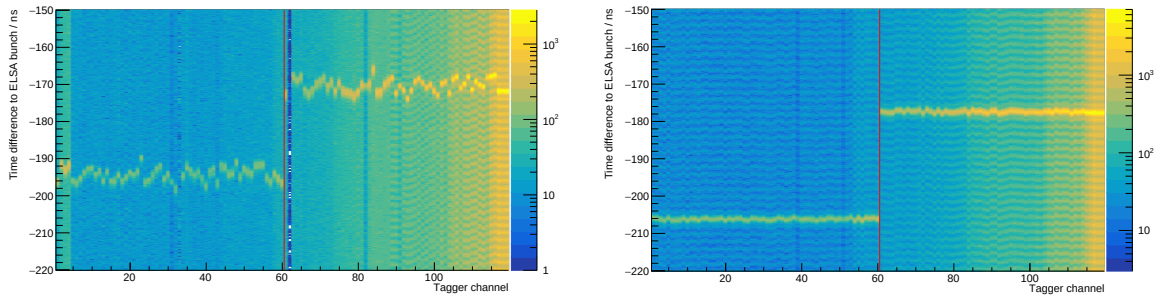

(a) Before local trigger alignment

(b) After local trigger alignment

Figure 3.1: Time distribution of the tagger channels (a) before local trigger alignment and (b) after local trigger alignment for deuterium beamtime 2018-06. The left part of each histogram describes the horizontal plane of the tagger and the right part describes the vertical plane, where each plane has its own calibration.

Global Trigger Alignment

Analogous to the alignment of the detector channels as an input for the local triggers, the local triggers are aligned as an input for a global trigger. The local trigger signals can be aligned via fine time steps of 5/6 ns on a dedicated global trigger time-to-digital converter (TDC). After the trigger alignment is completed, the global trigger logic can check whether one of the four trigger conditions listed in table 2.2 is fulfilled. If a condition is found to be true, a global trigger signal with a time jitter of about 5 ns, originating from the variance of the local trigger inputs, is provided and the recording of the corresponding event is enabled. The effective total trigger rate of the experiment is about 1 kHz.

Once the global trigger has fired, the time information of each single detector channel is saved on the corresponding detector TDC. Additionally, the time information of the activations of all single local triggers are saved on a DAQ TDC. Especially important is the time information of the tagger local trigger. Those information will be used in the subsequent T0 calibration.

T0 Calibration

During the T0 calibration, the time information of the single detector channels and the tagger local trigger are taken as an input. As the tagger has the finest time resolution, the tagger local trigger time, which is shown in figure 3.2, is specified as a first iteration of the starting point of the timescale of a reaction. The prompt peaks consistently have widths of below 5/6 ns. On a relative timescale, the tagger local trigger prompt peaks are located at zero.

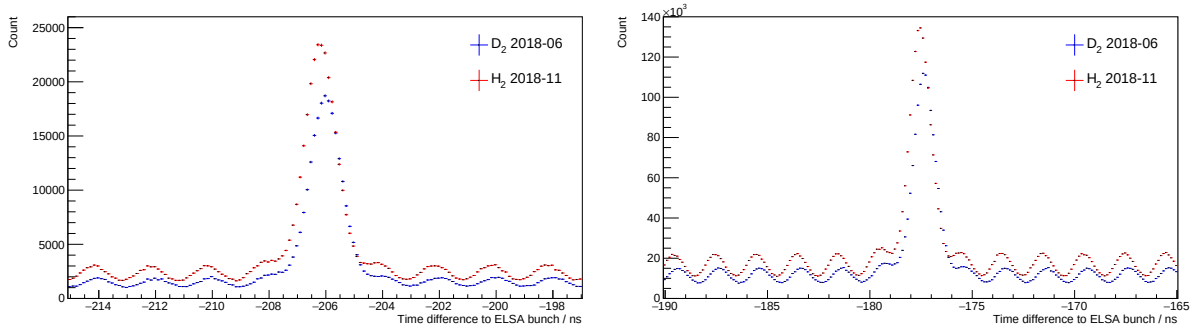

(a) Horizontal part of the tagger

(b) Vertical part of the tagger

Figure 3.2: Time distribution of the projection over all tagger channels (a) for the horizontal part and (b) for the vertical part of the tagger for both beamtimes.

The time information originating from the single detector channels are shifted by the absolute time of the tagger local trigger, setting them in relation to a common starting point, in what is called 'primary shift'. The resulting calibration values for the primary shift are stored on a software level. At this point, the time jitter of the signals is reduced to that of the tagger local trigger. Furthermore, as mentioned beforehand, during the beamtimes, dedicated runs are used to determine the time difference between tagger channel hits and FluMo hits, which can be used to determine the offsets of the individual tagger channels with respect to the tagger local trigger. These calibration values are also stored on a software level.

On an event-by-event basis, the calibration values of the tagger channels that participated in the prompt reaction are read in. As the tagger channels form double or triple coincidences, the mean offsets are calculated and applied to all the time information in what is called 'secondary shift'. This reduces the effective time jitter of the signals to below 5/6 ns [68].

After trigger alignment and T0 calibration, signals obtained from the same physical reaction are related to a common starting point in time. A careful reinvestigation of the trigger alignment and T0 calibration for the different beamtimes showed a general good match between beamtimes for almost all detectors. Spe-

cifically for the barrel, a small aberration is encountered: The local and global trigger timing for most of the barrel channels show a reflection of the trigger signal which occurs about 65 ns after the original signal. Fortunately, this reflection is unproblematic: As soon as a global trigger condition is fulfilled, detector-specific gates open and all events within the gates are saved. The reflection of the trigger signal arrives when the gate of the barrel, which has a width of 5 ns, has already closed, so there is no coincidence with the other detectors and the associated noise is not saved as an event. The reflection of the barrel trigger signal was found to be uncritical for an adequate comparison of beamtimes. This is confirmed by the fact that the DCS of the benchmark reaction $\gamma p \to \eta p$ was measured to be in accordance with the Bonn-Gatchina partial wave analysis for both beamtimes as described in section 3.6.

3.2 Trigger Efficiency

The trigger efficiencies of the detectors which are involved in building the global trigger conditions listed in table 2.2 can be determined by requiring a simultaneous firing of independent triggers and comparing them to the case where only a subset of them fired. The trigger efficiencies are first measured in situ for each beamtime and are then loaded into the simulation. The trigger efficiency $\zeta_{\text{BGO}}^{\text{High}}$ of the high BGO energy sum can be measured by taking following ratio:

$$\zeta_{\text{BGO}}^{\text{High}} = \frac{\text{High BGO energy sum AND Tagger AND SciRi AND SciFi AND ToF}}{\text{Tagger AND SciRi AND SciFi AND ToF}} .$$

Similarly, the trigger efficiency $\zeta_{\text{BGO}}^{\text{Low}}$ of the low BGO energy sum can be described as follows:

$$\zeta_{\text{BGO}}^{\text{Low}} = \frac{\text{Low BGO energy sum AND Tagger AND SciRi AND SciFi AND ToF}}{\text{Tagger AND SciRi AND SciFi AND ToF}} .$$

Both $\zeta_{\text{BGO}}^{\text{High}}$ and $\zeta_{\text{BGO}}^{\text{Low}}$ can be seen in figure 3.3 for both beamtimes. Between both beamtimes, $\zeta_{\text{BGO}}^{\text{High}}$ differs roughly by an absolute of 15%, while $\zeta_{\text{BGO}}^{\text{Low}}$ differs roughly by an absolute of 3%, the efficiencies of hydrogen beamtime 2018-11 being lower than the ones of deuterium beamtime 2018-06. The trigger efficiency ζ_{FS} of the forward track selection is described by following fraction:

$$\zeta_{\text{FS}} = \frac{\text{SciFi AND ToF AND Tagger AND Low BGO energy sum AND SciRi}}{\text{Tagger AND Low BGO energy sum AND SciRi}} . \tag{3.1}$$

The efficiency is dependent on the β of the forward going particles as shown in figure 3.4 for real data of both beamtimes and simulated data. The trigger efficiency of deuterium beamtime 2018-06 averages at about 96%, the one of hydrogen beamtime 2018-11 at 94% and the simulated one at 98%. To measure the trigger efficiency, a clean sample of forward-going protons is selected by placing a 2σ cut on the proton ToF mass prior to utilizing equation 3.1. For simulated data, this was done for the generated reaction $\gamma p \to \eta p$. The trigger efficiencies as functions of β can be described by linear fits and for each beamtime the real trigger efficiency can be compared to the simulated trigger efficiency. The simulated trigger efficiency is then adjusted to match the real one, the adjustment is approximately as little as an absolute 3%. The corrected trigger efficiencies ζ are all part of the overall reconstruction efficiency ϵ described in section 4.2.5.

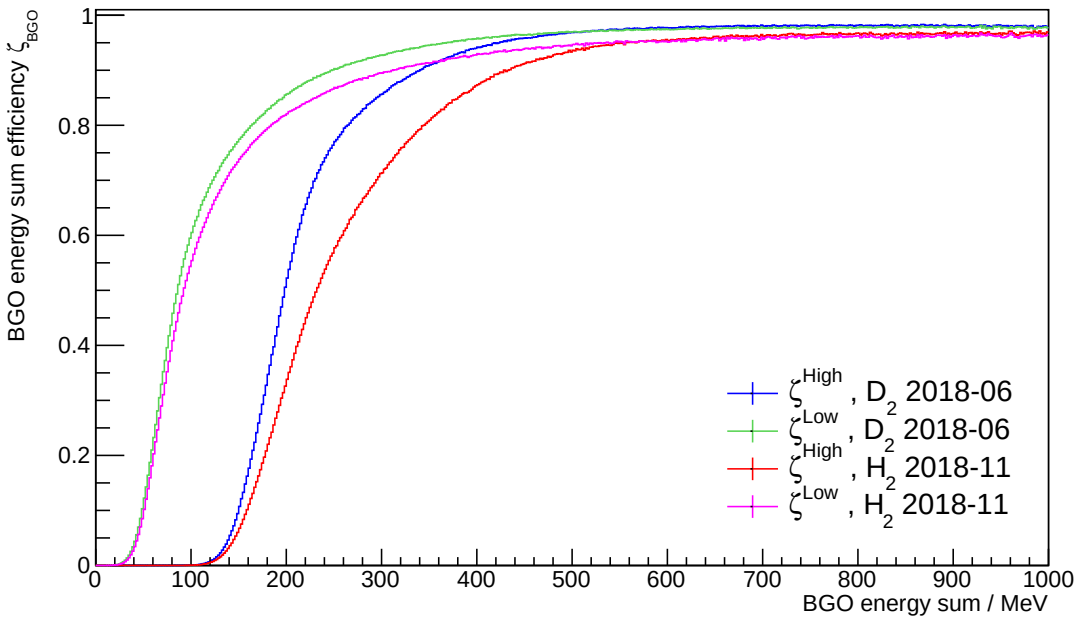

Figure 3.3: Trigger efficiency ζ_{BGO} of the high and low BGO energy sum for both beamtimes.

3.3 GIM and FluMo Calibration and Flux Determination

The photon tagging system has been described in section 2.2.1 and the photon monitoring system in section 2.2.4. Both are used to determine the applied photon flux which is needed to normalize the event count in order to measure the DCS. The determination of the photon flux is described in detail in reference [61]. The methodology has been thoroughly reinvestigated for both beamtimes in order to ensure that an adequate comparison is possible. Generally, the flux can be described as the product of the amount of electrons that cause coincidences in the tagging system, $N_{e^-\mathrm{coinc}}(E)$, and the tagging efficiency $P_\gamma(E)$:

$$N_\gamma(E) = N_{e^-\mathrm{coinc}}(E) \cdot P_\gamma(E) \ . \tag{3.2}$$

Determination of $N_{e^-\mathbf{coinc}}(E)$

First, the scaler of the tagging system provides the number of observed electrons depending on the electron's energy. This count is measured under the assumption that electrons only cause double coincidences in adjacent tagger channels.

Second, the preceding electron count is corrected for electrons that created triple coincidences in adjacent tagger channels and might have been previously misidentified as two independent double coincidences. This leads to a reduction of the electron count and provides the correct amount of detected electrons by the tagging system, $N_{e^-\mathrm{coinc}}(E)$.

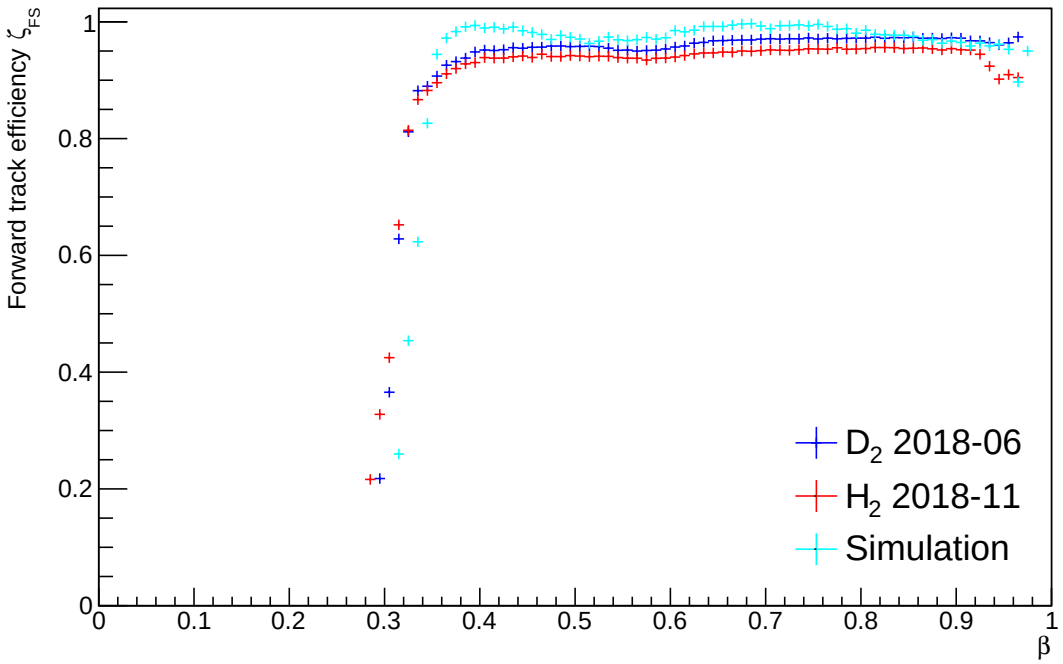

Figure 3.4: Forward track efficiency ζ_{FS} as a function of β. For the track selection a 2σ cut was placed on the proton ToF mass. For simulation, the reaction $\gamma p \to \eta p$ was generated.

Determination of $P_\gamma(E)$

Not all photons that were created in the bremsstrahlung process make it to the target, as they might be blocked during their passage through the first collimator, the sweeping magnet and the second collimator. The tagging efficiency can be determined by measuring the ratio of signals arising from post-bremsstrahlung electrons and the corresponding bremsstrahlung photons, whereas the electrons are detected in the tagger and the photons in the GIM, which is located at the end of the experiment:

$$P_\gamma^{\mathrm{GIM}}(E) = \frac{\text{Tagger(E) AND GIM}}{\text{Tagger(E)}} .$$

Cases in which the photon interacted with the target can be vetoed by observing whether a trigger fired. The GIM is highly sensitive to radiation and can only be used once a day with a low-intensity beam in order to avoid radiation damage. It provides a precise measurement of $P_\gamma(E)$ and can be moved in and out of the beam. To establish close to constant experimental conditions, a real-time observation of $P_\gamma(E)$ is desirable. For this purpose, FluMo is used.

FluMo is located near the end of the beamline in front of GIM. It detects photons via observation of pair-production within its scintillator material with a lower photon detection efficiency than GIM, but is not susceptible to radiation damage and can therefore be used for real-time measurements of $P_\gamma(E)$ once its efficiency is known. In order to assess the FluMo efficiency, dedicated runs are utilized for the measurement

of the ratio of coincidences between Tagger, GIM and FluMo and solely Tagger and GIM:

$$\text{FluMo Eff.}(E) = \frac{\text{Tagger(E) AND GIM AND FluMo}}{\text{Tagger(E) AND GIM}} .$$

Once the FluMo efficiency is known, FluMo can be used to measure $P_\gamma(E)$ in real-time as described by following equation:

$$P_\gamma^{\text{FluMo}}(E) = \frac{1}{\text{FluMo Eff. (E)}} \cdot \frac{\text{Tagger(E) AND FluMo}}{\text{Tagger(E)}} .$$

A comparison of $P_\gamma^{\text{FluMo}}(E)$ for the two beamtimes can be seen in figure 3.5. The shown spectra are averages over five runs taken at different days. The slight drop-off for higher energies originates from the beam extraction from ELSA, as uncorrelated electrons are able to enter the tagger. Both beamtimes have very similar values of $P_\gamma^{\text{FluMo}}(E)$, as beamtime 2018-06 has a mean value of $\bar{P}_\gamma = (79.38 \pm 0.18)\%$ and beamtime 2018-11 of $\bar{P}_\gamma = (83.43 \pm 0.29)\%$. To ensure adequate calibration during the beamtimes, the calibration runs are taken at regular intervals.

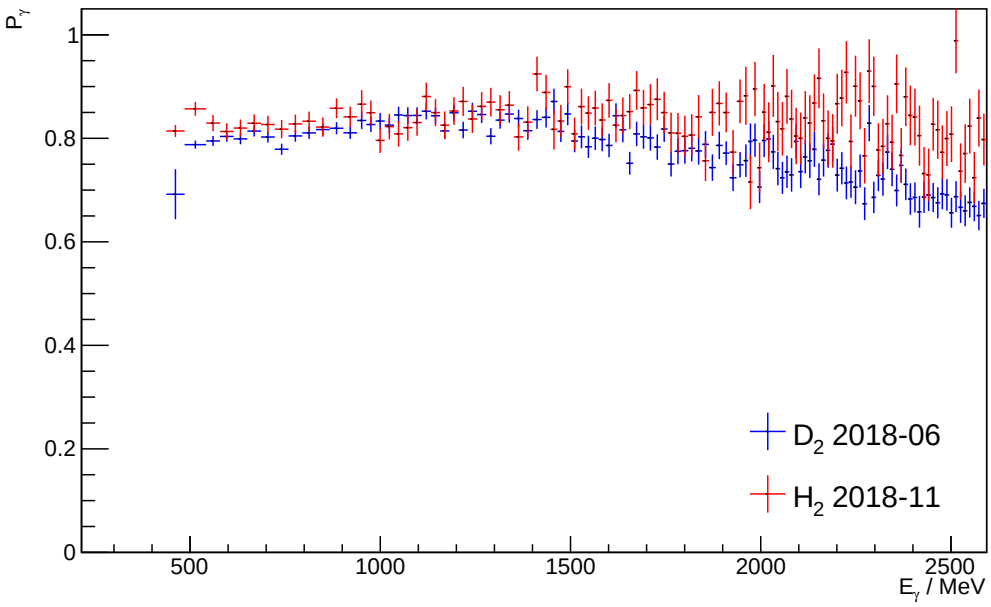

Figure 3.5: $P_\gamma^{\text{FluMo}}(E)$ measured by FluMo and corrected for double-counting effects for both beamtimes. The shown spectra are averages over five runs taken at different days.

At this point, the photon flux can be described by equation 3.2. The resulting photon flux distributions are described later in section 4.2.3.

3.4 BGO Calibration

As particles traverse the BGO calorimeter, they deposit their energies in the individual BGO crystals, producing analogue signals. These signals are calibrated in three steps.

Calibration with ^{22}Na Source

The signals are read out by a combination of PMTs and analog-to-digital converters (ADCs). The energy scales of the ADCs are segmented in discrete channels that must be mapped to the corresponding true energies. Therefore, ^{22}Na sources are placed between the MWPC and the barrel. The ^{22}Na sources undergo β^+ decay and turn into ^{22}Ne*, which subsequently returns to its ground state by emitting a photon of 1 274.530 MeV. The positron from the β^+ decay recombines and leads to a twofold energy deposit of 0.511 MeV within the crystals. By fitting to the corresponding uncalibrated ADC channel distribution, which can be seen in figure 3.6, one knows the ADC peak positions that relate to these energy deposits. Thus, one can apply a scaling factor to the ADC channel distribution in order to convert to an energy scale. This calibration is done prior to the datataking, while the attenuation of the BGO signal is set to zero. During datataking , an attenuation factor of 12db ≈ 4 has to be applied to the signal. As a result, the overall scaling factor must be multiplied by about $1/4$.

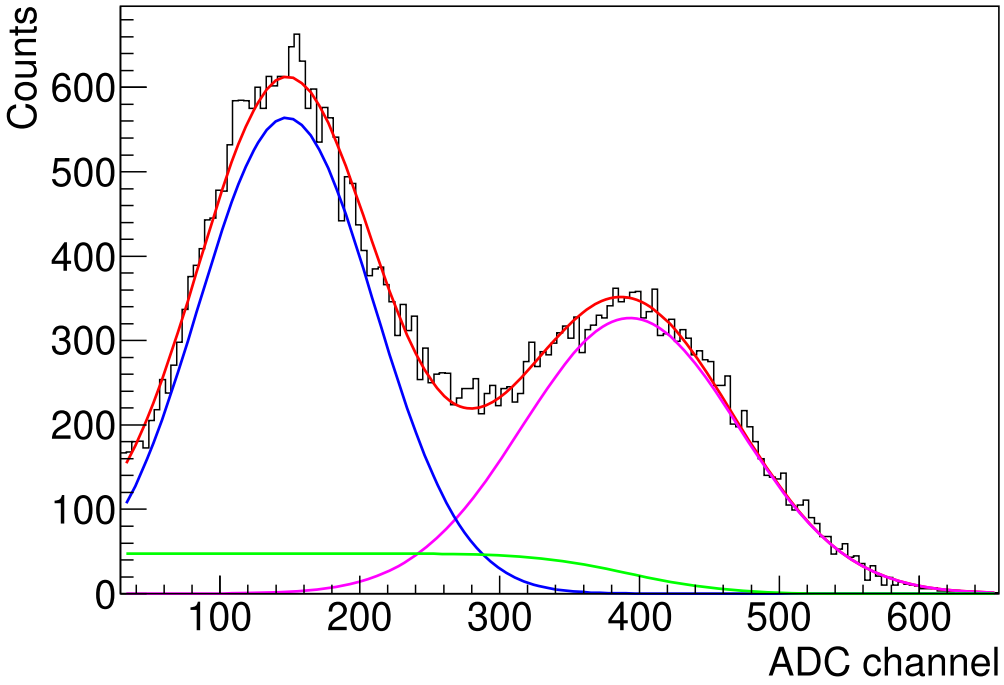

Figure 3.6: ADC channel distribution of a single BGO crystal. The left peak (blue Gaussian) corresponds to the 0.511 MeV energy deposit and the right peak (magenta Gaussian) to the 1 274.530 MeV energy deposit stemming from the ^{22}Ne* decay. The red fit function is the sum of the two Gaussians, while the green function is the corresponding error function [52].

Run-specific Calibration

As a second step, after datataking, the invariant π^0 mass is reconstructed for the reaction $\gamma p \to p\pi^0 \to p\gamma\gamma$. In order to achieve this, the two photons are detected in the BGO and their four-momenta are summed. Placing a cut on the missing mass to the π^0, which corresponds to the proton mass, helps to improve the invariant π^0 mass resolution. For each individual run, a Gaussian fit to the π^0 peak is performed. Comparing the mean value to the true π^0 mass, one can determine a run-specific scaling factor which shifts the energy deposit in the BGO to the expected values. This calibration serves as a first iteration prior to the crystal-specific calibration.

Crystal-specific Calibration

After the run-specific calibration, a crystal-index-specific calibration for each of the 480 individual BGO crystals is performed. The π^0 mass is reconstructed analogously to the run-specific calibration and for each event each crystal that is involved in the reconstruction is noted. It is geometry-dependent and slightly drops off at the outer crowns of the BGO ball, which is especially prominent for longer targets, being caused by the fact that the tracking hypothesis assumes that the photons ideally originate from the target centre. The reconstructed π^0 mass spectrum can be reproduced in simulated data, which allows for a correction of the real data in order to match the simulated ones. Figure 3.7 shows the crystal-index-dependent reconstructed π^0 mass after calibration, showing a good match between real data and simulation.

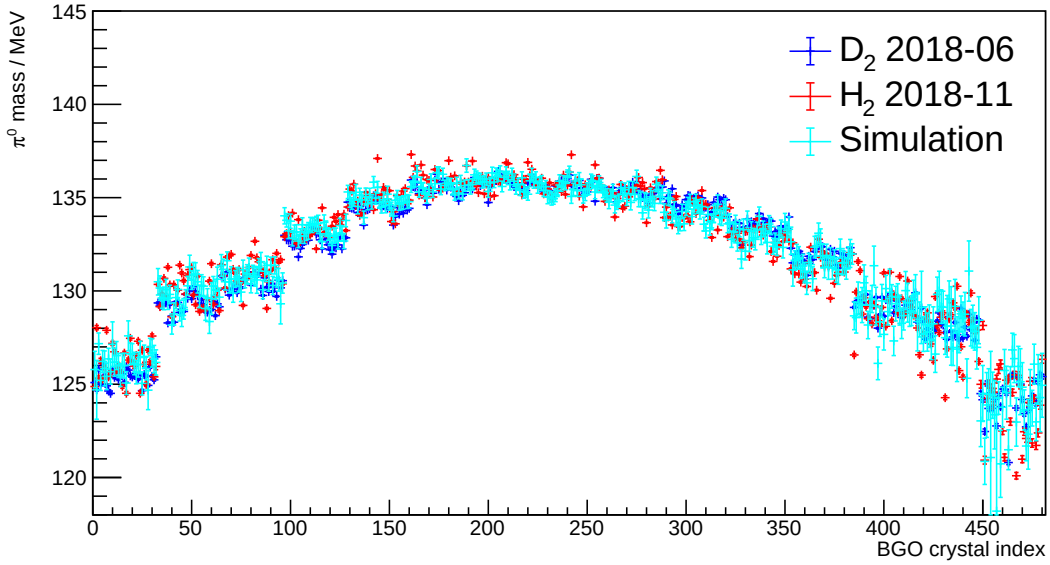

Figure 3.7: Reconstructed π^0 mass depending on BGO crystal index for both beamtimes and simulation.

At the time of writing, the feasability of a proper barrel energy calibration is still a matter of investigation.

3.5 Forward Spectrometer Calibration

In order to calibrate the momentum and β reconstruction achieved with the FS, one must consider different calibrations for its individual parts.

Run-specific Momentum Calibration

A run-specific momentum calibration is performed by investigating the invariant mass distribution of positively charged particles and fitting a Gaussian to the indistinguishable proton peak for each single run. By comparing the Gaussian mean to the true proton mass, one can determine a run-specific correction factor $\frac{m_p^{\text{true}}}{m_p^{\text{measured}}}$ for the momentum of particles detected in the FS. The correction factors are of the order of $\sim 1\%$ and are shown in figure 3.8 for the run numbers of both beamtimes. The correction factors tend to be a little higher at the very beginning of beamtimes, as these periods are not used for datataking, but for initialization of the running conditions of the experiment. Furthermore, the correction factors oscillate along with the day-and-night cycle and the corresponding temperature changes in the experimental area.

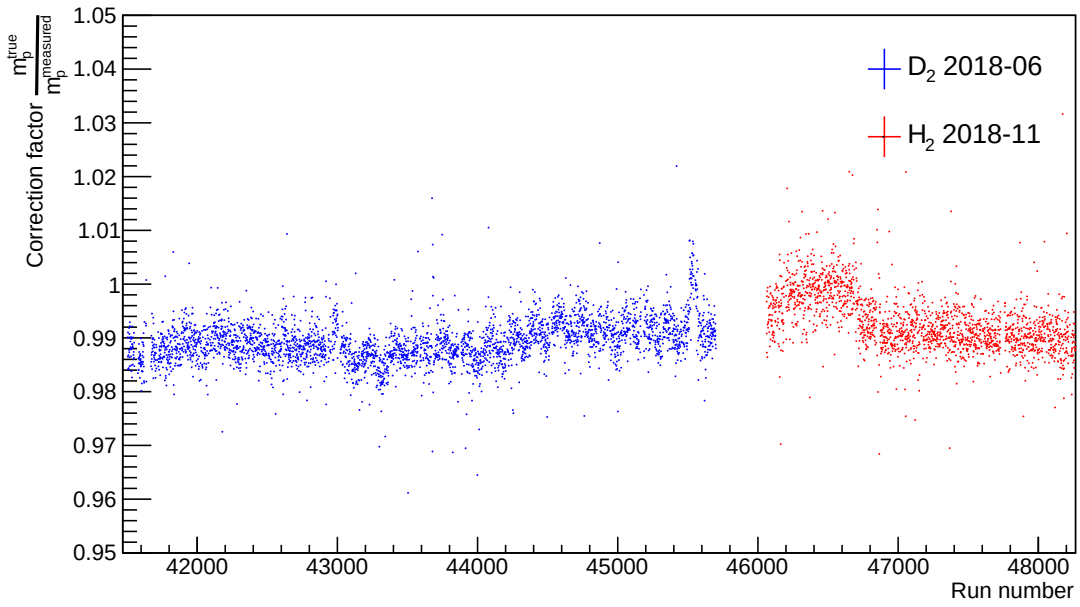

Figure 3.8: Run-specific momentum correction factors $\frac{m_p^{\text{true}}}{m_p^{\text{measured}}}$ for the run numbers of both beamtimes.

Angular-specific and Momentum-specific Momentum Calibration

The measured particle momentum is dependent on its trajectory through the magnetic field, parameterized by its incident horizontal angle X, vertical angle Y and momentum p. It is possible that the magnetic field strength of the OD is mildly anisotropic and slightly changes over a long time frame.
For calibration, one can calculate associated momentum scaling factors by plotting the Gaussian mean of the

proton peak as a total function of X, Y and p and comparing it to the true proton mass. To gain sufficient statistics for this procedure, the magnetic field, which effectively ranges from $-10°$ to $10°$ in both the horizontal and vertical plane, is discretized into 20 bins of X and Y, respectively. For each XY combination a ToF mass vs p histogram is filled. The ToF mass as a function of p can then be fitted by a first degree polynomial. Figures 3.9, 3.10 and 3.11 show a comparison of the ToF mass before and after calibration depending on the X angle, Y angle and p, respectively. The true proton mass is shown as a red line. It is apparent that the calibration procedure removes the X, Y and p dependency of the measured proton momentum and thus the dependency of the measured proton mass.
Note that for the aforementioned method the X and Y angles are discretized, while real particles of course have a continuous angular distribution. For a particle that incides at an angle in-between X or in-between Y values, one can calculate an adequate momentum scaling factor by taking the four closest XY pairs in the discretized XY grid, determining their associated momentum scaling factors and then performing a hyperbolic interpolation, which weights the scalingfactor of the particle by its distance to each XY pair. As depicted in figure 3.12, after calibration, when the average over both beamtimes is taken, a Gaussian mean of $\mu = (934.39 \pm 0.04)$ MeV with $\sigma = (62.66 \pm 0.05)$ MeV is achieved for the reconstructed proton mass, which is a resolution of 6.71%.

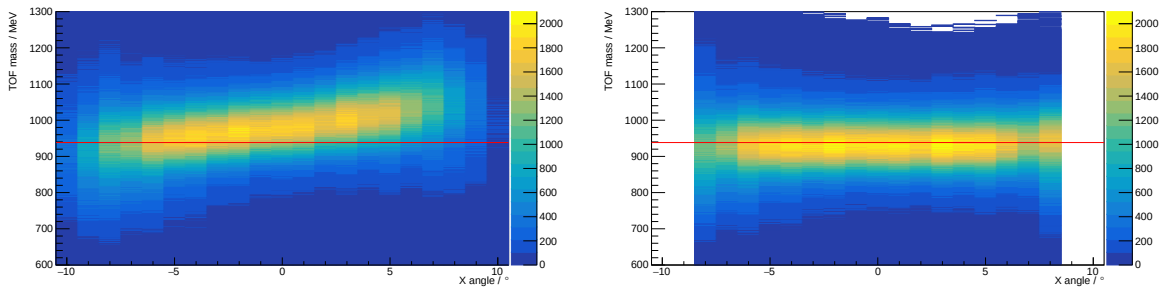

(a) Before calibration

(b) After calibration

Figure 3.9: ToF mass vs X angle for deuterium beamtime 2018-06 with true proton mass as the red line.

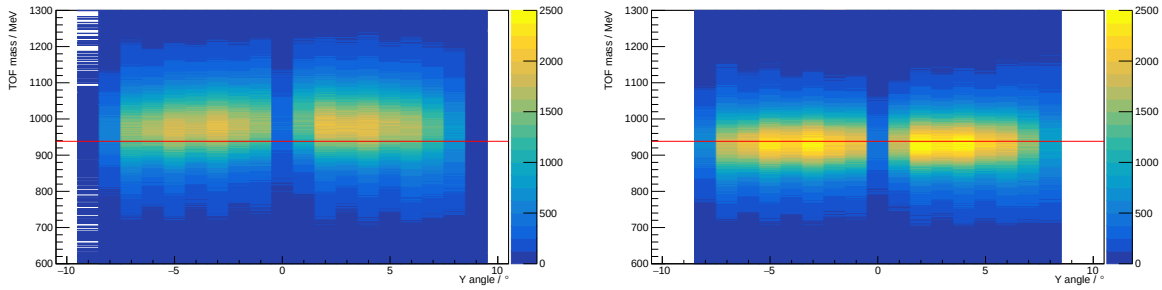

(a) Before calibration

(b) After calibration

Figure 3.10: ToF mass vs Y angle for deuterium beamtime 2018-06 with true proton mass as the red line.

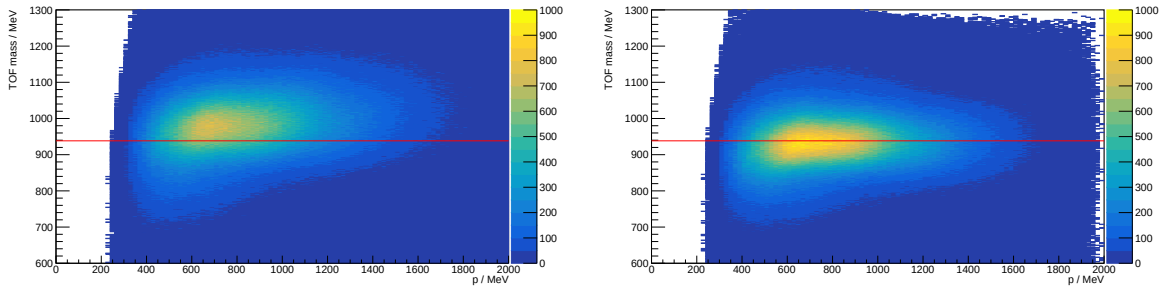

(a) Before calibration

(b) After calibration

Figure 3.11: ToF mass vs p for deuterium beamtime 2018-06 with true proton mass as the red line.

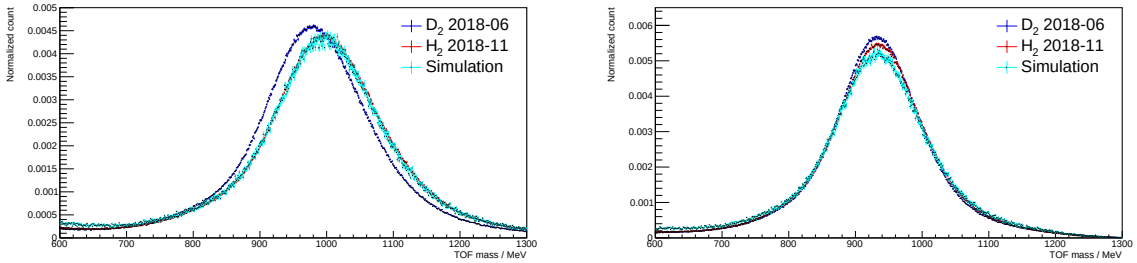

(a) Before calibration

(b) After calibration

Figure 3.12: ToF mass for both beamtimes and simulation (a) before calibration and (b) after calibration.

ToF Wall Calibration

Forward tracks are reconstructed as described in section 2.2.3. The ToF cluster's position and time signals are calibrated by measuring the discrepancy between the reconstructed particle's trajectory and the actual measured cluster data with respect to each individual ToF bar index. The offsets are determined by Gaussian fits and can then be applied to improve the signals provided by each ToF bar. The horizontal and vertical ToF cluster positions are then centred around zero as illustrated in figure 3.13, which corresponds to ToF1 for a single run of beamtime 2018-06. The other ToF walls look analogous for both utilized beamtimes. Additionally to the calibration per individual ToF wall, a check of the time differences between the three ToF walls was performed by comparing real data to simulated data. No systematic aberrations have been found.

3.6 Differential Cross Section of $\gamma p \rightarrow \eta p$

The DCS of the reaction $\gamma p \rightarrow \eta p$ is a well understood quantity [73][74][75][76][77] and can be used to cross-check whether any systematic uncertainties are still present in the utilized datasets after calibration. For comparison to the reaction $\gamma n \rightarrow K^+\Sigma^-$, the angular range of the K^+ of $\cos(\theta_{CM}) > 0.9$ is compared to the angular range of the proton of $\cos(\theta_{CM}) > 0.9$, implying an η angle of $\cos(\theta_{CM}) < -0.9$. More specifically, the proton is observed in the FS and the η is observed in the BGO via the 2γ decay. A rudimentary analysis is carried out, applying fixed W-independent 2σ cuts on the proton ToF mass, the invariant

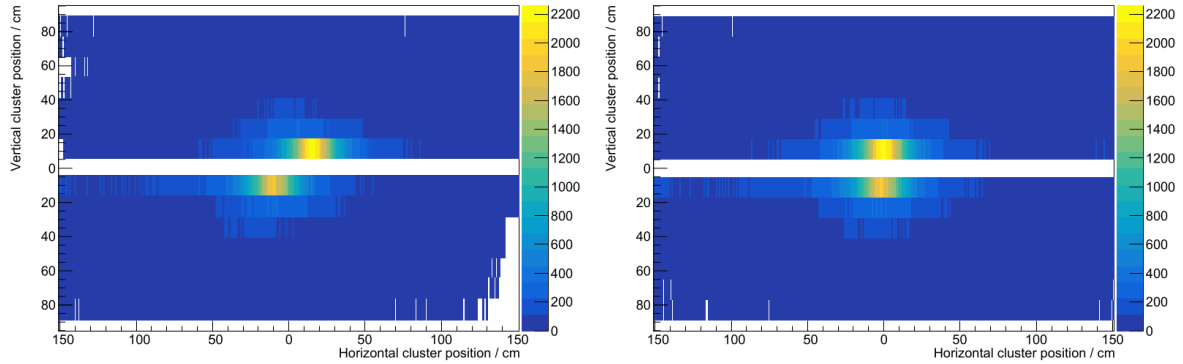

(a) Before calibration

(b) After calibration

Figure 3.13: ToF1 cluster horizontal and vertical position (a) before calibration and (b) after calibration for a single run of beamtime 2018-06.

η mass from the 2γ decay, the missing mass to the proton and the missing mass to the η. As the purpose of this analysis is to perform a rough cross-check of the systematic errors of the utilized datasets, an intricate fine-tuning of the cuts and modeling of the backgrounds depending on W is omitted. Figure 3.14 shows the DCS of the reaction $\gamma p \to \eta p$ as a function of W. For reference, the Bonn-Gatchina [73] model is shown as the black dashed line and the McNicoll et al. [76] data as the green data points.

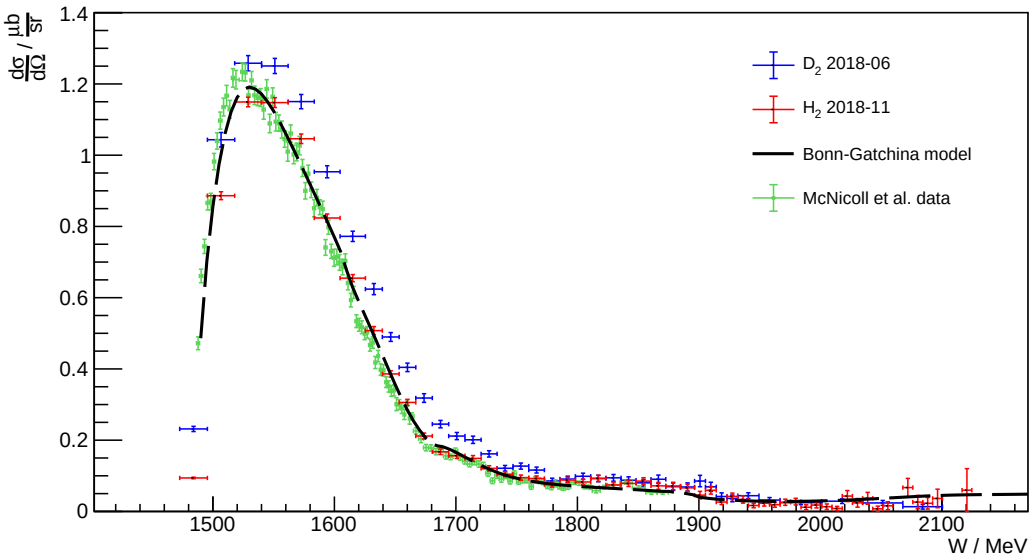

Figure 3.14: DCS of the reaction $\gamma p \to \eta p$ depending on W. The Bonn-Gatchina [73] model is shown as the black dashed line and the McNicoll et al. [76] data as the green data points.

Both the data from the deuterium beamtime and from the hydrogen beamtime show good agreement with the Bonn-Gatchina model and McNicoll et al. data. The small deviation of the deuterium dataset to the Bonn-Gatchina model of about 5% is consistent with the fact that no background subtraction was performed. Overall, the DCS measurement of the benchmark reaction $\gamma p \rightarrow \eta p$ confirms that no unknown systematic uncertainties are present in the datasets.

CHAPTER 4

Analysis

The aim of this thesis is the measurement of the DCS of the reaction $\gamma n \to K^+\Sigma^-$ in an angular range of $\cos(\theta_{\mathrm{CM}}) > 0.9$, which shall be described in this chapter. The next section 4.1 gives an overview of the applied methodology, while the subsequent sections depict the specific steps. The final result will then be presented in chapter 6.

4.1 Methodology

The differential cross section can commonly be determined as follows:

$$\left(\frac{d\sigma}{d\Omega}\right)_{K^+\Sigma^-}(W,\theta_{\mathrm{CM}}) = \frac{N_{K^+\Sigma^-}(W,\theta_{\mathrm{CM}})}{N_\gamma(W)\cdot\rho_n\cdot\epsilon(W,\theta_{\mathrm{CM}})\cdot\Omega} \tag{4.1}$$

with

$N_{K^+\Sigma^-}(W,\theta_{\mathrm{CM}})$	:	Number of measured $\gamma n \to K^+\Sigma^-$ reactions,
$N_\gamma(W)$	:	Integrated photon flux,
ρ_n	:	Neutron area density of the target,
$\epsilon(W,\theta_{\mathrm{CM}})$	:	Reconstruction efficiency,
Ω	:	Solid angle element.

The centre-of-mass (CM) energy is denoted with 'W' and the CM angle with 'θ_{CM}'. The measurement of the DCS of the reaction $\gamma n \to K^+\Sigma^-$ requires a neutron in the initial state. As a pure neutron target does not exist, one utilizes the closest viable candidate, which is a liquid deuterium target. Compared to twice the Fermi momentum of the deuteron, the momentum transfer of the incident photon to the target is much larger, meaning that coherent reactions off the deuteron as a whole are suppressed and incoherent reactions off the constituent neutron and proton dominate. Thus, the normalized count that is measured when using a deuteron target can be described as the incoherent sum of the normalized counts originating from neutron and proton, respectively, where the reactions off the neutron produce both signal and background and those off the proton only produce background. Additionally, one must consider the contribution of potential final state interactions (FSI) between the produced particles and the spectator nucleon. The relation between all of these individual terms is described by equation 4.2, where the superscripts denote the initial state target

particles, the subscripts denote signal (S), background (BG) and FSI contributions and for simplicity, the dependencies on W and θ_{CM} are omitted in the notation:

$$M^{d}_{\mathrm{S+BG}} = M^{p}_{\mathrm{BG}} + M^{n}_{\mathrm{BG}} + M^{n}_{\mathrm{S}} + A^{p,n}_{\mathrm{FSI}} \,, \tag{4.2}$$

$$M^{n}_{\mathrm{S}} = M^{d}_{\mathrm{S+BG}} - \left\{M^{p}_{\mathrm{BG}} + M^{n}_{\mathrm{BG}} + A^{p,n}_{\mathrm{FSI}}\right\} \,, \tag{4.3}$$

with

$M^{d}_{\mathrm{S+BG}}$	:	Normalized count measured when using a deuteron target,
M^{p}_{BG}	:	Normalized count originating from background reactions off the proton,
M^{n}_{BG}	:	Normalized count originating from background reactions off the neutron,
M^{n}_{S}	:	Normalized count originating from signal reactions off the neutron,
$A^{p,n}_{\mathrm{FSI}}$	:	Effective parametrization of FSI effects as a normalized count.

Rearranging the terms in equation 4.2 leads to equation 4.3, which is an expression for the desired normalized count of the signal reaction. The individual terms shall be explained here more extensively:

$M^{d}_{\mathrm{S+BG}}$ is the normalized count that is measured when using a deuteron target including all signal and background contributions. Appropriate selection criteria are chosen to maximize the signal-to-noise ratio (SNR) in favour of the desired signal reaction $\gamma n \to K^{+}\Sigma^{-}$ as described in the subsequent sections. In summary, this includes selecting events where the K^{+} is seen in the FS, the π^{-} resulting from the Σ^{-} decay in the BGO and the neutron resulting from the Σ^{-} decay goes undetected. The allowed energies and momenta of the π^{-} are then restricted according to reconstructed kinematics. Furthermore, selection criteria on the missing mass (MM) to $K^{+}\pi^{-}$ as well as to the MM to K^{+} are used. Furthermore, a maximum likelihood fit to the K^{+} ToF mass spectrum is applied to extract the yield of $K^{+}Y$ candidates. The measurement of $M^{d}_{\mathrm{S+BG}}$ is explained in section 4.2.

M^{p}_{BG} is the normalized count that originates from background reactions off the proton. The reaction channels that contribute significantly are:

$$\begin{aligned} \gamma p \to & K^{+}\Lambda \\ & K^{+}\Sigma^{0} \\ & K^{+}\Sigma^{0}(1385) \end{aligned}$$

This term can be measured by performing the same analysis that is carried out to measure $M^{d}_{\mathrm{S+BG}}$, but this time on a pure proton target, where a correction is applied that takes care of the fact that the nucleons inside the deuteron carry a Fermi momentum, while the pure free proton does not. This background contribution will be subtracted as described by equation 4.3. Its measurement is explained in section 4.2 with the Fermi momentum correction in subsection 4.2.1.

M^{n}_{BG} is the normalized count that originates from background reactions off the neutron. The most con-

tributing reaction channel is expected to be:

$$\gamma n \rightarrow K^+ \Sigma^-(1385)$$

The selection criteria that were applied for the measurement of $M^d_{\mathrm{S+BG}}$ will be chosen tight enough to minimize the influence of this reaction channel. As the contributions of background reactions off the neutron can not directly be measured in this analysis, they will be modeled in the Geant4 simulation, which is described in section 4.3, and expressed as a systematic uncertainty to the desired DCS measurement of $K^+\Sigma^-$, as depicted in chapter 5. By doing so, the term M^n_{BG} can be taken out of equation 4.3.

$A^{p,n}_{\mathrm{FSI}}$ is a parametrization of potential final state interaction effects as a normalized count. When using a deuteron target, the wave functions of the particles that were produced can potentially interfere constructively or destructively with the one of the remaining spectator nucleon. As such effects can increase or decrease the measured normalized count, the term $A^{p,n}_{\mathrm{FSI}}$ is used as an *effective parametrization* of FSI effects as a normalized count, meaning it can be positive or negative. As $A^{p,n}_{\mathrm{FSI}}$ can not be measured directly, the relative contribution of FSI to the DCS of $K^+\Sigma^-$ will be estimated by relying on theoretical calculations as described in section 4.4. Interpreting the final DCS under the consideration that it might be affected by FSI to the estimated extent allows for taking $A^{p,n}_{\mathrm{FSI}}$ out of equation 4.3. As the FSI are an intrinsic property of any DCS measurement on the deuteron, they will not be treated as a systematic uncertainty in the strictest sense.

As the terms M^n_{BG} and $A^{p,n}_{\mathrm{FSI}}$ can be taken out of equation 4.3, it reduces to:

$$M^n_{\mathrm{S}} = M^d_{\mathrm{S+BG}} - M^p_{\mathrm{BG}} \,. \tag{4.4}$$

Normalized counts are denoted by 'M' and not-normalized counts by 'N'. In equation 4.4, the normalization is achieved as follows:

$$\frac{N^n_{\mathrm{S}}}{N^n_\gamma \rho_n} = \frac{N^d_{\mathrm{S+BG}}}{N^n_\gamma \rho_n} - \frac{N^p_{\mathrm{BG}}}{N^p_\gamma \rho_p} \cdot \frac{\zeta^d}{\zeta^p} \,. \tag{4.5}$$

The event counts N_{K^+Y} are divided by the integrated photon fluxes N_γ and target area densities ρ of the respective beamtimes. Note that $N^d_\gamma = N^n_\gamma$ and $\rho_d = \rho_n$. In section 3.2, it has been explained that the trigger efficiencies of hydrogen beamtime 2018-11 are slightly lower than those of deuterium beamtime 2018-06. This effect is corrected by scaling the event count N^p_{BG} by the ratio of the relevant trigger efficiencies $\frac{\zeta^d}{\zeta^p}$ of the two beamtimes.

Dividing the normalized count M^n_{S} by the reconstruction efficiency ϵ and the solid angle element Ω and using the definition of the DCS given in equation 4.1 leads to the final expression for the DCS of the desired signal reaction $\gamma n \rightarrow K^+\Sigma^-$:

$$\left(\frac{d\sigma}{d\Omega}\right)^n_{\mathrm{S}} = \frac{M^n_{\mathrm{S}}}{\epsilon\,\Omega} = \frac{N^n_{\mathrm{S}}}{N_\gamma \rho_n \epsilon\,\Omega} \,. \tag{4.6}$$

To summarize, the chronological order of the analysis is the following:

1. Measuring $M^d_{\mathrm{S+BG}}$ for deuterium beamtime 2018-06
2. Measuring M^p_{BG} for hydrogen beamtime 2018-11 with Fermi momentum correction

3. Calculating M_{S}^{n} by subtracting the terms as described in formula 4.4
4. Calculating $\left(\frac{d\sigma}{d\Omega}\right)_{\mathrm{S}}^{n}$ by dividing by the reconstruction efficiency and solid angle element as described in formula 4.6
5. Modeling the contribution of M_{BG}^{n} to the systematic uncertainty in the Geant4 simulation
6. Estimating the contribution of $A_{\mathrm{FSI}}^{p,n}$ to the DCS based on theoretical calculations
7. Determining the contribution of other sources to the systematic uncertainty

These steps are illustrated in appendix B in flow diagram B.1, whereas steps one and two are described in even more detail in flow diagram B.2.
Steps one to four are explained in detail in the following section 4.2. Steps five and six will be elicited in sections 4.3 and 4.4, while step seven will be described in chapter 5 together with a list of all systematic uncertainties. The final results will be presented and interpreted in chapter 6. A summary and outlook is provided in chapter 7.

4.2 Measurement of the Differential Cross Section

This section explains how the DCS of the reaction $\gamma n \to K^+ \Sigma^-$ is determined by performing a measurement of a normalized event yield on a deuteron target utilizing deuterium beamtime 2018-06, then performing an almost identical measurement on a hydrogen target utilizing hydrogen beamtime 2018-11 and using it to subtract the contribution of background reactions off the proton as previously described by equation 4.4. The resulting normalized yield is then divided by the reconstruction efficiency and solid angle element as previously described by equation 4.6.
The selection criteria and methods applied to the deuterium dataset are identical to the ones applied to the hydrogen dataset with exception of the Fermi momentum correction. As the Fermi momentum correction affects different stages of the analysis, such as the W binning, MM resolution and integrated photon flux, from a didactical point of view it makes sense to cover the Fermi momentum correction prior to the other topics in the following section 4.2.1.

4.2.1 Fermi Momentum Correction

The deuteron is a bound state of a proton and a neutron with a binding energy of $E_{\text{bind}} = 2.22\,\text{MeV}$ [78]. Various models have been developed to describe the fundamental nucleon-nucleon (NN) potential that gives rise to the experimentally observable behaviour, such as the Paris [79], Nijmegen [80] and Argonne [81] potential. The NN potential that provides the best description of the world dataset with $\chi^2 = 1.02$ is the CD-Bonn potential [78].

The CD-Bonn potential utilizes field-theoretical perturbation theory to describe the NN interaction. The lowest order contributions to the NN interaction are one-meson exchange diagrams, where the CD-Bonn model allows for π, ρ and ω as exchange mesons and introduces two effective scalar-isoscalar σ mesons. Furthermore, several irreducible multi-meson diagrams exist. Most prominently, these consist of 2π exchange with intermediate Δ isobars, which provides the intermediate-range attraction of the nuclear force, but also $\pi\rho$, 3π and 4π exchanges. Some of these diagrams are able to partially cancel one another. The CD-Bonn model gives an accurate description of the charge dependence (CD) of the NN interaction. It is able to describe the charge-symmetry breaking via the nucleon mass splitting and the charge-independence breaking via the pion mass splitting. As the proton and the neutron inside the deuteron are both fermions, they obey Fermi statistics and possess corresponding momenta, which will colloquially be termed 'Fermi momenta'. The probability distribution of the Fermi momentum of a single nucleon as a result of the CD-Bonn NN potential is shown in figure 4.1. The *average* value of the momentum is approximately $|\vec{p}_{\text{F}}| = 94\,\text{MeV}$, while the *most likely* value of the momentum is about $|\vec{p}_{\text{F}}| = 55\,\text{MeV}$ [78].
This analysis measures the DCS of $\gamma n \to K^+ \Sigma^-$ off the bound neutron, which gives rise to background contributions off the bound proton. These background contributions are modeled by performing the same analysis on a static proton target. As the bound proton inherits Fermi momentum while the static proton does not, the data stemming from the static proton target must be corrected for Fermi-momentum-related effects in order to match the data stemming from the bound proton target. The subsequent paragraphs will show how the Fermi momentum is generally included in the simulation, how the real static proton data has to be corrected accordingly and how specific Fermi-momentum-related complications are fixed.

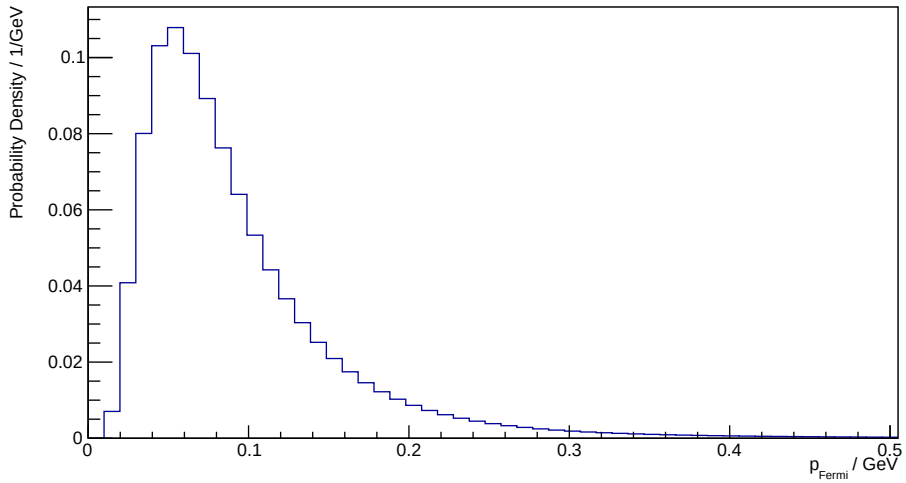

Figure 4.1: Probability distribution of the Fermi momentum of a single nucleon inside the deuteron as described by the CD-Bonn NN potential [78].

Modeling of Fermi Momentum in Simulation

When incoherent reactions off the deuteron are simulated, the Fermi momentum is included in simulation as follows:

1. A random beam energy E_γ is generated, whereas the probability distribution follows a $\frac{1}{E_\gamma}$ shape as expected for bremsstrahlung processes. The corresponding four-momentum of the photon is created.

2. A random Fermi momentum is generated, whereas the probability distribution follows the shape of figure 4.1, which is a result of the CD-Bonn NN potential. This value describes the total magnitude of the Fermi momentum, $|\vec{p}_\mathrm{F}|$.

3. A random three-dimensional unit vector is generated in spherical coordinates using the angles θ and ϕ:

$$\theta = \arccos(R) \,, \tag{4.7}$$

$$\phi = 2\pi r \,. \tag{4.8}$$

   Here, R is a random variable uniformly distributed between $[-1, 1]$ and r a random variable uniformly distributed between $[0, 1)$. The resulting distribution is illustrated in figure 4.2 in cartesian coordinates.

4. The magnitude of the unit vector is set to the previously generated Fermi momentum $|\vec{p}_\mathrm{F}|$, resulting in the three-momentum $\vec{p}_\mathrm{F}$. This is used as the momentum component of the four-momentum of the initial state, while $\sqrt{m^2 + \vec{p}_\mathrm{F}^2}$ is used as the energy component.

5. Adding up the four-momenta of the incoming photon and of the moving target results in the four-momentum of the initial state. It is used as a boost vector to Lorentz-transform the four-momenta of the incoming photon and the moving target into the CM frame.

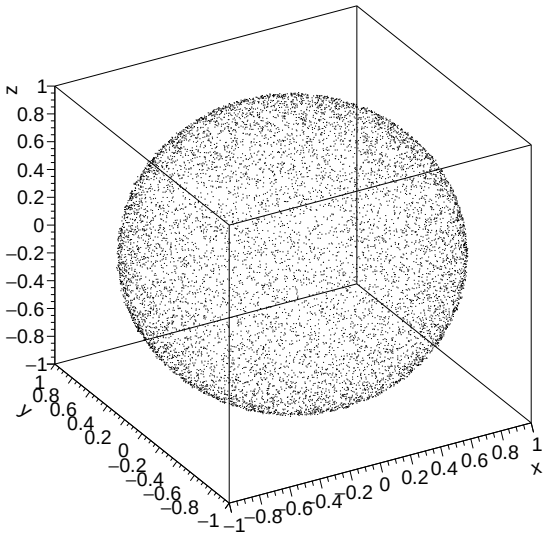

Figure 4.2: x, y and z components of randomly distributed three-dimensional unit vectors. θ and ϕ were generated according to equations 4.7 and 4.8.

6. In the CM frame, the final state particles are generated, considering the available phase space that is specified by the input parameters of the initial state. DCS distributions can also be considered.

7. The final state particles are boosted from the CM frame to the laboratory (LAB) frame, using the inverse of the previously utilized boost vector.

8. The four-momenta of the final state particles in the LAB frame can then be taken as input for the Geant4 simulation and their interaction with the detectors accurately modeled.

Fermi Momentum Correction for Real Data

The aforementioned method provides an accurate description of incoherent reactions off the deuteron in simulation. Furthermore, it is required to transform the real data that was measured off the static proton to let them match the real data that was measured off the moving proton inside the deuteron. The methodology is similar to the one utilized in simulation:

1. The four-momenta of the incoming photon and the static target are known, meaning the initial state four-momentum is known. This original four-vector will later function as a boost vector and shall be denoted as 'boost vector A'.

2. The four-momentum of the final state K^+ is already measured. It is Lorentz-transformed from the LAB frame into the CM frame using boost vector A.

3. Still in the LAB frame, a three-dimensional Fermi momentum vector is generated analogous to the previous methodology and used as the momentum component of a four-momentum of an artificial

initial state, while $\sqrt{m^2 + \vec{p}_F^2}$ is used as an artificial energy component. This artificial four-momentum shall be defined as 'boost vector B'.

4. The four-momentum of the K^+ in the CM frame is boosted back to the LAB frame, but this time not using the inverse of the original boost vector A, but instead of the artificial boost vector B.

5. The result is a four-momentum of a K^+ as if it had been created under the influence of a Fermi momentum.

Specific Fermi-momentum-related Complications

The previous section generally described how the data that were measured off the static proton target were corrected to match the ones measured off a moving target. This section shall go into more detail, list the specific complications that arise when comparing static to moving targets and how the aforementioned correction is able to address those. Major limiting factors are that the experimental setup does not contain an active target, so the recoil momentum of the spectator particle and thus the Fermi momentum can not be measured directly. Also, the neutron from the Σ^- decay goes undetected, meaning the final state is not fully specified. Following Fermi-momentum-related effects have to be considered:

1. The presence of the Fermi momentum leads to the four-momentum of the intial state to not be clearly defined, which introduces several further complications:
   a) The CM energy W is not clearly defined.
   b) The MM resolution is worsened.
   c) The W flux is not clearly defined.
   d) Apparent sub-threshold production is visible.
2. The bound proton and neutron are not on mass shell.
3. The Fermi momentum slightly changes the measured LAB angles.

These various effects and the necessary corrections shall be explained in the subsequent paragraphs.

1. Undefined initial state: Variables that relate to a static target will be denoted with the subscript 'S' and variables that relate to a moving target that contains a Fermi momentum $\vec{p}_F$ will be denoted with the subscript 'F', whereas the mass m always describes the target particle, not the spectator particle. For a static target, the initial state four-momentum is:

$$p_{\text{initial}_S} = p_\gamma + p_S = \begin{pmatrix} E_\gamma \\ 0 \\ 0 \\ E_\gamma \end{pmatrix} + \begin{pmatrix} m \\ 0 \\ 0 \\ 0 \end{pmatrix} .$$

Contrary, for a moving target, the initial state four-momentum is defined as follows:

$$p_{\text{initial}_\text{F}} = p_\gamma + p_\text{F} = \begin{pmatrix} E_\gamma \\ 0 \\ 0 \\ E_\gamma \end{pmatrix} + \begin{pmatrix} \sqrt{m^2 + \vec{p}_\text{F}^{\,2}} \\ p_{\text{F}_x} \\ p_{\text{F}_y} \\ p_{\text{F}_z} \end{pmatrix} .$$

As $\vec{p}_\text{F}$ is not known, the initial state four-momentum of a moving target is not clearly defined. This causes further complications.

1. a) Undefined W: The difference between the four-momenta of the initial states of static and moving targets implies that also the corresponding W differ. For the static target, W can be calculated as follows:

$$W_\text{S}(E_\gamma) = \sqrt{m^2 + 2E_\gamma m} .$$

For the moving target, one has to consider the Fermi momentum:

$$W_\text{F}(E_\gamma, \vec{p}_\text{F}) = \sqrt{m^2 + 2E_\gamma (\sqrt{m^2 + \vec{p}_\text{F}^{\,2}} - p_{\text{F}_z})} . \tag{4.9}$$

Let A be the domain of all accessible beam energies E_γ and B the codomain of all accessible CM energies W. In case of a static target, the function $W_\text{S} : A \to B$ is bijective and thus invertible, meaning once E_γ is known, then W is known, and vice versa. However, in case of a moving target, the function $W_\text{F} : A \to B$ is non-injective, meaning elements in B can potentially be mapped multiple times depending on the combination of the beam energy and the Fermi momentum. Equation 4.9 shows that W_F depends on the orientation of p_{F_z}: If p_{F_z} is oriented against the beam direction, W_F increases, if it is oriented in beam direction, W_F decreases. As $\vec{p}_\text{F}$ can not be measured, this leads to a loss or 'smearing' of W resolution.
Figure 4.3 shows a case study which illustrates this effect: Figure 4.3(a) shows a theoretical count for a single bin of $E\gamma$. Figure 4.3(b) shows the same count, but this time converted to W for a static target in blue and for a moving target in red. The bin edges of the E_γ spectrum have been translated to the bin edges of the W spectrum under the assumption of a static target. For the moving target, the E_γ distribution is convoluted with the Fermi momentum distribution, smearing out the W distribution symmetrically. For a single bin, this effect, with an order of about 80%, is quite dramatic.
However, for several adjacent bins of similar magnitude, the effect is reduced to a few percent, depending on the number of bins of similar magnitude. This is presented in figure 4.4: Analogous to the previous case, figure 4.4(a) exhibits a theoretical count depending on E_γ, this time for eleven adjacent bins with the same magnitude. Figure 4.4(b) shows the same spectrum converted to W for a static target in blue and the sum of all individual smeared signals of a moving target in red. Additionally, for the bins in light grey, the individual smeared W distributions can be seen in cyan, magenta and green, respectively. For the central bin, the difference between the W signal of the static and the moving target is diminished to approximately 5%, as the loss in count for this single bin as a result of Fermi smearing is compensated by the smeared counts of the neighbouring bins, partially filling up the central one. It would be reduced even further if more adjacent bins were generated. For the outermost bins, the difference is about 40%, as there are less neighbouring bins to compensate the smeared out count. This effect is especially important at production thresholds.
A priori, the Fermi smearing is able to hinder the detection of structures whose DCS is not significantly larger as the DCS of the W side band regions. This is illustrated in figure 4.5, which shows the same scenario

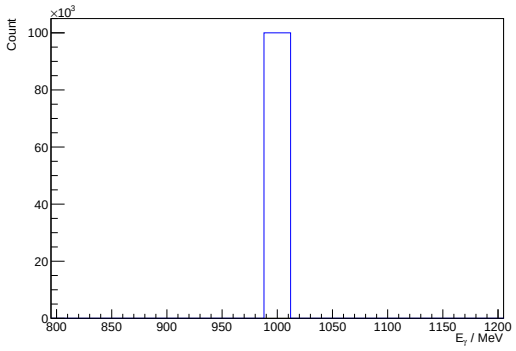

(a) Count depending on E_γ

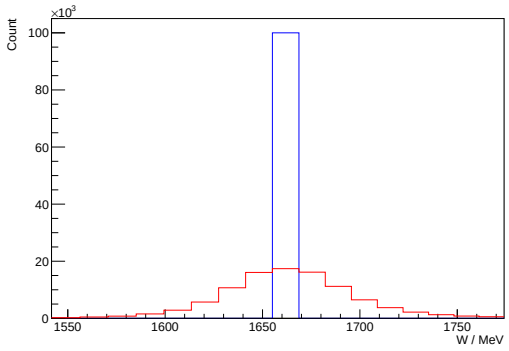

(b) Count converted to W

Figure 4.3: Case study of a theoretical event count (a) depending on E_γ and (b) converted to W for a static target (blue) and a moving target (red).

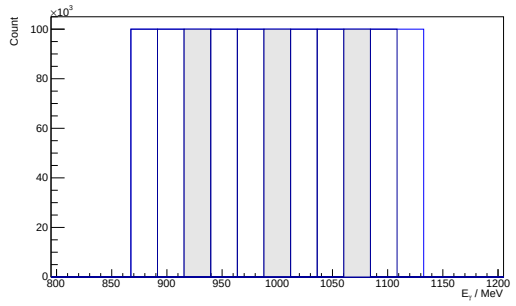

(a) Count depending on E_γ

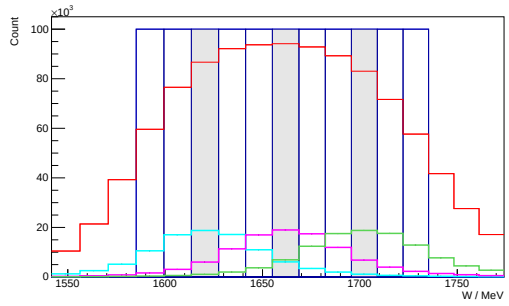

(b) Count converted to W

Figure 4.4: Case study of a theoretical event count for eleven bins of equal magnitude (a) depending on E_γ and (b) converted to W for a static target (blue) and a moving target (red). Cyan, magenta and green lines show individual smeared distributions of the grey bins, respectively.

as figure 4.4 with the only difference that one E_γ bin contains an increased count. The increased count is not high enough to compensate the loss of count due to Fermi smearing to an extent that would make it identifiable in the W spectrum of the moving target. A posteriori, the smearing can be undone though: In the special case where pure signal without any background contribution is measured and the underlying reaction can accurately be described in simulation including the Fermi smearing, the reconstruction efficiency as a function of W is known. By dividing the measured smeared count by the reconstruction efficiency, the original count is restored, even under the influence of Fermi momentum.
In this analysis, the measurement on the deuteron target does not only yield signal, but also background. The error ΔW that is made for background contributions can not be corrected a posteriori in the aforementioned way. This is not a problem though, as long as the same error is made for the measurements on the static proton target, achieving a match between the two datasets, and then subtracting the background contribution. The question arises: In order to achieve a match between the background contribution stemming from the moving proton and the background contribution stemming from the static proton, which W shall be assigned on an event-by-event basis? For a measurement on a moving target, assigning a W that corresponds to a static

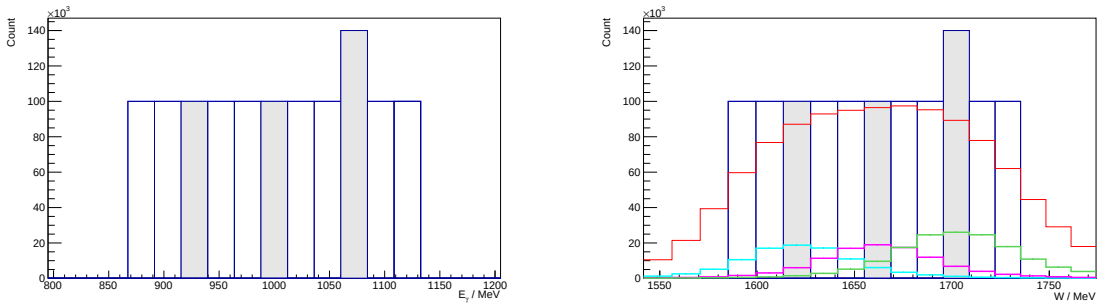

(a) Count depending on E_γ

(b) Count converted to W

Figure 4.5: Case study of a theoretical event count for ten bins of equal magnitude and one bin of larger magnitude (a) depending on E_γ and (b) converted to W for a static target (blue) and a moving target (red). Cyan, magenta and green lines show individual smeared distributions of the grey bins, respectively.

target introduces following error for W:

$$\Delta W_\mathrm{F} = W_\mathrm{F}^\mathrm{true} - W_\mathrm{S}^\mathrm{assigned} .$$

On the other hand, the aforementioned Fermi momentum correction is applied to the measurements on the static proton target, which treats the static proton data under the assumption that the target was moving, leading to the error:

$$\Delta W_\mathrm{S} = W_\mathrm{S}^\mathrm{true} - W_\mathrm{F}^\mathrm{assigned} = \Delta W_\mathrm{F} .$$

As the Fermi smearing of a W bin is symmetrical, meaning the same amount of counts is smeared towards lower energies as towards higher energies, it is the case that $\Delta W_\mathrm{F} = \Delta W_\mathrm{S}$, achieving a match between the moving proton dataset and the static proton dataset, allowing for a subtraction of the background contribution.

1. b) Worsened MM resolution: As the neutron from the Σ^- decay is not measured, the Σ^- can not be reconstructed directly. Its mass is visible as the MM to the K^+. In order to determine the MM to the K^+, the four-momentum of the K^+ needs to be subtracted from the four-momentum of the initial state. As, in case of the moving target, the initial state four-momentum is smeared by the Fermi momentum, the resulting MM spectrum is smeared accordingly. For the static target, the aforementioned Fermi momentum correction artificially smears the initial state and thus the MM spectrum, too, achieving a good description of the MM peak that is associated with the Λ, as shown later in section 4.2.2.4 in figure 4.19.

1. c) Undefined W flux: The photon flux N_γ is usually presented as a function of E_γ, which is possible as long as $W(E_\gamma)$ is bijective, which is not the case for a moving target. Therefore, N_γ must be determined as a function of W.
Figure 4.6 shows a case study of the dependency between E_γ flux and W flux. Figure 4.6(a) shows a theoretical flux depending on E_γ following a $\frac{1}{E_\gamma}$ distribution. $3 \cdot 10^8$ events have been generated, the binning has been chosen to be small with just 1 MeV per bin. Figure 4.6(b) shows the same spectrum, but this time converted to a flux depending on W for a static target in blue and a moving target in red. Due to the smearing effect described in section 1. a), discrepancies between the static and the moving target can only be seen for

$W < 1\,400\,\text{MeV}$ and $W > 2\,200\,\text{MeV}$. For W bins in-between, the loss of count due to Fermi smearing is compensated as the Fermi smearing of the neighbouring bins are filling them up. In the W region above the production threshold, which is at $W = 1\,691.126\,\text{MeV}$, the discrepancy is below 0.1% and thus negligible. The same situation is illustrated in figure 4.6(c) and 4.6(d), this time with the original tagger binning for E_γ and this binning converted to a W binning under the assumption of a static target, respectively. The same effects as for the fine binning are visible. Due to bin migration, the discrepancy between the W for a static and a moving target above production threshold is approximately 1%, which will be included in the estimation of the systematic uncertainties. Therefore, for the calculation of the DCSs of both beamtimes, the W flux under the assumption of a static target can be used.

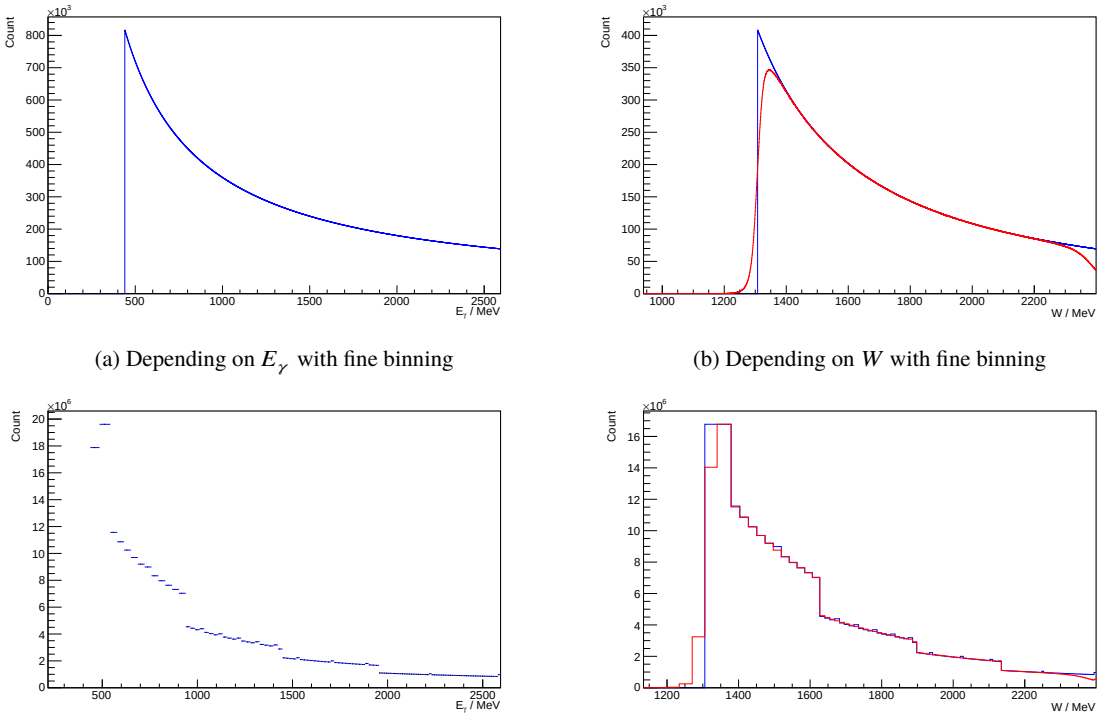

(a) Depending on E_γ with fine binning

(b) Depending on W with fine binning

(c) Depending on E_γ with original binning

(d) Depending on W with original binning

Figure 4.6: Case study of a theoretical flux (a) depending on E_γ with a fine binning, (b) depending on W with a fine binning, (c) depending on E_γ with the original tagger binning and (d) depending on W with the original tagger binning. The W binning was calculated from the E_γ binning under the assumption of a static target. In figure (b) and (d), the blue lines describe a static and the red lines a moving target.

1. d) Apparent sub-threshold production: Often, the DCS is presented as a function of E_γ, which is possible for a static target due to $W(E_\gamma)$ being a bijective function. For a moving target, it should be presented as a function of W though: Consider a theoretical scenario in which the DCS of an arbitrary reaction is accurately measured, has a flat energy dependence and a production threshold of $W = 1\,661.900\,\text{MeV}$ and the detector resolutions are neglected. For a static target as well as a moving target, the DCS as a function of W would look like a perfect step function like it is illustrated in figure 4.7(b). For a static target, the DCS as a function of E_γ would look like a step function, too, which rises at $E_\gamma = 1\,000\,\text{MeV}$ and is shown in

figure 4.7(a). For a moving target however, the DCS as a function of E_γ would even rise below the apparent production threshold $E_\gamma = 1\,000\,\text{MeV}$ which would be expected for a static target, as the Fermi momentum can be oriented towards the beam direction, increasing W even for lower beam energies. Note that this apparent 'sub-threshold production' would even be present in the final DCS after all of the aforementioned Fermi momentum corrections had been applied, including the division by the reconstruction efficiency, as it is the result of an actual measurement at an actual value for E_γ.
The only caveat that must be considered is that a DCS of a moving target that is presented as a function of E_γ should never be translated into a DCS that is presented as function of W under the assumption of a static target, as the apparent sub-threshold production in the E_γ spectrum would be converted into an erroneous sub-threshold production in the W spectrum. To avoid this error in the first place, the DCS will be presented as a function of W, not E_γ.

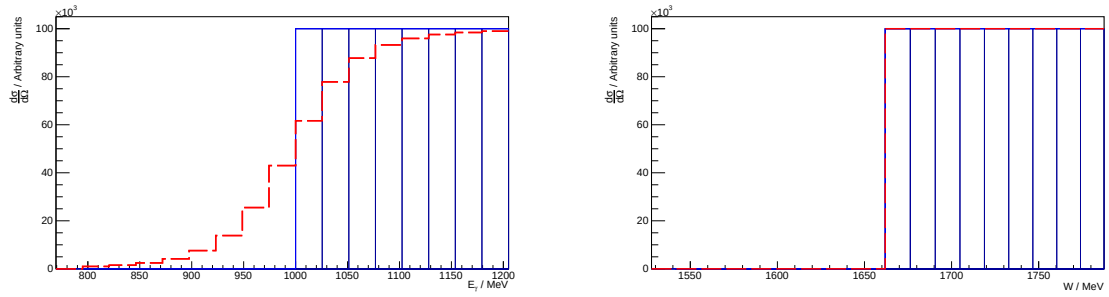

(a) Depending on E_γ

(b) Depending on W

Figure 4.7: Case study of a DCS of an arbitrary reaction as a function of (a) E_γ and (b) W. Blue lines describe a static target, red lines a moving target. Higher-laying bins have been used to generate these histograms, but are not shown.

2. Mass shell: The binding energy of the deuteron is $E_{\text{bind}} = 2.22\,\text{MeV}$ [78], which amounts to 1.11 MeV per nucleon. This implies that the bound proton, the bound neutron or both do not lie on mass shell. The question arises: Which effective mass value should be used for the description of the proton and neutron, respectively? For the proton and neutron, calculating the respective W for both the nominal nucleon mass and a nucleon mass reduced by the average 1.11 MeV shows that the deviation between these two values is below 0.1% and can be considered negligible. Thus, in all calculations for W, the nominal mass of the neutron is used. For the W assignment of the background reactions off the bound proton, this introduces a tiny W error, which is compensated by the fact that the same error is made for the measurements on the free proton target.

3. Changed angles: For a moving target, a small fraction of K^+ do not enter the FS compared to the static target. This effect can also be introduced to the data of the static target by applying the two previously described Lorentz transformations and sorting the data points into angular bins afterwards.

After applying the Fermi momentum correction to the dataset of hydrogen beamtime 2018-11, it can be subject to the same selection criteria that are applied to the dataset of deuterium beamtime 2018-06. The extraction of the yield N_{K^+Y} together with the associated selection criteria shall be described in the subsequent section.

4.2.2 Extraction of the Yield N_{K^+Y}

This section describes the applied selection criteria and methods that are utilized to extract the yield N_{K^+Y} for both individual beamtimes. The selection criteria are applied in successive order, each criterium improving the SNR. The very first step is selecting events which contain tracks with the right combination of charges.

4.2.2.1 Charge Signature Selection

First, a general overview of the kinematics of the reaction $\gamma n \to K^+\Sigma^-$ shall be provided. Due to its weak decay, the K^+ has a relatively long lifetime of $\tau = 12.38\,\text{ns}$ [27] and thus can be detected in the FS before it decays in the majority of cases. The angular distribution of the K^+ in the LAB frame is illustrated in figure 4.8 for CM energies ranging from threshold, being $W = 1\,691.126\,\text{MeV}$, up to $W = (1\,942.350 \pm 8.760)\,\text{MeV}$, which is the whole W range that has been considered in this analysis. The energy value after the plus-minus sign describes half of the W bin width. The distribution has been normalized so that its integral is equal to one. The figure only depicts the phase space distribution, meaning no DCS effects are included:

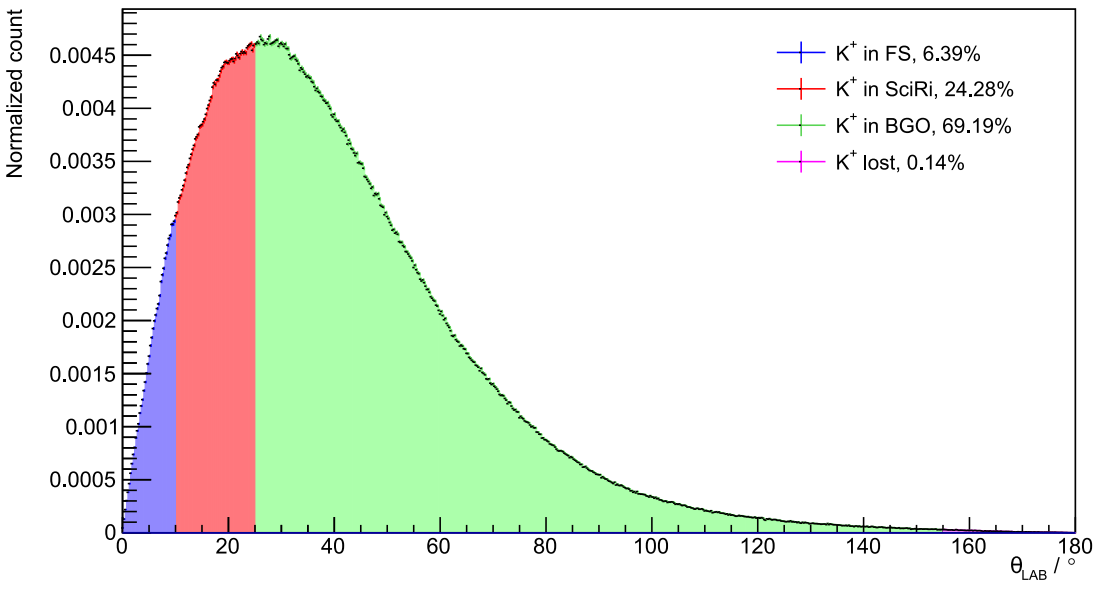

Figure 4.8: θ_{LAB} distribution of the K^+. $\theta_{\text{LAB}} = 0°$ corresponds to the forward direction. Only phase space is considered, no DCS contributions.

The angle $\theta_{\text{LAB}} = 0°$ corresponds to the forward direction. It is apparent that the K^+ enters the FS in 6.39%, SciRi in 24.28%, BGO in 69.19% and is out of acceptance in 0.14% of all cases. For completeness, it shall be mentioned that the K^+ can not be reliably reconstructed in SciRi, as it only functions as a veto detector without any provision of energy or momentum information. Contrary, a K^+ reconstruction in the BGO is possible by exploiting the fact that it deposits most of its energy in a single BGO crystal and then decays weakly, leading to a secondary energy deposit, whereas the time difference between the two clusters follows the distinct lifetime of the K^+ [82][83]. For extreme forward angles, only the detection in the FS is relevant. For the charge signature selection, events that have exactly one positively charged track in the FS are accep-

ted, corresponding to a potential K^+ candidate.

The Σ^- decays to $n\pi^-$ with a branching ratio of 99.84%. As it has a relatively short lifetime of $\tau = 0.15\,\text{ns}$ [27], it is only possible to detect its decay products. The focus will be on this dominant decay to $n\pi^-$ and, analogous to the previous investigation of the K^+, the corresponding angular distribution shall be explored. Assuming that the K^+ is detected in the FS, the phase space distribution of θ_{LAB} of the π^- looks as follows:

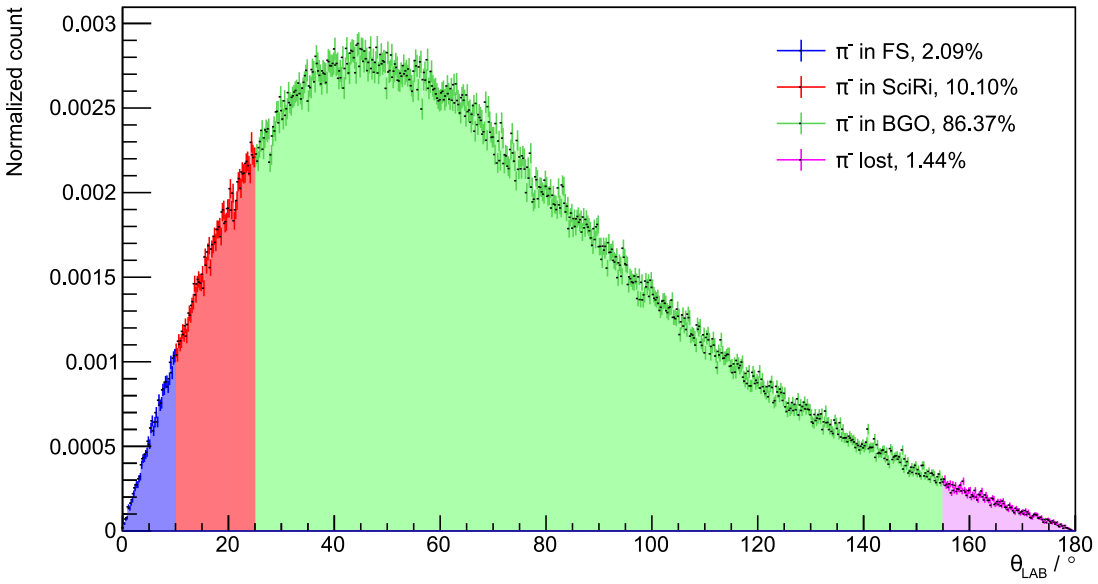

Figure 4.9: θ_{LAB} distribution of the π^-, assuming that the K^+ entered the FS. $\theta_{\text{LAB}} = 0°$ corresponds to the forward direction. Only phase space is considered, no DCS contributions.

In 86.37% of cases, the π^- enters the BGO. Due to this large fraction of the phase space, the π^- shall be reconstructed in the BGO. An identification in the FS has been tried but proved unsuccessfull due to the limited statistics, while a detection in SciRi does not provide the required energy information. Theoretically, it would also be possible to not require any π^- detection at all. However, background channels involve Λ and Σ^0 whose decays also involve π^-. Applying selection cuts to the π^- energy and momenta specifically tailored to the $K^+\Sigma^-$ final state reduces these background contributions. As the barrel and the BGO can detect charge, but not the sign of the charge, a single charged track in the BGO in combination with the barrel is required as a potential π^- candidate.

Finally, the angular distribution of the neutron is shown in figure 4.10, where it is required that the K^+ enters the FS and the π^- enters the BGO. The biggest portion of neutrons, 45.05%, enter SciRi. Second to that, 44.16% enter the BGO, while the FS is hit in 10.77% and the neutrons get out of detector acceptance in 0.02% of all cases. Neutrons interact only strongly with the active detector material: For fast neutrons, this happens via scattering of protons, which cause a detectable path of ionization, obtaining a large cross section of approximately 0.1 b [84]. In simulation, a reliable modeling of the neutron detection efficiency in

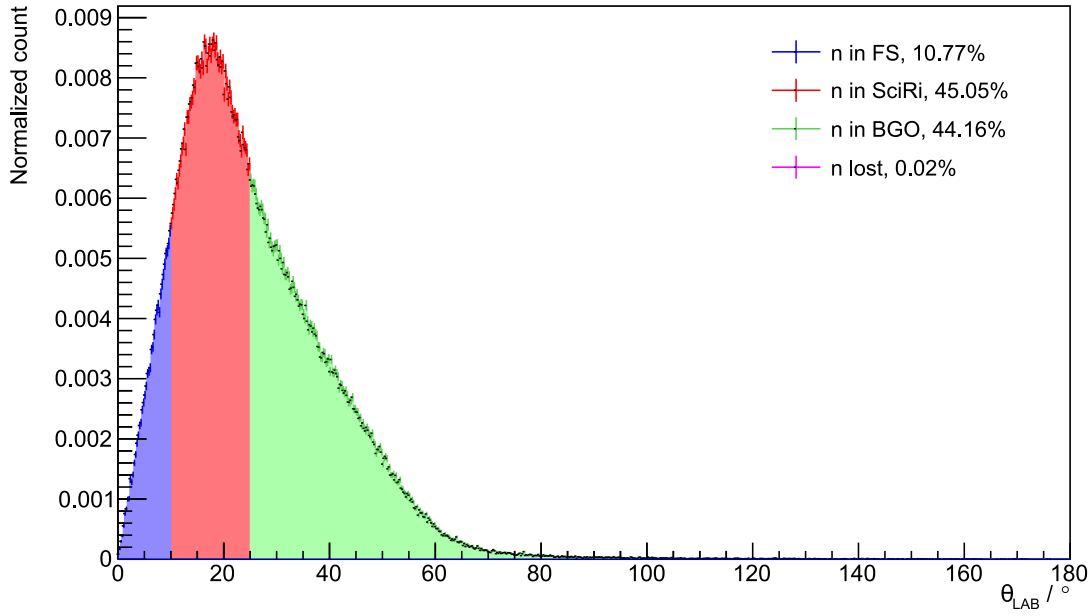

Figure 4.10: θ_{LAB} distribution of the neutron, assuming that the K^+ entered the FS and the π^- entered the BGO. $\theta_{\mathrm{LAB}} = 0°$ corresponds to the forward direction. Only phase space is considered, no DCS contributions.

either of the detectors or of the crystal multiplicity in the BGO is not possible, as the interaction of neutrons with matter is a very complex process. Not only does it depend on the kinetic energy of the neutron, it also depends on the properties of the scintillators such as the light output, the scintillating efficiency and the wavelength of maximum emission, and furthermore on the properties of the light guides, photomultipliers and discriminators. The applied cluster energy thresholds play an important role, too. The question arises which neutral particle count should be allowed for the charge signature selection. To answer this question, different approaches were assessed:

1. Neutral particle count ≤ 1: The first method would be to allow a neutral particle count of zero or one as a charge signature selection and to not place any further selection criteria on the neutron candidate. This would circumvent the issue of the unknown neutron detection efficiency and achieve a match between real and simulated data. However, this would also lead to the inclusion of photon background especially from K^* and Σ^0 decays, worsening the SNR. Therefore, this approach will not be chosen. For completeness, the effect of allowing a neutral particle count of zero or one has been compared to an analysis where only a neutral particle count of zero is allowed. The measured yield and therefore the resulting final DCS shows a difference in scale of 15.23%.

2. Neutral particle count $= 0$: Another method would be to choose a neutral particle count of exactly zero as a charge signature selection and discard any events that contain neutral tracks. This way, one removes background contributions from photons, but one must pay attention to the match between real and simulated data: In the Geant4 simulation, as the energy deposit of the neutron can not be modeled accurately,

the G4EmStandardPhysics [85] class is utilized, meaning only electromagnetic interactions are considered and the neutrons energy deposit is assumed to always be zero. In simulation, this always leads to a count of uncharged tracks of zero. In real data, the neutron will go undetected in most cases, leading to a count of uncharged tracks of zero, too, achieving a match between simulated and real data. If, however, in real data, the neutron energy deposit surpasses the necessary cluster energy threshold, a count of uncharged tracks of one will be encountered, inducing a mismatch between real data and simulation. The extent of this mismatch will be estimated and used as a systematic uncertainty to the DCS measurement.

In general, the neutron detection efficiency depends on the neutron kinetic energies and cluster energy thresholds. The involved neutron kinetic energies before the interaction of the neutron with the detector material can be described in simulation. For the BGO, the mean neutron kinetic energy shows almost no W dependency and is 105.9 MeV. The BGO detector used in the BGOOD experiment has previously been used by a predecessor experiment, the GRAAL experiment [86], which has measured the neutron detection efficiency using the reaction $\gamma p \to \pi^+ n$, where the π^+ identification was employed to tag the expected neutron, and compared it to simulation [87]. GRAAL has measured the neutron detection efficiency depending on the neutron kinetic energy and cluster energy threshold, which is presented in figure 4.11. For real data and a neutron kinetic energy of 105.9 MeV, the neutron detection efficiency for a 2 MeV cluster energy threshold is about 60% and for a 20 MeV cluster energy threshold it is approximately 30%.

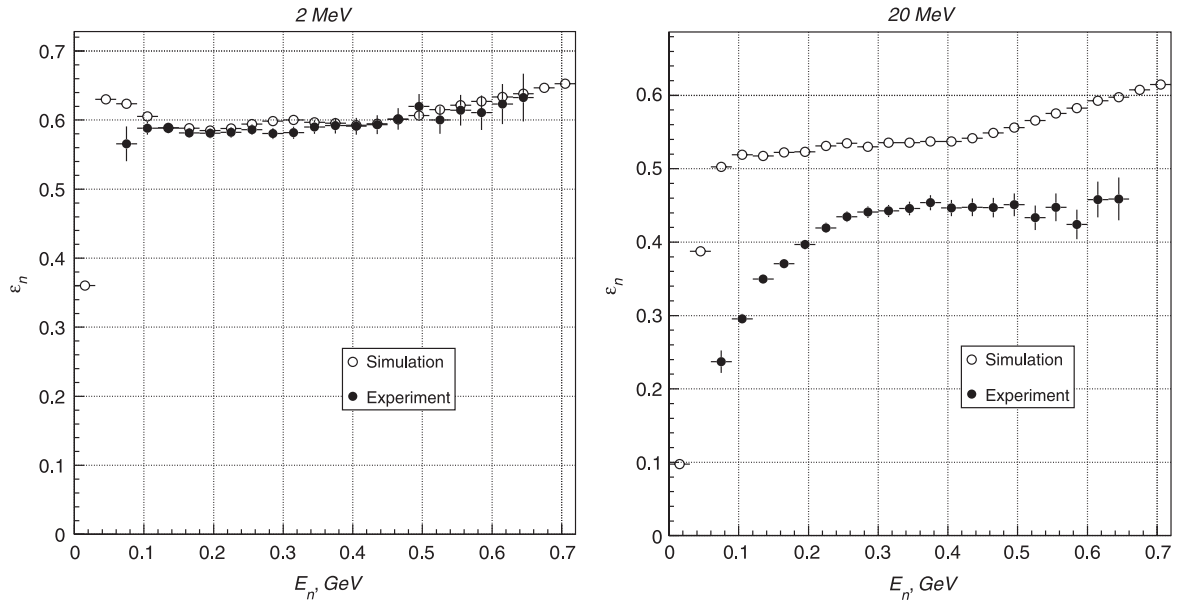

(a) 2 MeV cluster energy threshold

(b) 20 MeV cluster energy threshold

Figure 4.11: Neutron detection efficiency obtained from the GRAAL experiment (closed circles) and GEANT3 simulation using the FLUKA package (open circles) as a function of neutron kinetic energy for (a) 2 MeV and (b) 20 MeV cluster energy thresholds [87].

The measured neutron kinetic energy distribution in the BGO is roughly exponential. One can use these two data points to perform an exponential extrapolation of the neutron detection efficiency as a function of the applied cluster energy thresholds and evaluate it at the cluster energy threshold that is used at BGOOD, namely 25 MeV. This leads to an expected neutron detection efficiency of approximately 24.74%. Multiplication

with the angular phase space of the neutrons that enter the BGO, which has a value of 44.16% and is shown in figure 4.10, leads to an estimate of the fraction of neutrons which are expected to be observed in the BGO of 10.93% relative to the full neutron phase space. Even if a neutral particle count of zero or one is allowed, after all cuts have been applied to real data, there is not a single event in SciRi and not a single neutral event in the FS. This means that 89.07% of neutrons are expected to be undetected, which is the part of the phase space that is measured in this analysis when setting the amount of uncharged tracks to be zero. This implies a one-sided systematic uncertainty of $\frac{10.93\%}{89.07\%} = 12.27\%$ for the chosen charge signature selection, which will be included in the systematic uncertainties listed in chapter 5. For the future, an improved determination of the neutron detection efficiency could be achieved by replicating the entire GRAAL analysis [87] using the current hardware setup of BGOOD. For completeness, it shall be mentioned that a differentiation between neutrons and photons according to the BGO crystal multiplicities has been tried but proved to be unsuitable, because the multiplicity distributions of neutrons and photons show a large overlap and the multiplicity of the neutron is larger than 1 in most cases.

To summarize: The specific decay chain $\gamma n \rightarrow K^+\Sigma^- \rightarrow K^+\pi^- n$ will be identified. The charge signature selection of this reaction corresponds to one positive, one negative and zero neutral particles. Therefore, one requires exactly one positively charged track in the FS as a K^+ candidate, exactly one charged track in the BGO as a π^- candidate and one does not allow any further tracks, as the exact neutron detection efficiency is unknown and this requirement helps to suppress background. By doing so, one introduces a one-sided systematic uncertainty of 12.27%. At this point of the analysis, specific cuts can be applied to the individual tracks as described in the next sections.

4.2.2.2 π^- Energy and Momentum

After events with the appropriate charge signature selection have been identified, the two main challenges are differentiating between the K^+ and the π^+ peak in the ToF mass spectrum and between the Σ^- and the Λ peak in the MM spectrum to the K^+. Before any selection criteria or fits are applied to these spectra, it is reasonable to improve the SNR by applying selection criteria to other parameters, such as energy and momentum of the π^- stemming from the Σ^- decay. For better reproducibility, the selection criteria are presented in chronological order, meaning the SNR will improve with every subsequent criterion.

Maximum Allowed E_{kin} of π^- in BGO

In the previous section 4.2.2.1, it was shown that for the selection of the charge signature a π^- *candidate* in the BGO is required. The BGO in combination with the barrel is able to distinguish between charged and uncharged particles, but not between positively charged and negatively charged particles. This means that one can a priori not be sure whether π^- or π^+ were measured. Furthermore, due to the lack of a proper barrel calibration, a distinction between π and protons via a $\frac{\Delta E}{E}$ measurement is also not possible. For a first-order distinction of the different particle types, it must therefore be relied on the different energy deposits in the BGO. More specifically, the kinetic energy deposit E_{kin} shall be limited to be below the maximum value that is expected for π^-. The energy deposit dE per penetration depth dx of charged particles traversing through matter, also known as 'linear stopping power', is described by the Bethe-Bloch equation, shown here in SI units:

$$-\frac{dE}{dx} = \rho K z^2 \frac{Z}{A}\frac{1}{\beta^2}\left(\frac{1}{2}\ln\left(\frac{2m_e c^2\beta^2\gamma^2 W_{\max}}{I^2}\right) - \beta^2 - \frac{\delta(\gamma\beta)}{2}\right) . \tag{4.10}$$

ρ is the density of the absorber, $K = 4\pi N_A r_e^2 m_e c^2$ a constant, z the charge number of the incident particle, $\frac{Z}{A}$ the atomic mass over atomic number of the absorber, $W_{\max}$ the maximum possible energy transfer to an electron in a single collision and δ a density effect coefficient. This version of the Bethe-Bloch equation is valid in the region $0.1 \lesssim \beta\gamma \lesssim 1000$ [27]. For $\beta\gamma < 0.1$, equation 4.10 has to be adjusted by introducing low-energy correction terms such as a shell correction term, Bloch correction term and Barkas correction term. The Barkas correction term is especially important for differentiating between π^- and π^+: In theory, one could imagine that an atom's electron cloud is marginally recoiling against the approach of a negative projectile and being marginally attracted towards an approaching positive projectile. The stopping power should therefore be slightly smaller for negative particles than for positive particles [27]. As these low-energy correction terms are not fully included in the Geant4 simulation of the experiment, it must be ensured that their extent is negligible in order to achieve an accurate match between simulation and real data. An investigation of the kinematics of the reaction $\gamma n \to K^+\Sigma^-$ revealed that the involved π^- inherits $0.58 \lesssim \beta\gamma \lesssim 2.53$, which is above the aforementioned lower limit $\beta\gamma \sim 0.1$. Equation 4.10 is therefore a sufficient description of the energy deposit of π^- in the BGO and can be used in the simulation.

Using the simulation, a first-order differentiation between π^- and other particles can be achieved by placing a cut on the maximum kinetic energy deposit in the BGO which is expected for π^- stemming from the original reaction $\gamma n \to K^+\Sigma^- \to K^+ n\pi^-$. As K^+ and protons tend to deposit more energy than π, a reduction of background can be achieved. Figure 4.12 shows the kinetic energy deposit E_{kin} of particles in the BGO for real data of both beamtimes and for simulated π^- stemming from the Σ^- decay.

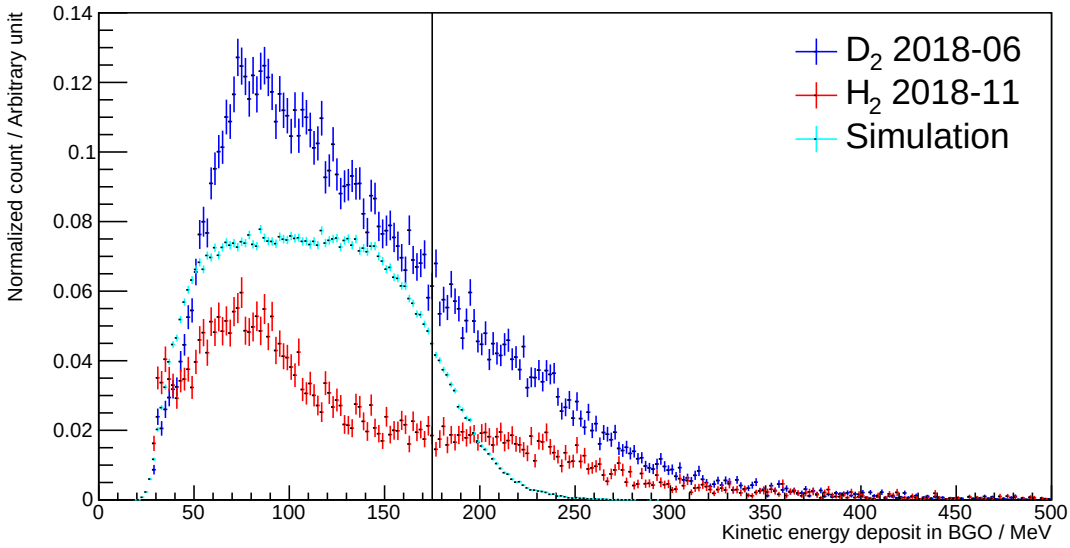

Figure 4.12: Kinetic energy deposit E_{kin} of particles in the BGO for deuterium beamtime 2018-06, hydrogen beamtime 2018-11 and Geant4 simulation of π^- from the original reaction $\gamma n \to K^+\Sigma^- \to K^+ n\pi^-$. The counts of the real data are normalized, the scale of the simulated data is chosen arbitrarily. The vertical line describes the cut at 90% of the full integral of the simulated spectrum, which is chosen according to the cumulative distribution shown in figure 4.13. The applied visualization cuts can be seen in figure 4.14.

The figure is a projection over all centre-of-mass W bins that are considered in this analysis, namely from $W = (1\,688.855 \pm 6.745)\,\mathrm{MeV}$ to $W = (1\,942.350 \pm 8.760)\,\mathrm{MeV}$, where the values after the plus-minus sign correspond to half of the W bin width. This is also the case for all subsequent histograms for which no explicit W dependency is presented. For the real data a normalized count is shown, meaning a count that was divided by the respective flux, reconstruction efficiency and effective target area density, whereas for the simulated data an arbitrary scale is applied. The normalized count of the deuterium data is much higher than for the hydrogen data. This can be explained by the fact that both datasets contain contributions of background reactions off the proton, but the deuterium dataset also contains contributions of background reactions off the neutron, which are mostly π^+ in the FS, and also signal reactions. The shape of the rising edge is similar, whereas for the hydrogen data the shape flattens at around $E_{\mathrm{kin}} = 120\,\mathrm{MeV}$. Adding the simulated π^- contribution to the hydrogen dataset roughly adds up to the shape of the deuterium dataset. The simulated energy spectrum drops at $E_{\mathrm{kin}} = 150\,\mathrm{MeV}$, which makes sense given that this is where the π^- reaches an energy of roughly $2m_{\pi^-}$, which is around the kinematic range of a minimum ionizing particle.

As the shape of the kinetic energy distribution is not Gaussian, it must be quantified by other means. The kinetic energy distribution of the simulation is converted to a cumulative plot as shown in figure 4.13 and the point at which the cumulative energy distribution surpasses 90% of its total integral is used as a cut criterion. These histograms are created for each bin of W and the W dependency is then descibed by a second-degree polynomial fit, enabling a W-dependent cut on the kinetic energy deposit. This is depicted in appendix C in detail. For a projection over all utilized W bins, the cut is positioned at $E_{\mathrm{kin}} = 175\,\mathrm{MeV}$. This leads to a 10% decrease of signal, but also to an approximate 30% decrease of noise. As more selection criteria are applied, the match between the real deuterium data and the simulated data will improve.

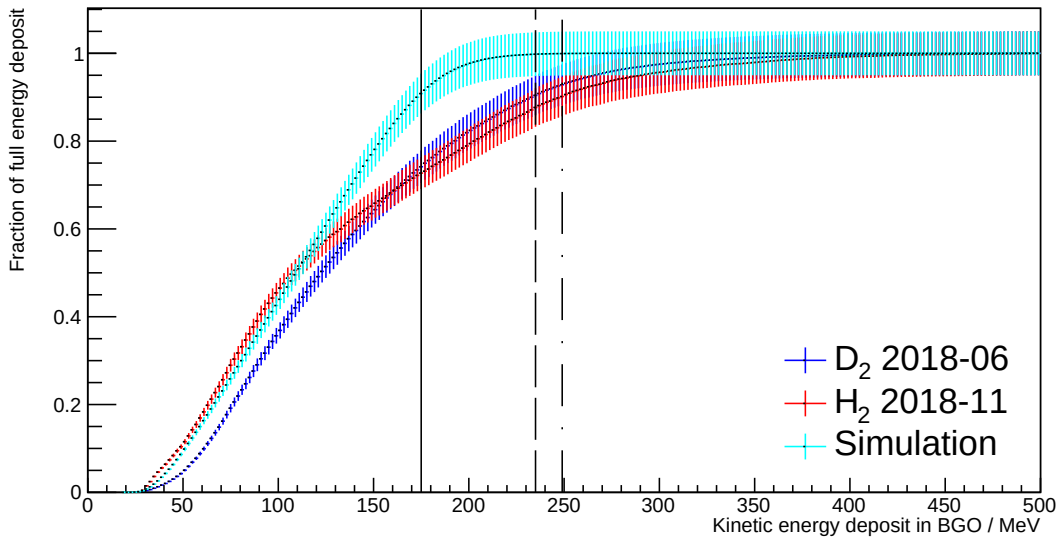

Figure 4.13: Cumulative distribution of figure 4.12 The vertical lines represent the kinetic energy deposits at which the cumulative distributions surpass 90% of their full integral. The solid line describes the simulation and corresponds to the cut that is actually applied in the analysis, the dashed line describes the hydrogen data and the dashed-dotted line the deuterium data. The W dependency of these values is shown in appendix C in detail, the visualization cuts in figure 4.14.

In order to achieve an adequate comparison of both real datasets to the simulated data, the real data should not inhibit any avoidable background, for example from the π^+ peak or proton peak in the ToF mass spectrum. Figures 4.12 and 4.13 were therefore created after placing a fixed 2σ cut on the K^+ ToF mass peak as well as on the expected MM to the K^+ peak corresponding to the Σ^- mass as shown in figure 4.14. These cuts are only used to compare real data and simulated data and have no influence on the actual final analysis. In the subsequent chapters they will be referred to as 'visualization cuts'. As apparent from figure 4.14(c), the simulation also considers cases where the K^+ decays to $\pi^+\pi^0$ before it reaches the FS, leading to a small fraction of observed π^+.

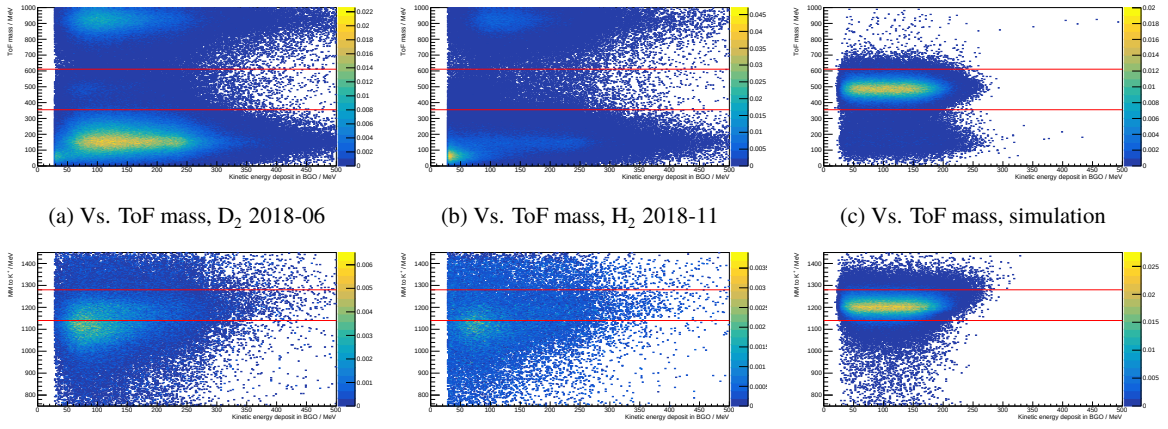

(a) Vs. ToF mass, D_2 2018-06 (b) Vs. ToF mass, H_2 2018-11 (c) Vs. ToF mass, simulation

(d) Vs. MM to K^+, D_2 2018-06 (e) Vs. MM to K^+, H_2 2018-11 (f) Vs. MM to K^+, simulation

Figure 4.14: Relation between kinetic energy deposit in the BGO E_{kin} and ToF mass, MM to K^+ and dataset, respectively. For visualization, figures 4.12 and 4.13 were created under a 2σ cut around the K^+ ToF mass and around the expected MM to K^+ as presented by the red lines, getting rid of background and enabling a fairer comparison of real data and simulation. This 'visualization cut' is not present in the actual final analysis.

Momentum of π^- in Σ^- Frame

The previous cuts were applied in the LAB frame. It is also possible to take the four-momentum of the π^- and perform a Lorentz transformation to the Σ^- frame, in which the π^- and neutron momenta are oriented back-to-back. The distribution of the π^- momentum in the Σ^- frame, $|\vec{p}_{\pi^-\text{in }\Sigma^-}|$, is investigated as shown in figure 4.15 over all used bins of W. Depicted are normalized counts for both beamtimes and an arbitrary scale for simulation. The shape of the deuterium dataset can nicely be described by combining the shape of the hydrogen dataset with the Gaussian peak that is expected from simulation. The difference in scale of the first peaks at around $|\vec{p}_{\pi^-\text{in }\Sigma^-}| = 120\,\text{MeV}$ is anticipated due to the additional background contribution stemming from reactions off the neutron inside the deuteron, part of them leading to π^+ in the FS that overlap with the K^+. This can be seen in figures 4.16(a) and 4.16(b). A Gaussan fit is applied to the simulated data for each bin of W. The corresponding Gaussian mean and sigma as functions of W can then be described by second-degree polynomials, which are shown in appendix C in detail. A 2σ cut is chosen. For the projection over all used bins of W illustrated in figure 4.15 , the Gaussian fit yields $\mu = (182.85 \pm 0.05)\,\text{MeV}$ and $\sigma = (24.49 \pm 0.04)\,\text{MeV}$, the 2σ range is described by the vertical lines. For a fair comparison of real and simulated data in figure 4.15, the same visualization cut as chosen for the

kinetic energy deposit in the BGO is chosen, illustrated in figure 4.16.

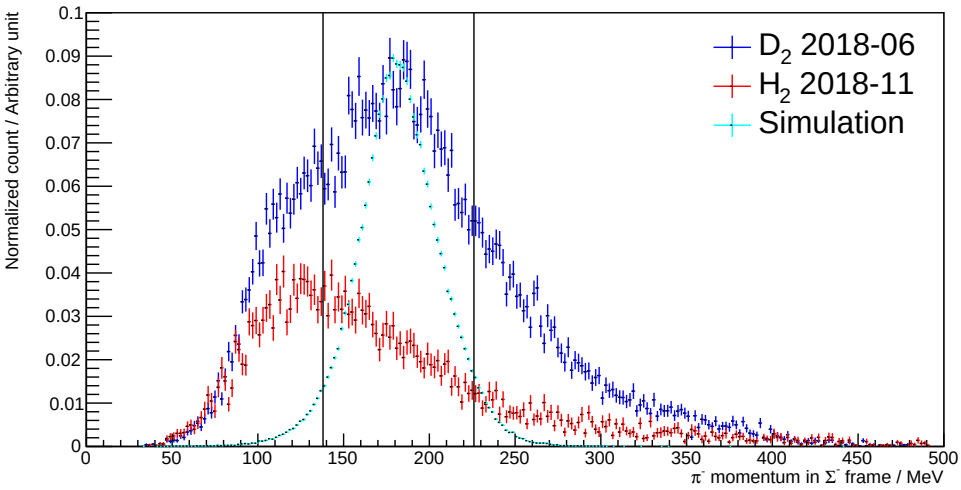

Figure 4.15: Momentum of the π^- in the Σ^- frame $|\vec{p}_{\pi^- \text{in } \Sigma^-}|$ for both beamtimes, shown as normalized counts, and simulation, shown with an arbitrary scale, over all used bins of W. A Gaussian fit to the simulated data yields $\mu = (182.85 \pm 0.05)$ MeV and $\sigma = (24.49 \pm 0.04)$ MeV, the 2σ range is described by the vertical lines. The W dependency is shown in appendix C, the visualization cuts in figure 4.16.

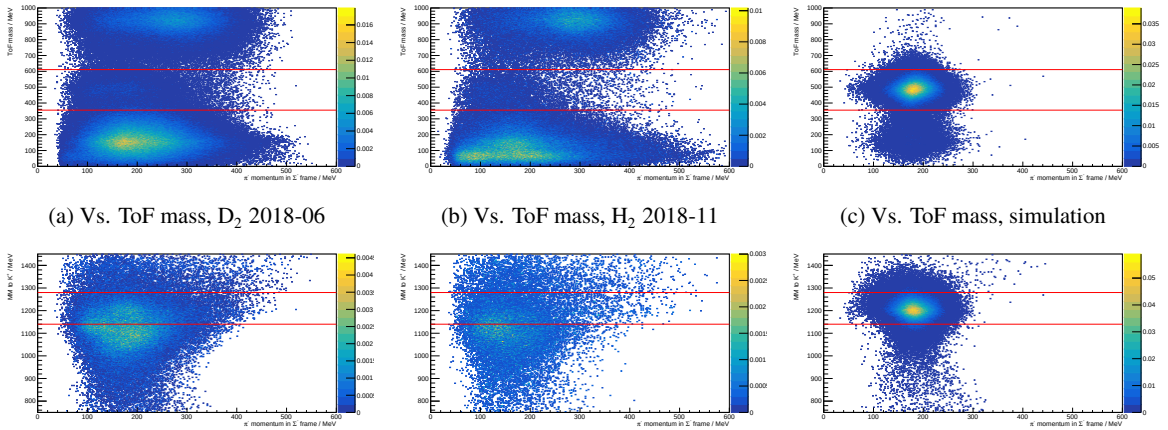

(a) Vs. ToF mass, D_2 2018-06 (b) Vs. ToF mass, H_2 2018-11 (c) Vs. ToF mass, simulation

(d) Vs. MM to K^+, D_2 2018-06 (e) Vs. MM to K^+, H_2 2018-11 (f) Vs. MM to K^+, simulation

Figure 4.16: Visualization cuts for the momentum of the π^- in the Σ^- frame as in figure 4.15. See caption of figure 4.14.

4.2.2.3 Missing Mass to $K^+\pi^-$

For the decay of an initial state with four-momentum p_{initial} to two particles with four-momenta p_1 and p_2, the MM to p_1 is defined as:

$$m_{\text{MM}} = (p_{\text{initial}} - p_1)^2 \,.$$

The four-momentum conservation between the initial state and the final state of the reaction $\gamma n \to K^+\Sigma^- \to K^+\pi^- n$ can be written as follows:

$$p_\gamma + p_{\text{Target}} = p_{K^+} + p_{\Sigma^-} = p_{K^+} + p_{\pi^-} + p_n \,,$$

$$\begin{pmatrix} E_\gamma \\ \vec{p}_\gamma \end{pmatrix} + \begin{pmatrix} E_{\text{Target}} \\ \vec{p}_{\text{Target}} \end{pmatrix} = \begin{pmatrix} E_{K^+} \\ \vec{p}_{K^+} \end{pmatrix} + \begin{pmatrix} E_{\Sigma^-} \\ \vec{p}_{\Sigma^-} \end{pmatrix} = \begin{pmatrix} E_{K^+} \\ \vec{p}_{K^+} \end{pmatrix} + \begin{pmatrix} E_{\pi^-} \\ \vec{p}_{\pi^-} \end{pmatrix} + \begin{pmatrix} E_n \\ \vec{p}_n \end{pmatrix} \,. \tag{4.11}$$

As outlined in section 4.2.2.1, an accurate modeling of the reconstruction efficiency of a neutron measurement in simulation is not possible. The neutron from the Σ^- decay will therefore be treated as a missing particle and the MM to $K^+\pi^-$, which is expected to be the neutron mass, will be measured instead. Isolating the four-momentum of the neutron and squaring it leads to an expression of the mass of the neutron:

$$m_n = \sqrt{((E_\gamma + E_{\text{Target}}) - (E_{K^+} + E_{\pi^-}))^2 - ((\vec{p}_\gamma + \vec{p}_{\text{Target}}) - (\vec{p}_{K^+} + \vec{p}_{\pi^-}))^2} \,.$$

The distribution of the MM to $K^+\pi^-$ can be seen in figure 4.17 for the visualization cuts presented in figure 4.18 as a projection over all used bins of W. The real data are shown as normalized counts, whereas the simulated data is shown with an arbitrary scale. For simulated data, the MM to $K^+\pi^-$ does not sit at the nominal mass of the neutron, but instead at a Gaussian mean of $\mu_n = (960.83 \pm 0.08)\,\text{MeV}$ with $\sigma_n = (36.51 \pm 0.05)\,\text{MeV}$. This is a result of the fact that the FS is calibrated matching the proton ToF mass to the proton nominal mass, not using any K^+, leading to a slight offset. This offset in simulation matches real data once a clean K^+ ToF mass selection is done. As apparent from figure 4.18, a wider ToF mass cut leads to more inclusion of π^+ background, which skews the MM to $K^+\pi^-$ to slightly lower values in real data, while a tighter ToF mass cut leads to a good match between real and simulated data. For each bin of W, a Gaussian fit is applied to the simulated data and the W dependency of the Gaussian mean and sigma can be described by a fourth-degree polynomial. This is all shown in appendix C. A 2σ cut is chosen. For the projection over all used W bins in figure 4.17, this is illustrated by the two vertical lines.

4.2.2.4 Missing Mass to K^+

Now that all cuts have been applied to the π^- and the missing neutron, one can focus on the MM to the K^+, which should ideally correspond to the Σ^- mass. It can be calculated by utilizing the four-momentum conservation from equation 4.11 again:

$$m_{\Sigma^-} = \sqrt{((E_\gamma + E_{\text{Target}}) - E_{K^+})^2 - ((\vec{p}_\gamma + \vec{p}_{\text{Target}}) - \vec{p}_{K^+})^2} \,.$$

Figure 4.19 depicts the MM spectrum to the K^+ for both beamtimes as normalized counts and simulated data with an arbitrary scale. As explained in section 4.1, the background reactions off the hydrogen target are expected to contain contributions from $K^+\Lambda$, $K^+\Sigma^0$ and $K^+\Sigma^0(1385)$, which can nicely be seen in the MM distribution: The Λ peak is much more dominant than the Σ^0 peak, while the $\Sigma^0(1385)$ peak, in practice, does not contribute. The Λ peak sits approximately 15 MeV higher than its nominal mass $m_\Lambda = 1\,116\,\text{MeV}$ [27],

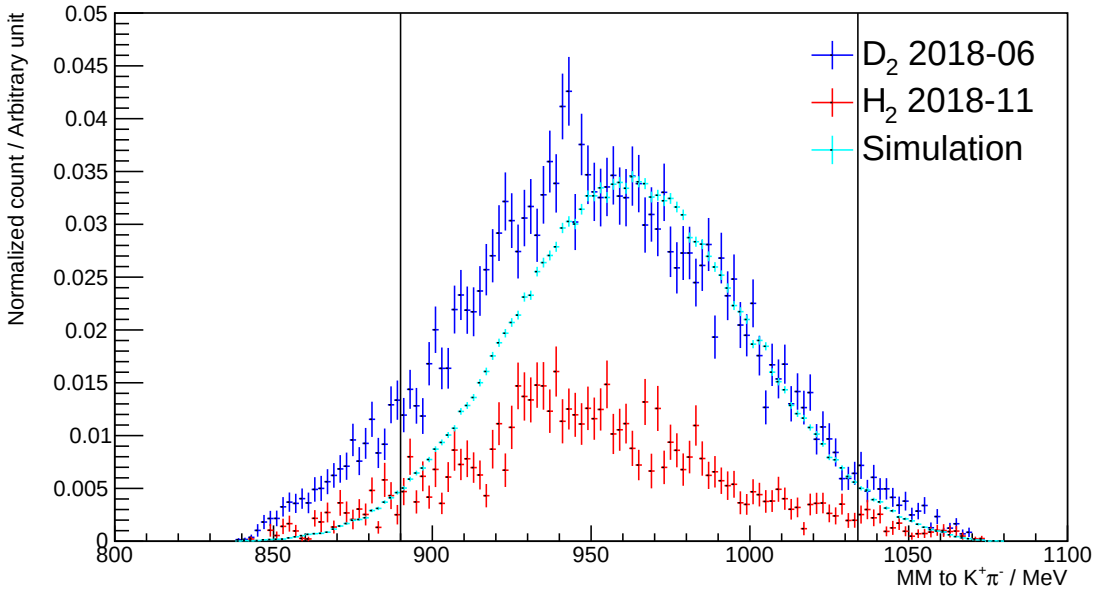

Figure 4.17: MM to $K^+\pi^-$ for both beamtimes, shown as normalized counts, and simulation, shown with an arbitrary scale, over all used bins of W. A Gaussian fit to the simulated data yields $\mu_n = (960.83 \pm 0.08)$ MeV and $\sigma_n = (36.51 \pm 0.05)$ MeV, the 2σ range is described by the vertical lines. The W dependency is shown in appendix C, the visualization cuts in figure 4.18.

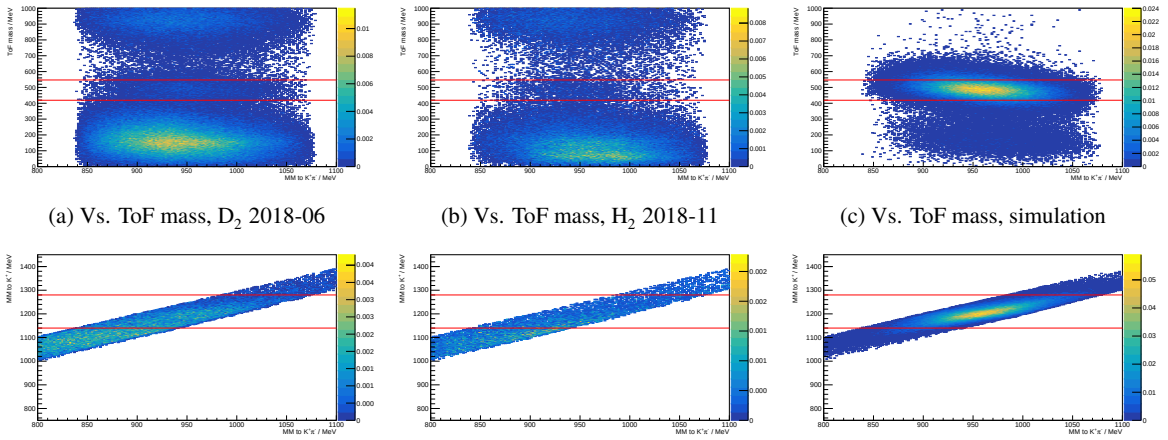

(a) Vs. ToF mass, D_2 2018-06 (b) Vs. ToF mass, H_2 2018-11 (c) Vs. ToF mass, simulation

(d) Vs. MM to K^+, D_2 2018-06 (e) Vs. MM to K^+, H_2 2018-11 (f) Vs. MM to K^+, simulation

Figure 4.18: Visualization cuts for the MM to $K^+\pi^-$ as in figure 4.17. See caption of figure 4.14. This time, the 2σ cut around the K^+ ToF mass has been exchanged for a 1σ cut.

which is consistent with the fact that the Σ^- peak in simulation also sits about 15 MeV higher than its nominal mass $m_{\Sigma^-} = 1\,197$ MeV [27], namely at a Gaussian mean of $\mu_{\Sigma^-} = (1\,209.10 \pm 0.06)$ MeV with $\sigma_{\Sigma^-} = (28.09 \pm 0.05)$ MeV. As mentioned before, it is an expected result of the calibration procedure of the FS. In theory, the data from the deuteron dataset would contain Σ^- signal, the same background reactions as in the hydrogen dataset and a contribution of $K^+\Sigma^-(1385)$, which, in practice, is nonexistent. The shape of the deuteron dataset can be described by combining the shape of the simulated signal with the background contributions off the proton. The fact that the scale of the Λ peak differs between the hydrogen and the deuteron dataset is caused by the K^+ selection still containing background. Figure 4.19 was created under the visualization cut shown in figure 4.20 where a 1σ K^+ ToF mass visualization cut is chosen. For a clean 0.5σ selection, the scale of the Λ peak would be the same for both real datasets. A Gaussian fit is applied to the simulated data for each bin of W and the W dependency of the Gaussian mean and sigma is described by a fourth-degree polynomial, shown in detail in appendix C. A 2σ cut is chosen, which, for the projection over all used W bins in figure 4.19, is described by the two vertical lines.

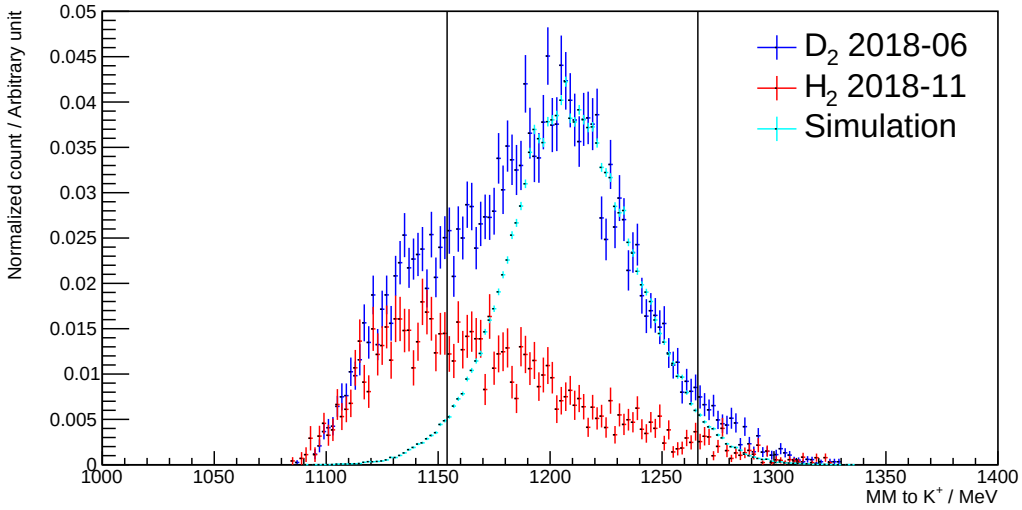

Figure 4.19: MM spectrum to the K^+ for both beamtimes as normalized counts and simulated data with an arbitrary scale as a projection over all used bins of W. A Gaussian fit to the simulated data yields $\mu_{\Sigma^-} = (1\,209.10 \pm 0.06)$ MeV and $\sigma_{\Sigma^-} = (28.09 \pm 0.05)$ MeV, the 2σ range is described by the vertical lines. The W dependency is shown in appendix C, the visualization cuts in figure 4.20.

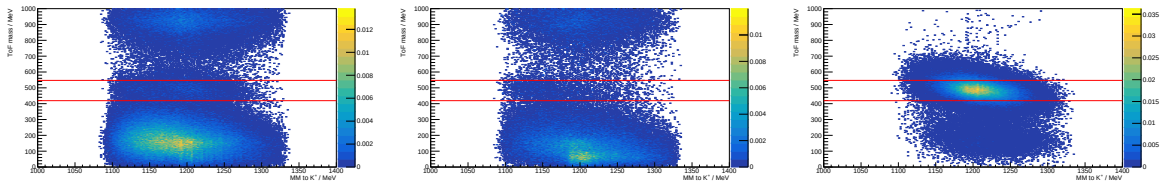

(a) Vs. ToF mass, D_2 2018-06 (b) Vs. ToF mass, H_2 2018-11 (c) Vs. ToF mass, simulation

Figure 4.20: Visualization cuts for the MM to K^+ as in figure 4.19. See caption of figure 4.14. This time, the 2σ cut around the K^+ ToF mass has been exchanged for a 1σ cut.

4.2.2.5 Maximum Likelihood Fit to the ToF Mass Spectrum

Finally, the yield N_{K^+Y} can be extracted from the ToF mass spectra. Figure 4.21 shows the ToF mass spectra as projections over all used W bins for both beamtimes as normalized counts, meaning as counts scaled by the inverse of their corresponding flux, reconstruction efficiency and effective target area density, while the simulated data exhibits an arbitrary scale.

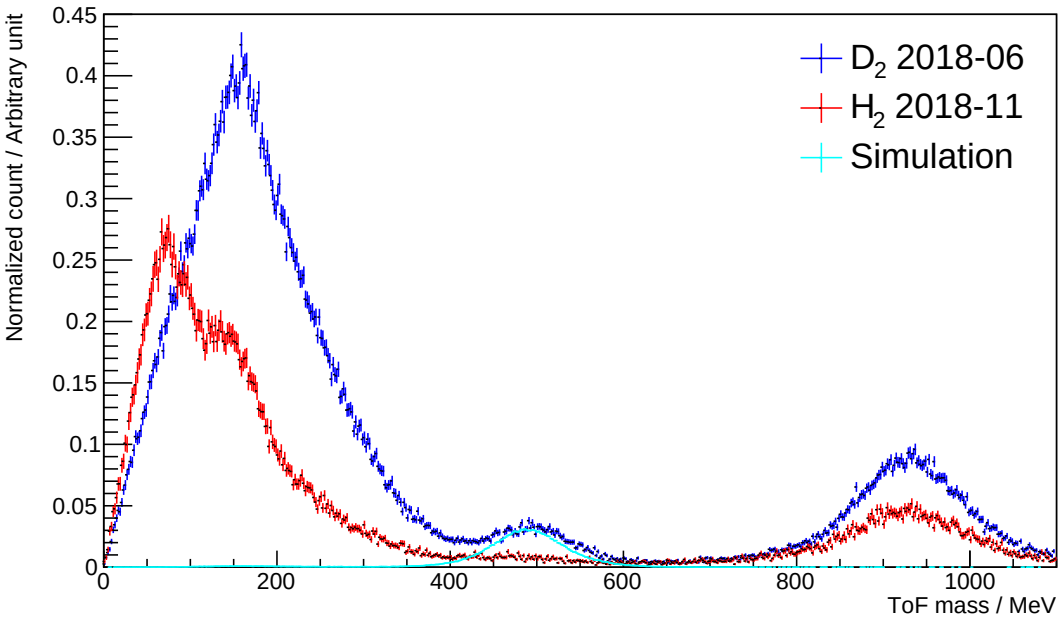

Figure 4.21: ToF mass for both beamtimes normalized by their respective flux, reconstruction efficiency and effective target area density over the full W range. The simulated data is shown with an arbitrary scale.

Starting from low to high ToF masses, visible are peaks corresponding to π^+ with some positron contribution, to the K^+ and to the proton. Generally speaking, the background contributions from π^+ and protons originating from the hydrogen dataset are approximately half the size of the corresponding ones originating from the deuterium dataset. The Gaussian peaks corresponding to the K^+ and proton are located around their particular masses as expected. However, even after careful calibration, the peaks corresponding to the π^+ show two deviations from the expected Gaussian shape and position: First, especially for the hydrogen dataset, the left flank of the π^+ peak suffers from positron contribution originating from uncorrelated pair production. The positron background is highly sensitive to the beam position, which tends to slightly wander over the course of a beamtime, leading to different distortions for different beamtimes. Second, for the deuterium dataset, the Gaussian mean does not coincide with the nominal π^+ mass, but is shifted by about +20 MeV. These aberrations are caused by the fact that the FS calibration is achieved by matching the measured proton ToF mass to the nominal proton ToF mass, not being tailored specifically to the π^+. Furthermore, they are also influenced by the ToF mass being determined by momentum and β measurements, which, for the π^+, are greatly affected by low-energy corrections in the FS track-finding algorithm, which are complicated to model precisely. This has implications on the utilized methodology: If the match between both beamtimes were perfect, one could normalize both datasets and then directly subtract the hydrogen ToF mass spectrum

from the deuterium ToF mass spectrum, removing the background reactions originating off the proton inside the deuteron, and then model the remaining overlapping π^+ and K^+ peaks afterwards. The integral over the K^+ peak would then correspond to the final normalized yield M_S^n of the signal. Due to the mismatch of the π^+ peaks, a different methodology needs to be applied, which has been described previously in section 4.1: The π^+ background is eradicated for each individual beamtime, leaving a K^+ peak with corresponding yield N_{K^+Y} for each individual beamtime. The respective normalization and the subtraction of the two normalized yields is then done *afterwards*, resulting in the final normalized yield M_S^n. Fortunately, the proton peaks do not overlap with the K^+ peaks and can be ignored.

As the overlap of the π^+ and the K^+ peak grows larger with increasing W, a straightforward fit function that consists of the sum of two Gaussians is at some value of W no longer able to distinguish between the two peaks. Therefore, a more elaborate fitting method is used. The shape of the π^+ peak may differ between beamtimes, but it is almost identical to the shape that would be observed for a measurement of π^-, as the resolution of the FS and the involved kinematics are the same. Furthermore, the π^- peak does not contain any K^- contribution, as K^- are not produced in the relevant kinematic range. Therefore, there is no need to model the π^+ shape with a Monte Carlo simulation as it can be measured directly. For the measurement of the π^- peak, all aforementioned cuts are applied in the same way except for the charge signature: The positively charged track in the FS is exchanged for a negatively charged track in the FS. Figure 4.22(a) shows β vs. p for a normal charge signature, while figure 4.22(b) shows the same variables for a negatively charged track in the FS. When selecting a negative track, only contributions from π^- and electrons remain.

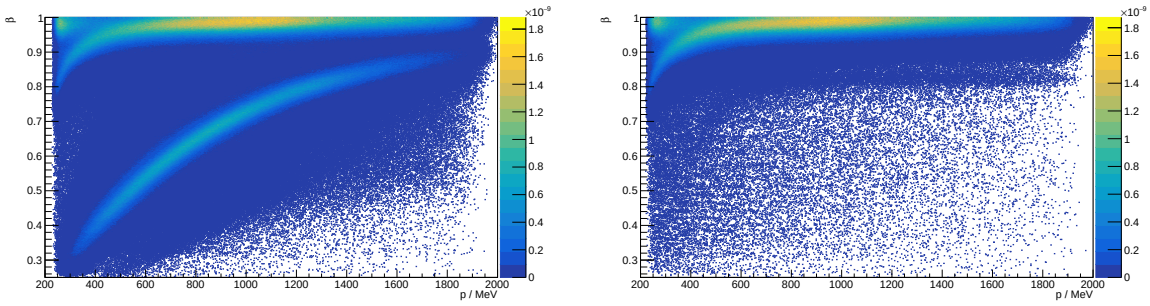

(a) Normal charge signature

(b) Negative FS track

Figure 4.22: β vs. p for (a) the normal charge signature and (b) the negative FS track.

The shape of the π^- peak describes the π^+ peak and the electron contribution in the former matches the positron contribution in the latter, while the distribution of the K^+ peak is modeled in the Geant4 simulation. The small π^+ peak in the simulated K^+ ToF mass spectrum, which originates from part of the K^+ decaying before entering the FS, contributes approximately 3% to its integral. It is excluded from the simulated ToF mass spectrum and from the calculation of the reconstruction efficiency, achieving a match between real data and simulation. The measured shape of the π^- peak as a π^+ model and the simulated K^+ peak are used as inputs for a maximum likelihood fit to the real ToF mass spectrum utilizing the RooFit [70] library of ROOT [69]. During the fitting routine, the input spectra are scaled to best describe the real data. The modeled π^+ spectrum and the K^+ spectrum were allowed to shift by ± 10 MeV along the x-axis to account for small deviations between simulation and real data. As the ToF mass spectra tend to show minor deviations from one another at ToF mass values close to zero, the lower end of the fitting range is set to 30MeV.

The bin width of the ToF mass spectra is set to 4 MeV.

For the sake of briefness, only the fits to every third W bin shall be shown here, while the goodness of fit will be shown over the full W range in which fits are necessary. The fits to each W bin can be found in appendix D. Figure 4.23 depicts the maximum likelihood fit to the ToF mass spectrum for different bins of W for the deuterium beamtime 2018-06. Note the different scales on the y-axes. The real data is shown in black, the peak that was measured using the π^- charge signature selection and then fitted is shown in blue and the K^+ peak that is a result of the Geant4 simulation and then fitted is shown in red. For the sake of clarity, the sum of the two peaks, which is the relevant quantity to maximize the likelihood, is not shown, as it largely overlaps with the individual peaks. The proton peak does not overlap with the K^+ peak and is not presented. The lower limit of the fitting range at 30 MeV is described by the vertical black dashed line.
The production threshold for $K^+\Sigma^-$ is $W = 1\,691.126$ MeV. It is located rougly at the centre of the first W bin, which encompasses $W = (1\,688.855 \pm 6.745)$ MeV, shown in figure 4.23(a). Thus, the K^+ signal is quite small for this bin. Up to a CM energy including $W = (1\,793.565 \pm 6.355)$ MeV, the 3σ distances of the π^+ and K^+ peaks do not overlap and therefore no fit needs to be applied, the integral can be taken directly over the full K^+ ToF mass peak. This eliminates any fitting uncertainty. This W range encompasses figures 4.23(a), 4.23(b) and 4.23(c), which is why no fitted ToF mass spectra are displayed. The 3σ distances overlap starting from $W = (1\,806.230 \pm 6.310)$ MeV, described by figure 4.23(d), and fits become necessary. As W increases, so does the width of the π^+ peak. Initially, a clear distinction between the two peaks is possible, but gets increasingly hard from $W = (1\,911.460 \pm 4.450)$ MeV, until no distinction is possible anymore above $W = (1\,942.350 \pm 8.760)$ MeV. The original tagger binning converted to a W binning was kept for most of the used W range, only the last two original bins at $W = (1\,937.980 \pm 4.390)$ MeV and $W = (1\,946.740 \pm 4.370)$ MeV were merged to form a single bin to gain sufficient statistics.

Figure 4.24 shows the analogous spectra for hydrogen beamtime 2018-11. Note that the spectra use the same colours as in the previous figure 4.23. As expected, the K^+ peak is generally smaller when compared to the deuterium beamtime.

Figure 4.25 shows the reduced χ^2 for the fits for both beamtimes depending on W. The figure only describes the W range in which fits are actually necessary due to the overlap of the π^+ and K^+ peak. In most cases the reduced χ^2 has a reasonable value and varies between 0.7 and 1.2. For the deuterium beamtime, the average absolute deviation from 1.000 is 0.196, while for the hydrogen beamtime, it is 0.273.

At this point of the analysis, the measured yield N_{K^+Y} is extracted for each individual beamtime by integrating over the known K^+ peak in the respective ToF mass spectrum after the fit. The next section will describe how the yields are normalized.

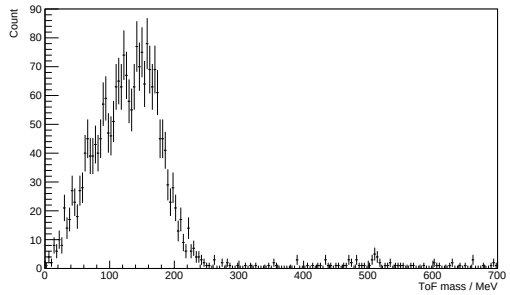

(a) $W = (1\,688.855 \pm 6.745)$ MeV

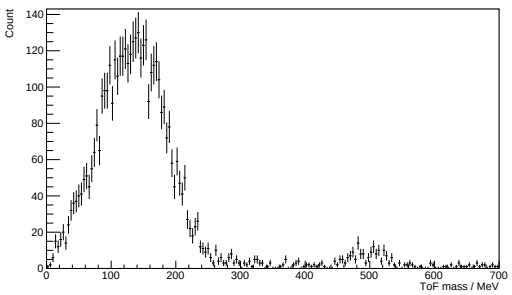

(b) $W = (1\,728.865 \pm 6.595)$ MeV

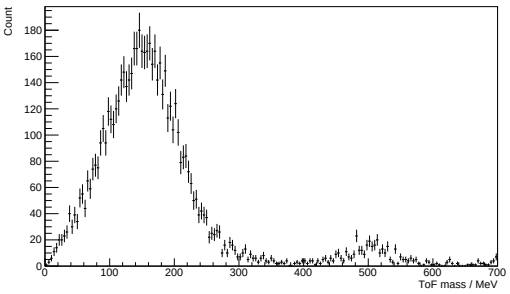

(c) $W = (1\,767.970 \pm 6.450)$ MeV

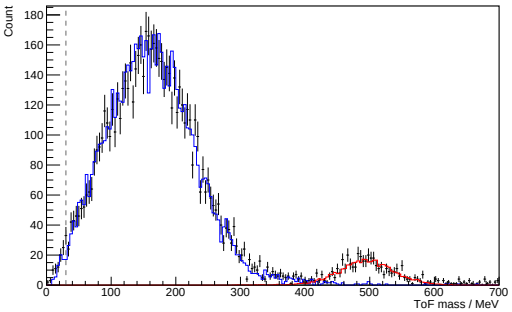

(d) $W = (1\,806.230 \pm 6.310)$ MeV

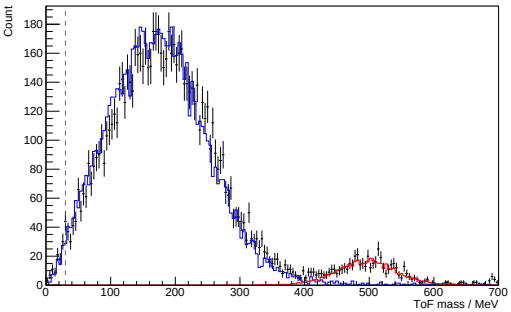

(e) $W = (1\,843.690 \pm 6.180)$ MeV

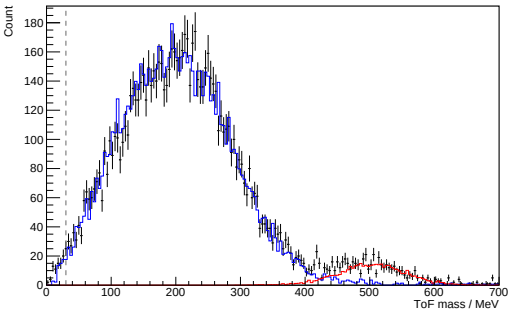

(f) $W = (1\,880.410 \pm 6.060)$ MeV

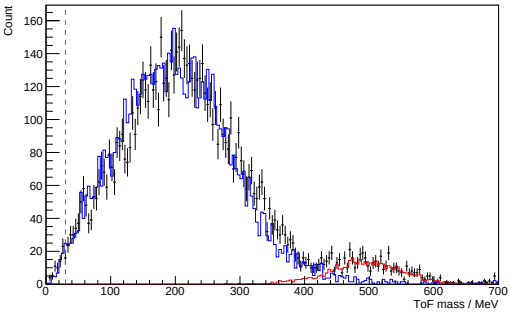

(g) $W = (1\,911.460 \pm 4.450)$ MeV

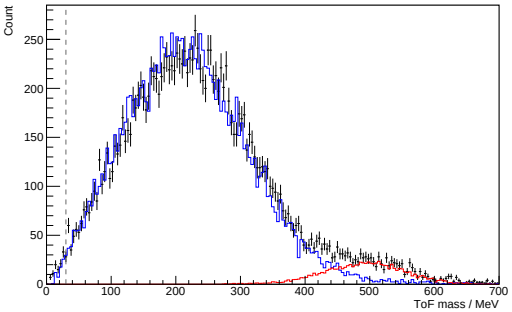

(h) $W = (1\,942.350 \pm 8.760)$ MeV

Figure 4.23: Maximum likelihood fit to the ToF mass spectrum of deuterium beamtime 2018-06 for selected bins of W. Real data shown in black, fitted π^+ model in blue and simulated K^+ peak in red. Fits become necessary from inclusive $W = 1\,806$ MeV on upward. The fitting region is restricted to above 30 MeV as depicted by the vertical line. Note the different scales on the y-axes.

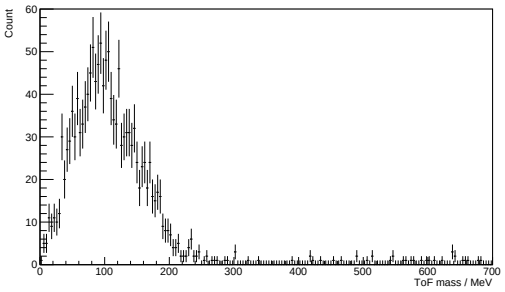

(a) $W = (1\,688.855 \pm 6.745)$ MeV

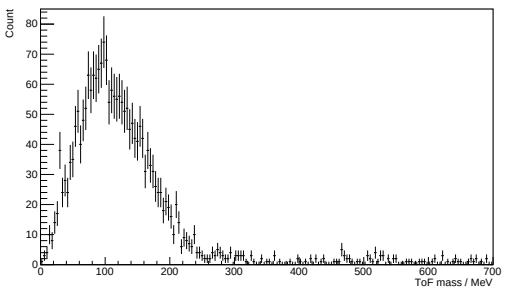

(b) $W = (1\,728.865 \pm 6.595)$ MeV

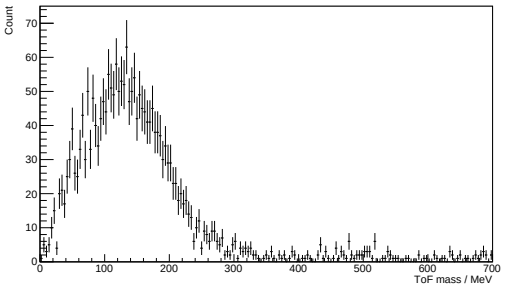

(c) $W = (1\,767.970 \pm 6.450)$ MeV

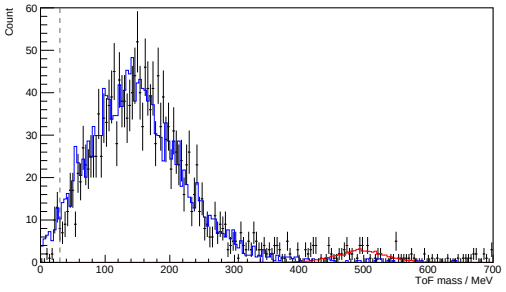

(d) $W = (1\,806.230 \pm 6.310)$ MeV

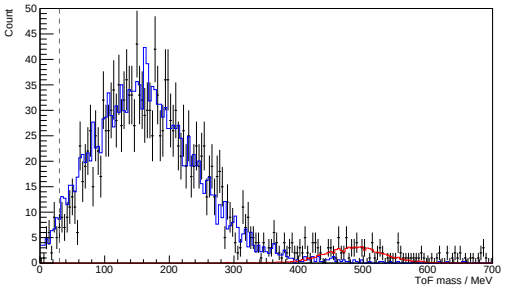

(e) $W = (1\,843.690 \pm 6.180)$ MeV

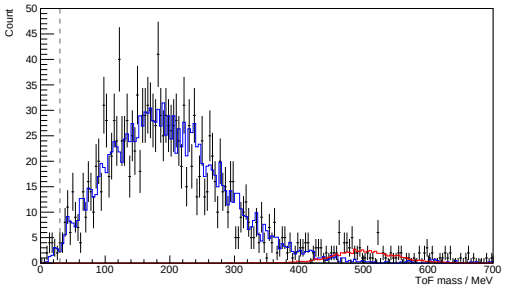

(f) $W = (1\,880.410 \pm 6.060)$ MeV

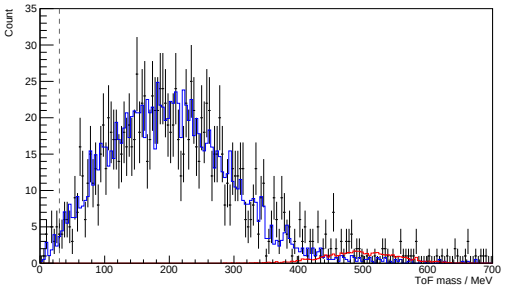

(g) $W = (1\,911.460 \pm 4.450)$ MeV

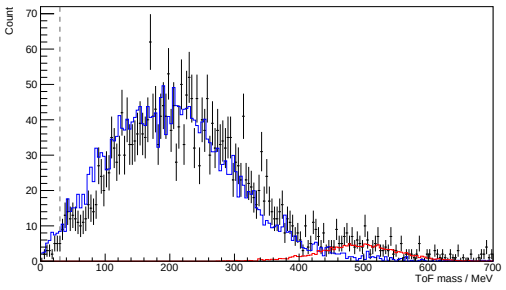

(h) $W = (1\,942.350 \pm 8.760)$ MeV

Figure 4.24: Maximum likelihood fit to the ToF mass spectrum of hydrogen beamtime 2018-11 for selected bins of W. Note the caption of figure 4.23.

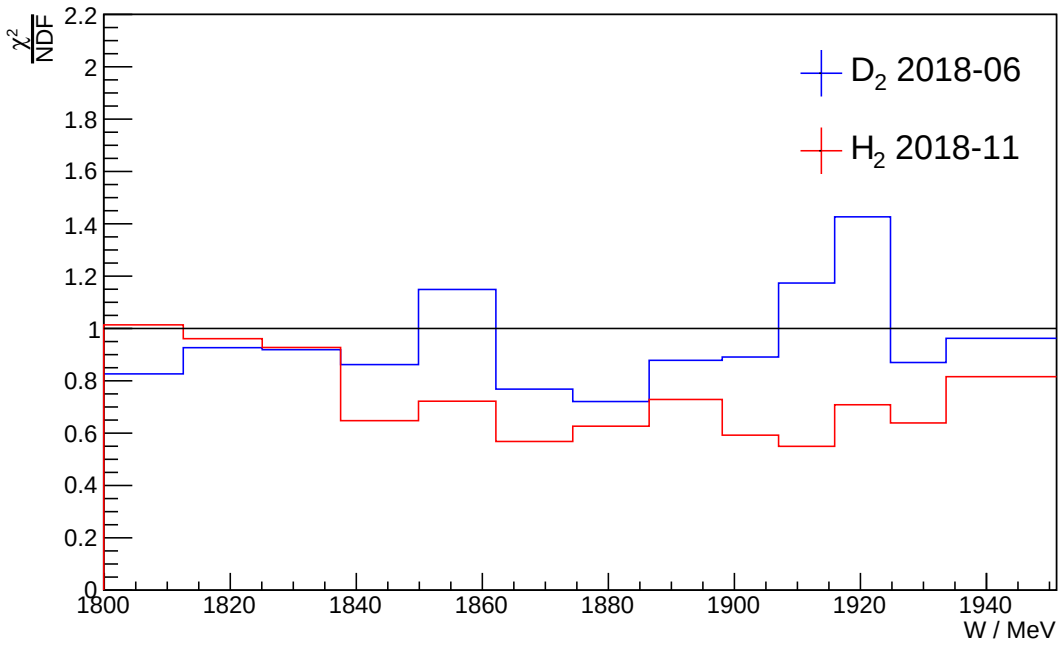

Figure 4.25: Reduced χ^2 depending on W for both beamtimes. Shown is only the W range in which fits are actually necessary. For the deuterium beamtime, the average absolute deviation from 1.000 is 0.196, while for the hydrogen beamtime, it is 0.273.

4.2.3 Normalization of the Yield N_{K^+Y}

As previously described by equation 4.5, the measured yields $N_{K^+Y}(W, \theta_{\mathrm{CM}})$ of the different beamtimes must be normalized by the respective integrated photon fluxes $N_\gamma(W)$, target area densities ρ and trigger efficiency ratio $\frac{\zeta^d}{\zeta^p}(W, \theta_{\mathrm{CM}})$ before the contribution of background off the proton can be subtracted:

$$\frac{N_{\mathrm{S}}^n}{N_\gamma^n \rho_n} = \frac{N_{\mathrm{S+BG}}^d}{N_\gamma^n \rho_n} - \frac{N_{\mathrm{BG}}^p}{N_\gamma^p \rho_p} \cdot \frac{\zeta^d}{\zeta^p} \,. \tag{4.5}$$

The following sections will describe how these parameters have been determined.

Integrated Photon Flux

The measurement of the integrated photon flux and the associated calibrations have been described in section 3.3. The integrated photon flux can be described as the product of the amount of electrons that cause coincidences in the tagging system and the tagging efficiency. The resulting energy spectrum of the incoming photons follows a $\frac{1}{E_\gamma}$ bremsstrahlung distribution, the conversion between the E_γ spectrum and the W spectrum was described in section 4.2.1. Figure 4.26 shows the integrated photon flux N_γ as a function of W for both beamtimes. The steps in the spectrum are a result of increasing bin widths for increasing W. For the sake of clarity, the original W binning is presented, whereas in the final result two bins will be merged

starting with the ones at $W = (1\,937.980 \pm 4.390)$ MeV and $W = (1\,946.740 \pm 4.370)$ MeV.
In about 4% of the cases, in real data, two photons are recorded for the same event. This effect can be corrected for by calculating the MM to the K^+ for both photons and discarding the one for which the MM is the most different to the nominal Σ^- mass.

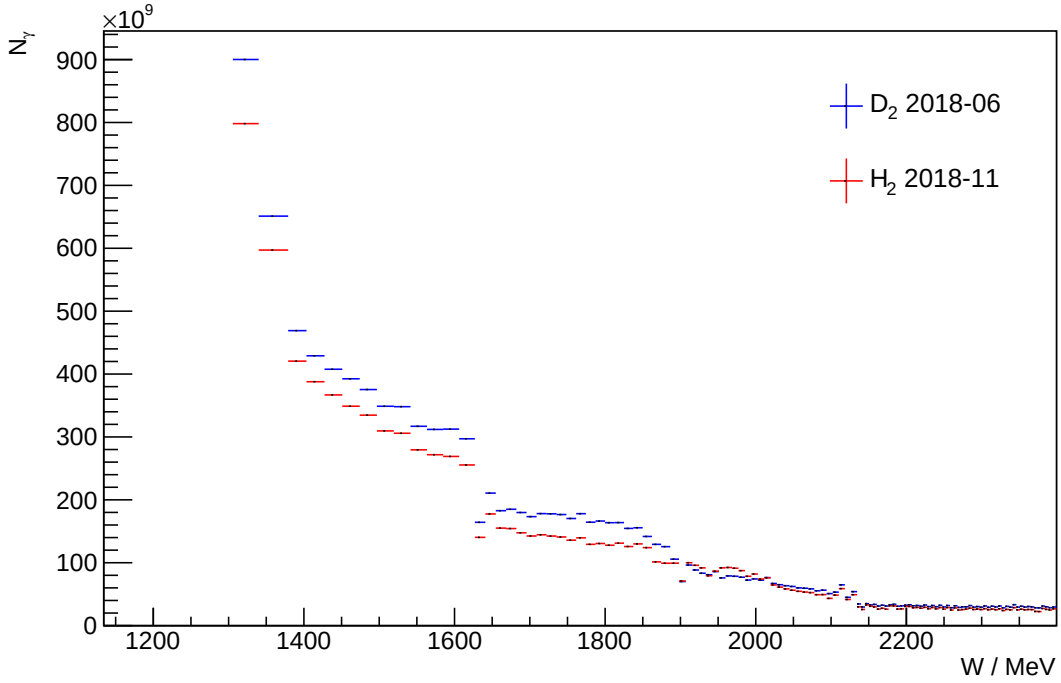

Figure 4.26: Integrated photon flux N_γ as a function of W for both beamtimes. The steps in the spectrum are a result of increasing bin widths for increasing W. For the sake of clarity, the original W binning is presented, whereas in the final result two bins will be merged starting with the ones at $W = (1\,937.980 \pm 4.390)$ MeV and $W = (1\,946.740 \pm 4.370)$ MeV.

Target Area Density

For all beamtimes, the same target cell with an effective length of $l = (11.1 \pm 0.1)$ cm was used, where the effective length factors in the slight elongation due to the curvature of the target cell windows made of Mylar foil. It was cooled down using the cryostat system to just above the freezing temperature in order to not destroy the target cell. For deuterium the temperature was held at 21.5 K and for hydrogen at 18.0 K. Table 4.1 lists the target densities [88]. The target area density ρ can then be calculated by multiplying these densities with the effective target length. As both beamtimes use the same target cell, the influence of the Mylar foil is canceled out during the subtraction procedure.

Trigger Efficiency Ratio

The trigger system was described in section 2.3 and the trigger efficiencies of the two beamtimes in

Material	Nucleus density $\left(\frac{1}{\mathrm{m}^3}\right)$	Proton density $\left(\frac{1}{\mu\mathrm{b}\cdot\mathrm{cm}}\right)$	Neutron density $\left(\frac{1}{\mu\mathrm{b}\cdot\mathrm{cm}}\right)$
Liquid hydrogen	4.237×10^{28}	4.237×10^{-8}	0
Liquid deuterium	5.053×10^{28}	5.053×10^{-8}	5.053×10^{-8}
Mylar foil	6.403×10^{28}	4.136×10^{-7}	4.111×10^{-7}

Table 4.1: Nucleus, proton and neutron densities for different materials [88]

section 3.2. For the performed analysis, the events were triggered by trigger 4 and some of them additionally by trigger 0. Thus, the trigger efficiency $\zeta_{\mathrm{BGO}}^{\mathrm{Low}}$ of the low BGO energy sum and the trigger efficiency ζ_{FS} of the forward track selection are relevant. It was shown that the trigger efficiencies of hydrogen beamtime 2018-11 are slightly lower than for deuterium beamtime 2018-06. This means that for the measurement of N_{BG}^{p}, which is the count of background reactions off the proton that was measured during hydrogen beamtime 2018-11, fewer events have been detected relative to the background contribution in the measurement of $N_{\mathrm{S+BG}}^{d}$ during deuterium beamtime 2018-06 even after normalization by N_γ and ρ. In order to correct for this effect, N_{BG}^{p} must be scaled by the ratio $\frac{\zeta^d}{\zeta^p}$ of the trigger efficiencies of trigger 4 of the two beamtimes. The ratio $\frac{\zeta^d}{\zeta^p}$ was determined once by simulating the reaction $\gamma p \rightarrow K^+\Lambda$ for both beamtimes and once by simulating $\gamma p \rightarrow K^+\Sigma^0$ for both beamtimes, as these are the reaction channels that contribute to N_{BG}^{p}, while the contribution of $\gamma p \rightarrow K^+\Sigma^0(1385)$ is negligible. Figure 4.27 shows $\frac{\zeta^d}{\zeta^p}$ as a function of W for $\cos(\theta_{\mathrm{CM}}) > 0.9$ for both simulated reaction channels. The W dependency appears to be negligible and the trigger efficiency ratios can be described by constant fit functions. The fit to $K^+\Lambda$ implies a scaling factor of $\frac{\zeta^d}{\zeta^p}(K^+\Lambda) = (1.1319 \pm 0.0040)$ and the one to $K^+\Sigma^0$ a scaling factor of $\frac{\zeta^d}{\zeta^p}(K^+\Sigma^0) = (1.0984 \pm 0.0061)$. As the relative background contributions of $K^+\Lambda$ and $K^+\Sigma^0$ are a priori unclear, the rounded mean value $\frac{\zeta^d}{\zeta^p} = (1.1151 \pm 0.0036)$ is used as a scaling factor. Theoretically, the deviation of the mean value to the other two values, which is of the order of 1.5%, could be used as an estimate of the associated systematic uncertainty. In practice, this systematic uncertainty affects only N_{BG}^{p}, which is several times smaller than $N_{\mathrm{S+BG}}^{d}$ over the vast majority of the whole W range, reducing the effective contribution of this systematic uncertainty to close to zero. For these reasons, the systematic uncertainty associated with the determination of the trigger efficiency ratio will be considered negligible.

The resulting normalized counts will be shown in the next section 4.2.4 in combination with the subtraction of the contribution of background off the proton.

4.2.4 Subtraction of the Contribution of Background off the Proton

At this point of the analysis, the yields $N_{K^+Y}(W, \theta_{\mathrm{CM}})$ have been extracted from the ToF mass spectra of both beamtimes as described in section 4.2.2.5 and the normalization factors have been determined as described in section 4.2.3. Applying the normalization factors to the yields leads to equation 4.4, which describes the desired normalized yield M_{S}^{n} of the signal reaction $\gamma n \rightarrow K^+\Sigma^-$ as the subtraction of the normalized count M_{BG}^{p} that originates from background reactions off the proton from the normalized count $M_{\mathrm{S+BG}}^{d}$ that is measured when using a deuteron target:

$$M_{\mathrm{S}}^{n} = M_{\mathrm{S+BG}}^{d} - M_{\mathrm{BG}}^{p} \,. \tag{4.4}$$

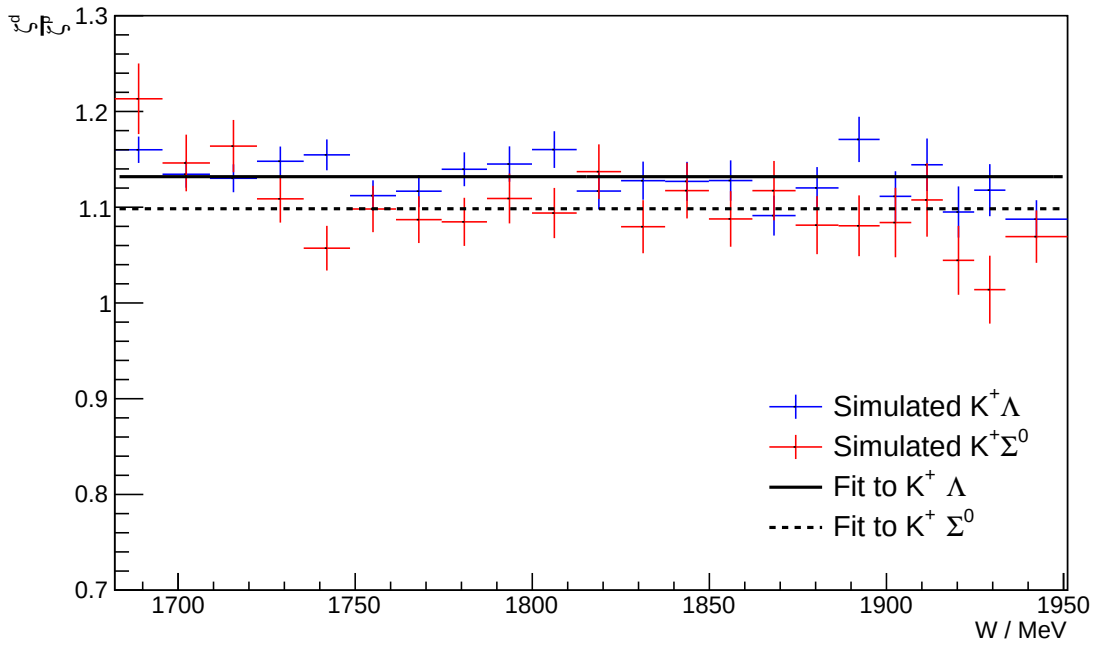

Figure 4.27: Trigger efficiency ratio $\frac{\zeta^d}{\zeta^p}$ of trigger 4 of deuterium beamtime 2018-06 and hydrogen beamtime 2018-11. The ratio was determined as a function of W for $\cos(\theta_{\mathrm{CM}}) > 0.9$ by simulating the reactions $\gamma p \to K^+\Lambda$ (blue) and $\gamma p \to K^+\Sigma^0$ (red) for both beamtimes, respectively.

The normalized counts are presented in figure 4.28. The normalized count of the deuterium beamtime is shown in blue, the one of the hydrogen beamtime in red and the one as a result of the subtraction in cyan. For most of the W range, the normalized count of the hydrogen beamtime fluctuates around 0.001 µb, while the normalized count of the deuterium beamtime rises roughly linearly up to about 0.009 µb at the end of the used W range. The normalized count as a result of the subtraction also rises roughly linearly and then shows a jump at $W = (1\,902.540 \pm 4.470)$ MeV.

4.2.5 Reconstruction Efficiency and Solid Angle Element

In order to determine the final DCS, the measured normalized yield $M_{\mathrm{S}}^n(W, \theta_{\mathrm{CM}})$ of the signal reaction $\gamma n \to K^+\Sigma^-$ must be divided by the reconstruction efficiency $\epsilon(W, \theta_{\mathrm{CM}})$ and the solid angle element Ω as previously described by equation 4.6:

$$\left(\frac{d\sigma}{d\Omega}\right)_{\mathrm{S}}^{n} = \frac{M_{\mathrm{S}}^n}{\epsilon\,\Omega} = \frac{N_{\mathrm{S}}^n}{N_\gamma\,\rho_n\,\epsilon\,\Omega}\,. \tag{4.6}$$

This section will describe how the reconstruction efficiency was determined and how big the solid angle element is. The division will then be done in the subsequent section 4.2.6.

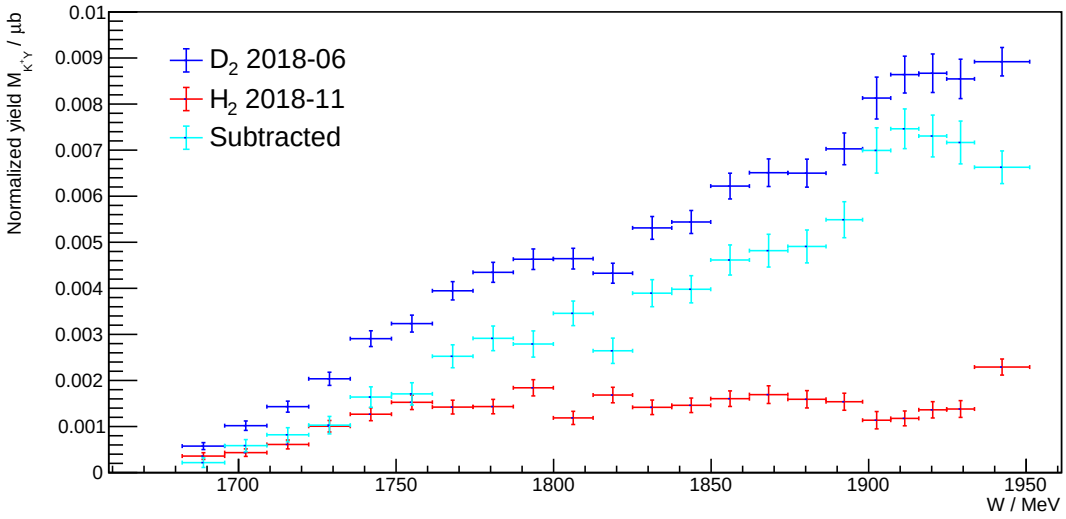

Figure 4.28: Normalized counts of the deuterium beamtime (blue), of the hydrogen beamtime (red) and as a result of the subtraction of the hydrogen data from the deuterium data (cyan).

Reconstruction Efficiency

The reconstruction efficiency $\epsilon(W, \theta_{\mathrm{CM}})$ can be modeled in Geant4, which was delineated in section 2.4.2. Given the specific reaction $\gamma n \rightarrow K^+\Sigma^-$ and having set the desired amount of events to $8 \cdot 10^7$, Geant4 first simulates the whole phase space and the associated particle tracks of the final state using Monte Carlo methods. It uses a full three-dimensional digital model of the experimental setup and emulates the resulting energy deposit of the particle tracks in the active detector material. The beamtime-specific detector response and trigger engagement variations are also included in the simulation. All cuts and methods that are applied to the real data are then also applied to the simulated data. The reconstruction efficiency is straightforwardly defined as the ratio of the number of events that remain after all cuts $N_{\mathrm{sim}}^{\mathrm{detected}}(W, \theta_{\mathrm{CM}})$ to the number of events that were initially generated by the simulation $N_{\mathrm{sim}}^{\mathrm{generated}}(W, \theta_{\mathrm{CM}})$:

$$\epsilon(W, \theta_{\mathrm{CM}}) = \frac{N_{\mathrm{sim}}^{\mathrm{detected}}(W, \theta_{\mathrm{CM}})}{N_{\mathrm{sim}}^{\mathrm{generated}}(W, \theta_{\mathrm{CM}})} \,.$$

Figure 4.29 shows $\epsilon(W)$ in an angular range of $\cos(\theta_{\mathrm{CM}}) > 0.9$. The vertical black line describes the W above no signal could be extracted anymore from real data.

The reconstruction efficiency has a maximum value of about 7.5%. The first bin is located at the CM energy $W = (1\,688.855 \pm 6.745)$ MeV and has an increased reconstruction efficiency compared to what the slope of the other data points would suggest. This is an artefact caused by the production threshold laying at $W = 1\,691.126$ MeV, meaning only one third of the bin covers a region above threshold. This implies that the number of simulated events $N_{\mathrm{sim}}^{\mathrm{generated}}$ is low in this particular W bin. The number of simulated events that are detected in simulation $N_{\mathrm{sim}}^{\mathrm{detected}}$ is affected by the experimental W resolution and Fermi smearing, described in section 4.2.1. The second W bin has a much higher count than the first one, inducing a dispro-

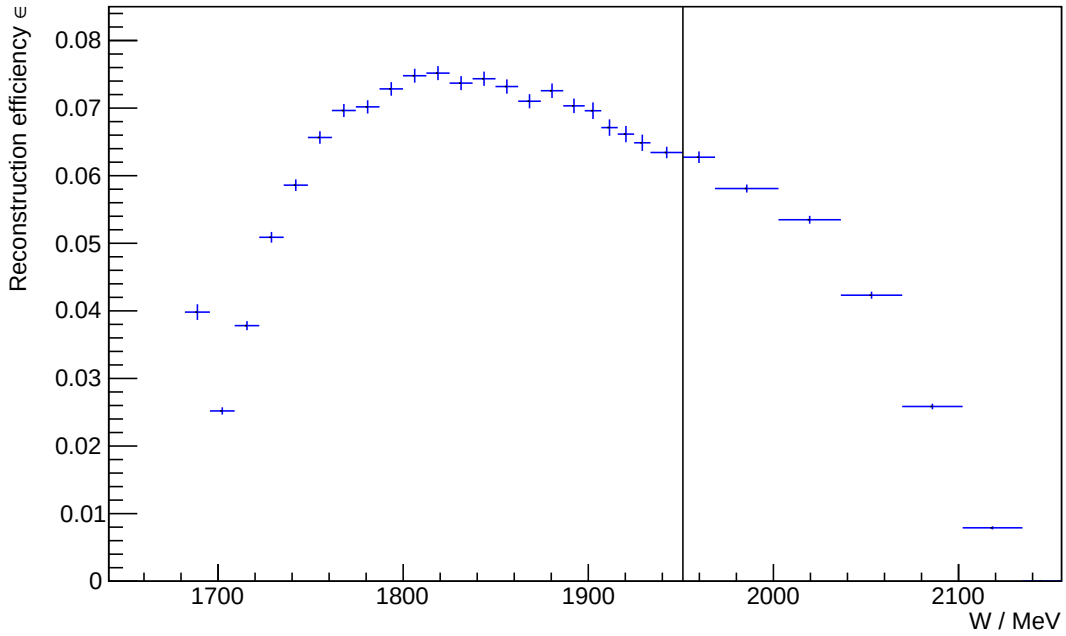

Figure 4.29: Reconstruction efficiency ϵ for the simulated reaction $\gamma n \to K^+ \Sigma^-$ depending on W in an angular range of $\cos(\theta_{\mathrm{CM}}) > 0.9$. The black vertical line describes the value of W above no signal could be extracted anymore from real data.

portionality between the amount of counts that the first bin looses by smearing versus the amount of counts that it gains by smearing, which increases the effective reconstruction efficiency for this particular bin. This effect is present in both real data and simulation.

Solid Angle Element

The data was taken at forward angles ranging from $\cos(\theta_{\mathrm{CM}}) = 0.9$ to $\cos(\theta_{\mathrm{CM}}) = 1.0$, so the solid angle element is $\Omega = 2\pi \cdot \Delta \cos(\theta_{\mathrm{CM}}) = 2\pi \cdot 0.1$.

4.2.6 Determination of the Differential Cross Section

Finally, the DCS of the reaction $\gamma n \to K^+ \Sigma^-$ can be determined by dividing the normalized count $M_{\mathrm{S}}^n(W, \theta_{\mathrm{CM}})$, which was presented in figure 4.28, by the reconstruction efficiency $\epsilon(W, \theta_{\mathrm{CM}})$, which was presented in figure 4.29, and the solid angle element $\Omega = 2\pi \cdot 0.1$. The result is shown in figure 4.30. Noticeable is a roughly linear rise up to $\frac{d\sigma}{d\Omega} = 0.124 \frac{\mu\mathrm{b}}{\mathrm{sr}}$ at $(1\,892.270 \pm 5.800)$ MeV. The DCS then jumps to $0.177 \frac{\mu\mathrm{b}}{\mathrm{sr}}$ at $(1\,911.460 \pm 4.450)$ MeV.

The determination of the normalized yield of the signal M_{S}^n was done under the assumption that the contribution of background off the neutron M_{BG}^n and the contribution of FSI effects $A_{\mathrm{FSI}}^{p,n}$ are small. This assumption shall be tested in the following sections 4.3 and 4.4. The next chapter 5 will then describe the statistical

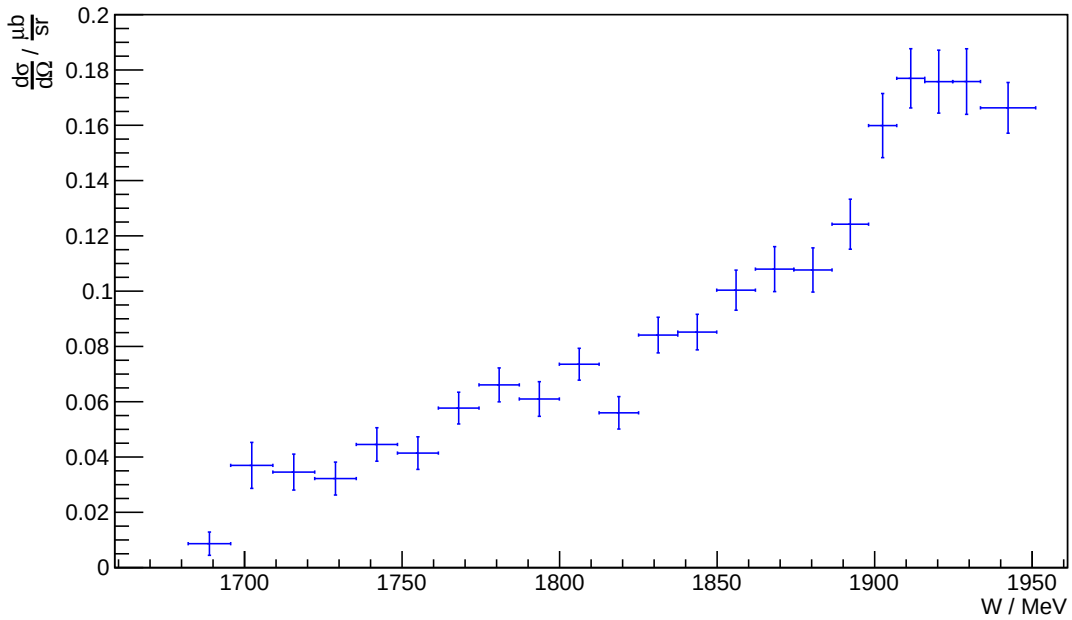

Figure 4.30: DCS of the reaction $\gamma n \to K^+ \Sigma^-$ as a function of W in an angular range of $\cos(\theta_{\mathrm{CM}}) > 0.9$. A detailed discussion including the systematic uncertainties can be found in chapter 6.

and systematic uncertainties. The final result under consideration of the uncertainties will be presented and discussed in chapter 6.

4.3 Contribution of Background off the Neutron

The contribution of background channels originating off the neutron can theoretically be determined in two different ways: One method would be to take preexisting reference DCS measurements of the contributing channels into consideration and subtract them from the DCS that is measured for reactions off the neutron. Data for the contributing channels are either scarce or nonexistent though, rendering this method unavailable. The second option is to compare the reconstruction efficiency of $\gamma n \to K^+\Sigma^-$ to the reconstruction efficiencies off the background channels and to make the reasonable assumption that the DCS of each individual channel is approximately of the same magnitude as the DCS for $K^+\Sigma^-$. The resulting reconstruction efficiency of all combined background channels relative to the one of $K^+\Sigma^-$ can then be used as an estimate of the systematic uncertainty. Table 4.2 lists the reaction channels off the neutron together with their production threshold, reconstruction efficiency ϵ and fraction of their reconstruction efficiency compared to the one of $K^+\Sigma^-$. The determination of the reconstruction efficiency is explained in section 4.2.5.

Reaction channel	Production threshold / MeV	Overall ϵ / %	Fraction of ϵ of $K^+\Sigma^-$ / %
$K^+\Sigma^-$	1691	5.8011	100.0000
$K^+\Sigma^-(1385)$	1881	0.0111	0.1913
$K^{*+}\Sigma^-$	2089	0.0000	0.0000
$K^0\Sigma^0$	1690	0.0023	0.0396
$K^{*0}\Sigma^0$	2088	0.0000	0.0000
$K^0\Sigma^{*0}$	1881	0.0009	0.0155
$K^0\Lambda$	1613	0.0126	0.2172
$K^{*0}\Lambda$	2011	0.0150	0.2586
$K^0\Lambda(1405)$	1903	0.0000	0.0000
$K^0\Lambda(1520)$	2017	0.0000	0.0000
$a_0(980)n$	1920	0.0000	0.0000
K^+K^-n	1927	0.0030	0.0517
ϕn	1959	0.0149	0.2568

Table 4.2: Reaction channels originating off the neutron and corresponding reconstruction efficiencies relative to the one of $K^+\Sigma^-$. Combining all reconstruction efficiencies under the simplified assumption that the reaction channels are open at the same time amounts to 1.0307% $\approx$ 1.03% of the one of $K^+\Sigma^-$.

All cuts and methods that were used in the $K^+\Sigma^-$ analysis except for the maximum likelihood fit were applied to the simulated data. Instead a 2σ cut around the K^+ ToF mass was applied. The reconstruction efficiencies are compared for each individual W bin above the listed production thresholds and then the average of these fractions is taken. All reconstruction efficiencies combined amount to a fraction of 1.0307% $\approx$ 1.03% of the reconstruction efficiency of $K^+\Sigma^-$, which is taken as an upper estimate of the associated systematic uncertainty. This estimate is considered an upper estimate, as it does not take into consideration that the production channels open up one after another with increasing W, letting the systematic uncertainty grow with every surpassed threshold. The estimated small size implies that even if each individual background channel would have a DCS that is multiple times larger than the DCS of $\gamma n \to K^+\Sigma^-$, the caused systematic uncertainty for the DCS measurement of $K^+\Sigma^-$ would still remain small.
To summarize, the contribution of background channels originating off the neutron M^n_{BG} that appears in equation 4.3 can be estimated to contribute a systematic uncertainty of 1.03% at most to the DCS measurement of $\gamma n \to K^+\Sigma^-$.

4.4 Contribution of Final State Interactions

Besides background reactions that originate directly from the initial state proton or initial state neutron, the DCS can potentially be affected by constructive or destructive interference of the wave functions of the produced final state particles and the remaining spectator proton. The extent of these FSI has been modeled theoretically by Salam and Arenhövel [89] and this section shall give a brief overview of their work.

The DCS is proportional to the square of the transition matrix element. For incoherent kaon photoproduction off the deuteron, the transition matrix element $M^{K\gamma d}_{\mu_Y \mu_N \mu_d \lambda}$ can be expressed by a corresponding photoproduction operator $\hat{M}^{K\gamma d}$ as follows:

$$M^{K\gamma d}_{\mu_Y \mu_N \mu_d \lambda}(\vec{p}_{YN}, \vec{p}_K, \vec{p}_\gamma) = \langle \vec{p}_{YN} \vec{p}_K \mu_Y \mu_N | \hat{M}^{K\gamma d} | \vec{p}_\gamma \mu_d \lambda \rangle \, .$$

Here, the $\vec{p}_i$ describe the three-momenta of the states indicated by the subscript, μ_i the spin orientation on some quantization axis and λ a phase parameter. A full treatment of all interaction effects would require a three-body treatment. Salam and Arenhövel approximate these complex effects by restricting their analysis to rescattering in the two-body subsystems of the final state. This approximation allows to write the production operator $\hat{M}^{K\gamma d}$ as the sum of four operators corresponding to individual types of interactions:

$$\hat{M}^{K\gamma d} = \hat{M}^{K\gamma d}_{\mathrm{IA}} + \hat{M}^{K\gamma d}_{YN} + \hat{M}^{K\gamma d}_{KN} + \hat{M}^{K\gamma d}_{K\pi} \, . \tag{4.12}$$

The operator $\hat{M}^{K\gamma d}_{\mathrm{IA}}$ describes the impulse approximation (IA), $\hat{M}^{K\gamma d}_{YN}$ hyperon-nucleon rescattering (YN), $\hat{M}^{K\gamma d}_{KN}$ kaon-nucleon rescattering (KN) and $\hat{M}^{K\gamma d}_{K\pi}$ pion mediated processes ($\pi N \rightarrow KY$), all of which are shown in figure 4.31 and shall be described in the following paragraphs.

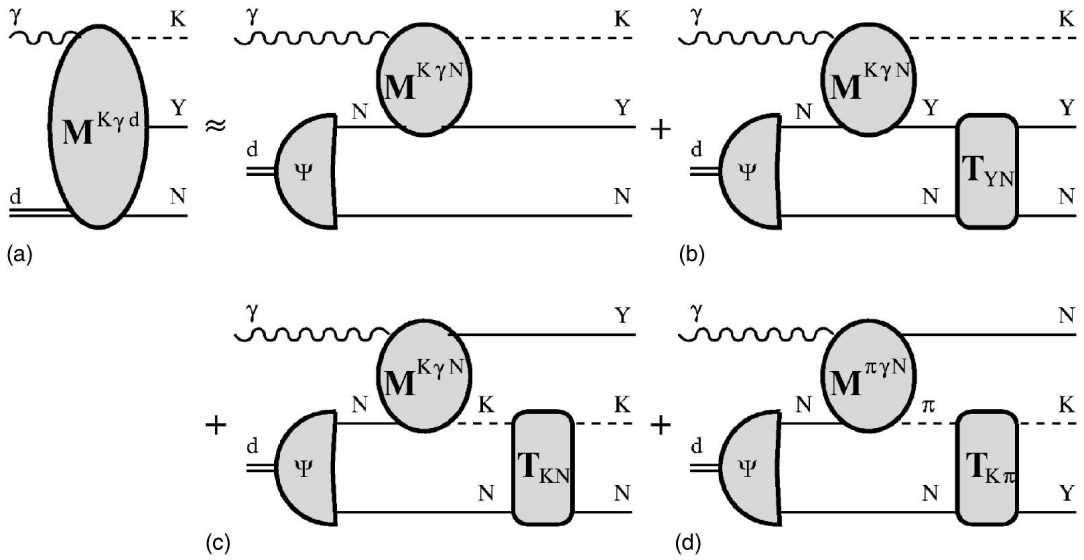

Figure 4.31: Incoherent kaon photoproduction on the deuteron including rescattering contributions in the two-body subsystems and the π-mediated process. Diagram (a): IA, (b): YN rescattering, (c): KN rescattering, (d): $\pi N \rightarrow KY$ process [89].

The impulse approximation describes the scenario where the incoming photon interacts with one nucleon only and produces a kaon, while the other nucleon remains as an unaffected spectator. Any subsequent interactions are neglected. This corresponds to the 'true' elementary DCS whose measurement is the goal of this thesis. In this straightforward description of kaon photoproduction, the driving terms of the corresponding production amplitude are the tree-level Feynman diagrams shown in figure 4.32. The authors include all of these effects except for the one described by diagram (e) in a so-called 'isobar model'. The coupling constants and coupling parameters were determined by fits to experimental data. For details about the included resonances, consult reference [89].

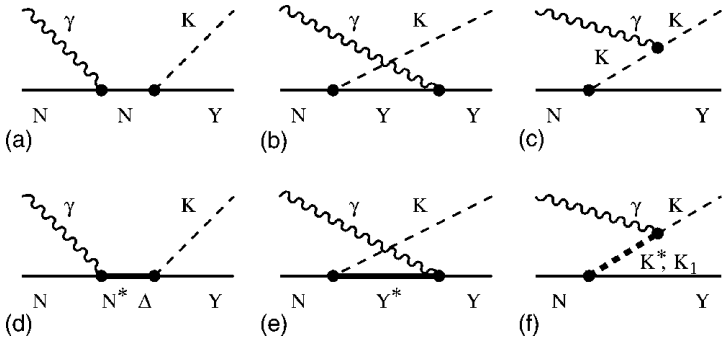

Figure 4.32: Elementary Feynman diagrams of kaon photoproduction contributing to the IA. Diagrams (a)-(c) show the Born terms for the nucleon, hyperon and kaon poles, respectively, whereas (d)-(f) show the resonance terms for the nucleon, hyperon and kaon resonance poles, respectively [89].

For a description of the hyperon-nucleon scattering the Nijmegen interaction potential is used [90][91]. The hyperon scatters off the nucleon via one-boson exchange. Since it is a baryon with strangeness $S = -1$, the exchange can contain both strange and non-strange mesons as illustrated in figure 4.33.

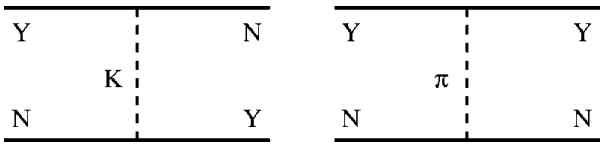

Figure 4.33: Boson exchange Feynman diagrams for the hyperon-nucleon potential, whereas the left diagram shows a strangeness exchange and the right one a nonstrangeness exchange [89].

Kaon-nucleon scattering is described by a rank-one separable interaction potential. The parameters of the potential are a result of fits to experimental data.

For the π-mediated processes the MAID model is used [92]. As depicted in figure 4.34, it contains Born terms, the vector mesons ρ and ω and various nucleon resonances. As the DCS of pion photoproduction is much stronger than the DCS for kaon photoproduction for most energies, π-mediated processes can potentially have sizable effects to the photoproduction operator.

The operators of the aforementioned effects are summed according to equation 4.12. Figure 4.35 shows the total cross section of the incoherent reaction $\gamma d \to K^+ \Sigma^- p$. More specifically, the figure presents the total cross section as a result of IA, of IA+YN, of IA+YN+KN and of IA+YN+KN+($\pi N \to KY$), respectively, as a fraction of IA. It is apparent that the total cross section shows a significant increase caused by YN res-

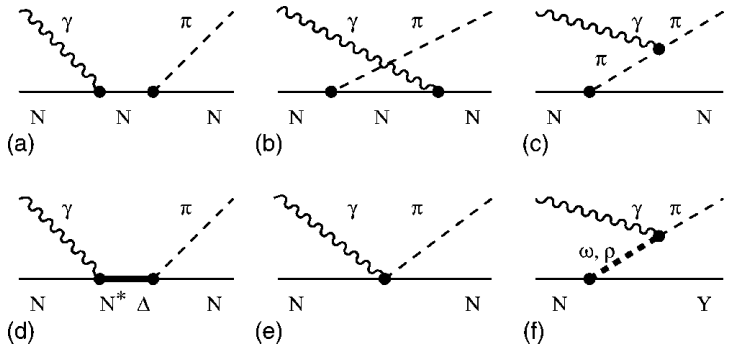

Figure 4.34: Elementary Feynman diagrams of pion photoproduction on the nucleon. Diagrams (a)-(c) show the Born terms for the nucleon, crossed-nucleon and pion poles, respectively, whereas (e) shows the Kroll-Rudermann contact term, (d) the resonance term and (f) vector meson exchange [89].

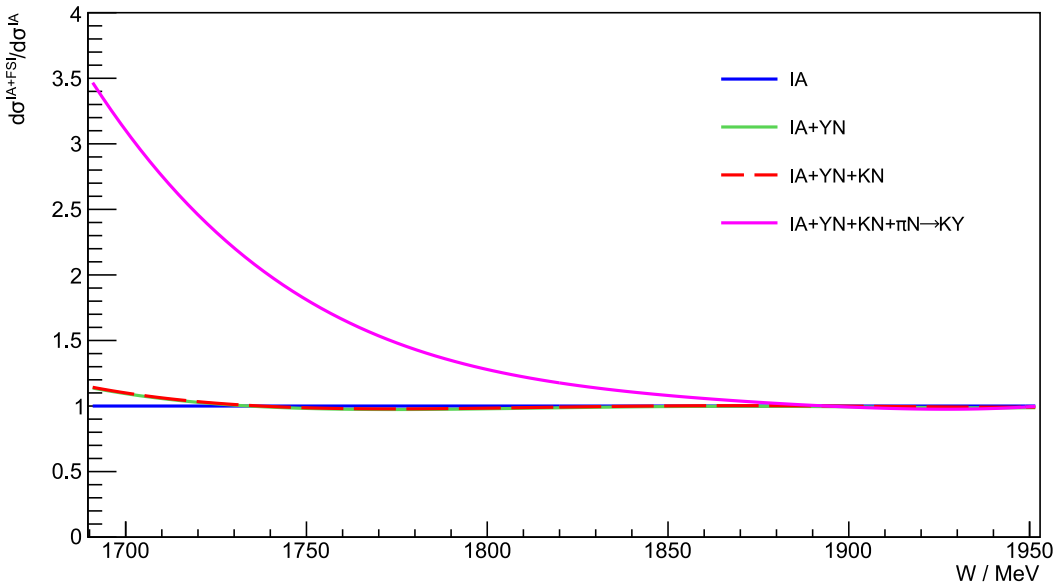

Figure 4.35: Total cross section of the incoherent reaction $\gamma d \to K^+\Sigma^- p$ as a result of IA (blue), of IA+YN (green), of IA+YN+KN (red) and of IA+YN+KN+($\pi N \to KY$) (magenta), respectively, as a fraction of IA. The running variable is the CM energy W. The latter effect dominates at threshold and decreases for increasing W. Figure adapted from reference [89].

cattering close to threshold, a tiny increase caused by KN rescattering and most dominantly a major increase caused by $\pi N \to KY$, which decreases for increasing W. Fortunately, these effects are highly dependent on the K^+ angle. Figure 4.36 shows the semi-inclusive DCS of the incoherent reaction $\gamma d \to K^+\Sigma^- p$ where only the K^+ is detected. Presented are the ratios of the IA to the other effects, analogous to figure 4.35, depending on the LAB angle θ_{LAB} for three different CM energies W. In forward direction, the DCS is reduced by YN rescattering and almost unaffected by KN rescattering. At threshold, the reduction is more than compensated by $\pi N \to KY$ processes. The FS covers a polar range from approximately $\theta_{\mathrm{LAB}} = 1.5°$ to

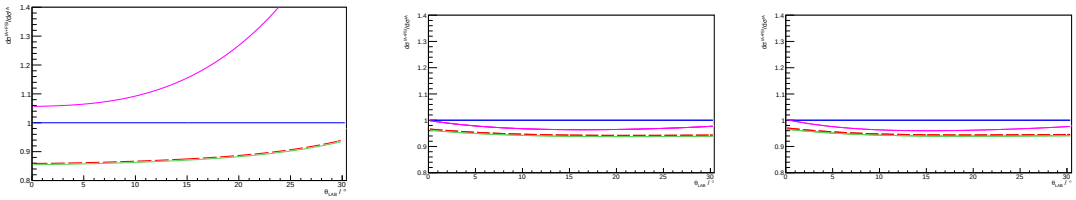

(a) $W = 1\,691\,\text{MeV}$ (b) $W = 1\,884\,\text{MeV}$ (c) $W = 1\,918\,\text{MeV}$

Figure 4.36: Semi-inclusive DCS of the incoherent reaction $\gamma d \to K^+ \Sigma^- p$ as a result of IA (blue), of IA+YN (green), of IA+YN+KN (red) and of IA+YN+KN+($\pi N \to KY$) (magenta), respectively, as a fraction of IA. The running variable is the LAB angle θ_{LAB}, three different energies W are shown. The FSI increase the DCS at threshold and decrease the DCS at higher W. The average effect of all FSI over the FS region and the presented energies is about 7%. Figure adapted from reference [89].

$\theta_{\text{LAB}} = 10.0°$. In this angular range and averaging over all presented energies, when compared to the DCS that results from the pure IA, the combined FSI lead to a deviation of about 7%. As theoretical calculations for a fine W binning are unavailable, this value will be considered as an upper estimate across the whole W range [89].

When the final DCS is interpreted under the consideration that the contribution of the FSI is about 7%, the term $A^{p,n}_{\text{FSI}}$ in equation 4.3 can be set to zero. The estimated value must be treated with reservation though: The theoretical FSI model was developed under simplified assumptions and relies partly on fits to experimental data, which, at the time of publication of the corresponding paper, was even more scarce than today. Still, it is the most encompassing description of FSI available.

In chapter 5, it will be layed out that the contribution of FSI to the DCS will be treated on a different footing than the systematic uncertainties, as FSI are an intrinsic property of measurements on the deuteron and other experiments will encounter the exact same effect on the measurement.

CHAPTER 5

Statistical and Systematic Uncertainties

For an adequate error analysis it must be distinguished between three types of uncertainties:

1. **Statistical uncertainties:** The statistical uncertainties of the event count $N(W, \theta_{\mathrm{CM}})$, the photon flux $N_\gamma(W)$ and the simulated event count $N_{\mathrm{sim}}^{\mathrm{detected}}(W, \theta_{\mathrm{CM}})$ that is used for the determination of the reconstruction efficiency correspond to the square roots of the respective counts and propagate further via Gaussian error propagation. The statistical uncertainties have always been included in the figures shown in the preceding chapters.

2. **Systematic uncertainties:** The systematic uncertainties can be divided into two sub-categories:
   a) **Scaling uncertainties:** These uncertainties affect all bins of the DCS distribution equally.
   b) **Fitting uncertainties:** These uncertainties are a result of the fit quality and affect the bins of the DCS distribution individually.

The scaling uncertainties can be divided further into two sub-categories: On the one hand, general scaling uncertainties that are caused by the hardware setup exist. These uncertainties are well-known and described in reference [93], the corresponding experimental conditions remained unchanged since the publication. Thus, these scaling uncertainties shall be adopted and only covered briefly here. On the other hand, scaling uncertainties that are unique to the methodology of the performed analysis of $\gamma n \to K^+\Sigma^-$ exist. Additionally, the DCS is affected by FSI effects, which are an intrinsic property of any measurement on the deuteron and not a systematic uncertainty in the strictest sense. Table 5.1 lists the types of scaling uncertainties together with their relative effects, the general scaling uncertainties are shown in the first section, the aforementioned unique scaling uncertainties in the second and the contribution of FSI effects to the DCS in the third.

The biggest contribution to the general scaling uncertainties stems from the beam spot alignment. A shifted beam affects the point at which the incoming electrons produce bremsstrahlung photons and from which the electrons are subsequently deflected into the tagger channels, influencing the assigned energy values. Furthermore, it affects the position at which the photon beam hits the target cell, which must match the geometry in simulation. The beam spot alignment is monitored regularly during beamtimes via dedicated wirescans and is subject to slight variations on a day-to-day basis. These variations are taken as a basis to model the associated systematic uncertainty.
The systematic uncertainty associated with the photon flux is determined by comparing the measurements

Source	Error / %
Beam spot alignment	4.00
Photon flux	4.00
Beam energy calibration	1.00
Target length	1.70
SciFi efficiency	3.00
DC efficiency	1.00
ToF wall efficiency	1.50
Track time selection	2.00
Forward track geometric selection	1.00
Modeling of hardware triggers	1.00
W assignment of flux	1.00
Charge signature selection of neutron	12.27
π^- kinetic energy cut	1.74
π^- momentum in Σ^- frame cut	4.62
MM to $K^+\pi^-$ cut	2.07
MM to K^+ cut	1.52
BG off neutron	1.03
FSI	7.00
Summed in quadrature excluding FSI	15.42%
Summed in quadrature including FSI	16.93%

Table 5.1: Systematic uncertainties contributing to the constant fractional error. The first section describes general analysis-independent uncertainties [93], the second section describes uncertainties that are unique to the methodology of the performed analysis and the third section describes FSI contributions which are intrinsic to any measurement on the deuteron. Excluding the FSI, taking the square root of the sum in quadrature leads to a total scaling uncertainty of 15.42%, which is the relevant value that will be considered for the uncertainty analysis. Including the FSI, it would amount to 16.93%.

of DCSs of well-known reactions like $\gamma p \to \pi^0 p$ or $\gamma p \to \eta p$ to reference data from other experiments.
The mapping of individual tagger channels to photon energies depends on an accurate representation of the tagger geometry including the magnetic field of the tagger magnet, variations of which can be described in simulation and are used as a systematic uncertainty to the beam energy calibration.
The cylindrical target cell contains target windows made of Mylar foil, which, when observed from the outside, are convex, increasing the effective length, which has been taken into consideration. Depending on the specific point of irradiation on the convex target foil, the effective target length changes, which is described by the corresponding systematic uncertainty.
The efficiencies of SciFi, the DCs and ToF have been determined by selecting events that give rise to a signal in all of those detectors and comparing them to events that only give a signal in a subset of them. These efficiencies have been included in simulation together with the associated systematic uncertainties.
Forward tracks require to select clusters within a certain time distance and spatial distance. Variations on these criteria are used as the systematic uncertainty for the track time selection and forward track geometric selection, respectively.
The systematic uncertainty of the hardware trigger modeling has been determined by variation of the local and global trigger criteria.

Contributing to the systematic scaling uncertainties that are unique to the methodology of the performed analysis, the uncertainty originating from the W assignment to the E_γ flux has been described in section 4.2.1. The conversion to a W flux has been performed once under the assumption of a static target and once under the assumption of a moving target, and the deviation appears to be small. It only plays a significant role at the very edges of the flux spectrum.
The charge signature selection in which neutral tracks are not allowed is the biggest contributor. It has been estimated in section 4.2.2.1 by using GRAAL measurements [87] of the neutron detection efficiency of the BGO. It is a one-sided uncertainty and can only scale the DCS up. An exact description of the neutron detection efficiency could help to decrease this uncertainty. A natural first step would be to replicate the GRAAL analysis for the current hardware setup of BGOOD.
As explained in section 4.2.2.2, a cut on 90% of the maximum kinetic energy deposit of the π^- in the BGO is applied. Sections 4.2.2.2, 4.2.2.3 and 4.2.2.4 show that the allowed π^- momentum in the Σ^- frame, the MM to $K^+\pi^-$ and the MM to the K^+ are normally distributed and 2σ cuts are applied. For an estimation of the systematic uncertainties associated with these cuts, they are varied and the standard deviation of the resulting change of the final DCS is used as the associated uncertainty. For the maximum kinetic energy deposit of the π^-, the whole analysis is performed using a cut of 85.0%, 87.5%, 90.0%, 92.5% and 95.0%. For the aforementioned three Gaussian distributions, the whole analysis is performed using a 1.50σ, 1.75σ, 2.00σ, 2.25σ and 2.50σ cut. The biggest impact is achieved by the cut on the allowed π^- momentum in the Σ^- frame.
The contribution of all relevant background channels off the neutron to the systematic uncertainty of the DCS measurement has been described in detail in section 4.3. It was modeled by simulating all relevant background channels, comparing their reconstruction efficiencies to the one of $K^+\Sigma^-$ and making the reasonable assumption that the involved DCSs are approximately of the same magnitude. The associated systematic uncertainty is 1.03%.

The contribution of potential FSI to the DCS has been estimated in section 4.4 based on theoretical calculations and is approximately of the order of 7%. It should be treated with reservation, as the associated theoretical calculations were carried out on a scarce data basis. The contribution of FSI shall be treated on a different footing than the systematic uncertainties. FSI are an intrinsic property to any measurement on the deuteron, meaning other experiments would encounter the exact same background contributions. Therefore, when calculating the total scaling uncertainty by taking the square root of the sum of the individual uncertainties in quadrature, the FSI are excluded, leading to a total value of 15.42%. This is the value which will be considered the true systematic scaling uncertainty which is presented together with the results in chapter 6. Including the FSI contribution would lead to a total scaling uncertainty of 16.93%.

The systematic fitting uncertainty has been determined by comparing the DCSs as results of different fitting methods. As described in section 4.2.2.5, there is no overlap between the π^+ and the K^+ ToF mass peaks up to including $W = (1\,793.565 \pm 6.355)$ MeV, therefore the integral is taken directly over the full K^+ ToF mass peak. Applying a maximum likelihood fit becomes necessary for higher W. The fit has been applied under the conditions of a ToF mass bin width of 4 MeV, a lower boundary of the fitting range at a ToF mass of 30 MeV and an allowed shift of the input spectra to the maximum likelihood fit along the ToF mass axis of $\pm$10 MeV. These conditions are varied as follows: For the bin width, values of 4 MeV, 6 MeV and 8 MeV are chosen. For the lower boundary of the fitting range, values at ToF masses of 0 MeV, 30 MeV and 60 MeV are selected. For the allowed shifts of the input spectra to the maximum likelihood fits along the ToF mass axis, values of 0 MeV, $\pm$10 MeV and $\pm$20 MeV are chosen. A DCS analysis is performed

for each of the 27 permutations of the aforementioned fitting conditions. For each bin of W, the resulting standard deviation of all DCS measurements is used as systematic fitting uncertainty. Note that at the W range of $W = (1\,793.565 \pm 6.355)$ MeV and below, as no maximum likelihood fit needs to be applied, there is no uncertainty related to the fitting procedure. However, there is an uncertainty associated with taking the integral between fixed borders when using different bin widths. This uncertainty will also be encompassed under the term 'fitting uncertainty'.

The fitting uncertainties are shown in figure 5.1 as the red data points. For $W = (1\,793.565 \pm 6.355)$ MeV and below, they have values of approximately 1% as a result of the variation of the bin widths. The two first W bins inherit slightly higher uncertainty values, as their ToF mass integrals are very small and thus the relative uncertainty is impacted stronger by fluctuations of the integral. Above excluding $W = (1\,793.565 \pm 6.355)$ MeV, the fitting uncertainties jump to values of about 4%, whereas the bins at $W = (1\,880.410 \pm 6.060)$ MeV and $W = (1\,892.270 \pm 5.800)$ MeV inherit values of roughly 7%. At $W = (1\,920.340 \pm 4.430)$ MeV, where a differentiation between the π^+ and the K^+ ToF mass peak becomes increasingly harder, the fitting uncertainty rises up and then reaches a maximum value of approximately 10%. The corresponding data points are described by an exponential fit of the form $\delta^{\text{Fitting}}_{\text{Syst.}}(W) = e^{\alpha+\beta\cdot W} \cdot 100$ with $\alpha = -26.295900$ and $\beta = 0.012249$, which is shown in figure 5.1 as the magenta line.

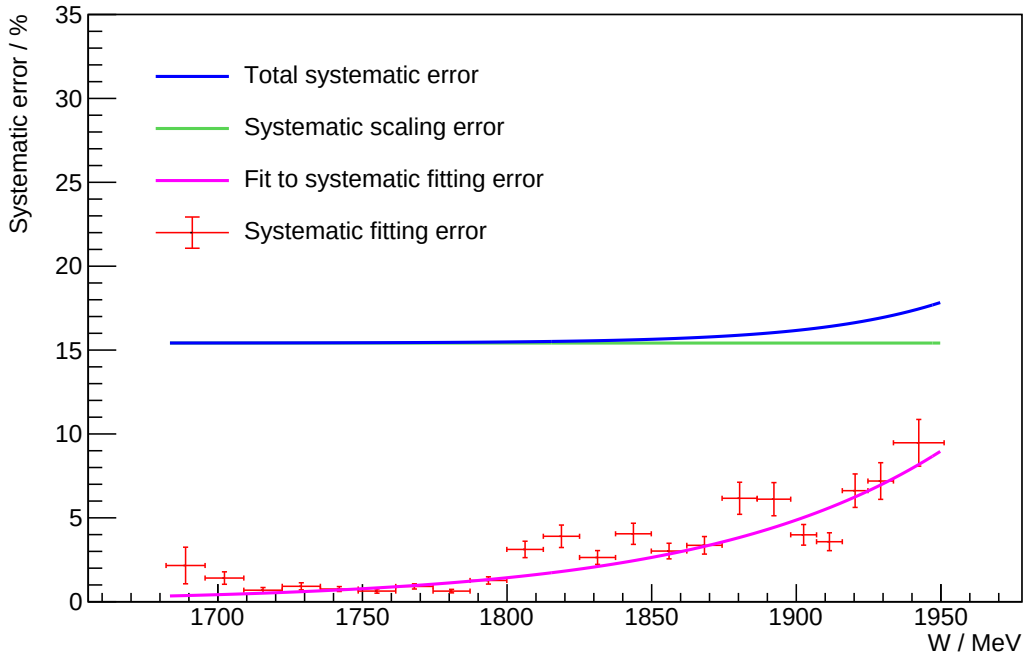

Figure 5.1: Systematic uncertainties. The scaling uncertainty $\delta^{\text{Scaling}}_{\text{Syst.}}$ is shown in green and is constant across all W. The fitting uncertainty $\delta^{\text{Fitting}}_{\text{Syst.}}$ is shown in red. The corresponding data points are described by an exponential fit of the form $\delta^{\text{Fitting}}_{\text{Syst.}}(W) = e^{\alpha+\beta\cdot W} \cdot 100$ with $\alpha = -26.295900$ and $\beta = 0.012249$ shown in magenta. The total systematic uncertainty $\delta^{\text{Total}}_{\text{Syst.}}$, which is the square root of the sum of the squares of the scaling uncertainty and the function that describes the fitting uncertainty, is shown in blue.

The major contribution to the total systematic uncertainty is achieved by the scaling uncertainty $\delta^{\text{Scaling}}_{\text{Syst.}}$, shown in figure 5.1 in green. Taking the square root of the sum of the squares of the scaling uncertainty $\delta^{\text{Scaling}}_{\text{Syst.}}$ and the function that describes the fitting uncertainty $\delta^{\text{Fitting}}_{\text{Syst.}}$ results in the total systematic uncertainty $\delta^{\text{Total}}_{\text{Syst.}}$ shown in blue, ranging from 15.42% at $W = (1\,688.855 \pm 6.745)$ MeV to 15.89% at $W = (1\,880.410 \pm 6.060)$ MeV to a maximum of 17.45% at $W = (1\,942.350 \pm 8.760)$ MeV.

CHAPTER 6

Results and Interpretation

The DCS of the reaction $\gamma n \to K^+ \Sigma^-$ has been measured in an angular range of $\cos(\theta_{\mathrm{CM}}) > 0.9$ at CM energies ranging from threshold, being $W = 1\,691\,\mathrm{MeV}$, up to $W = 1\,942\,\mathrm{MeV}$. It is shown in figure 6.1 in blue together with datasets from LEPS [51] in red and CLAS [50] in green. Importantly, the CLAS dataset has been measured at the less forward angle $0.8 < \cos(\theta_{\mathrm{CM}}) < 0.9$.

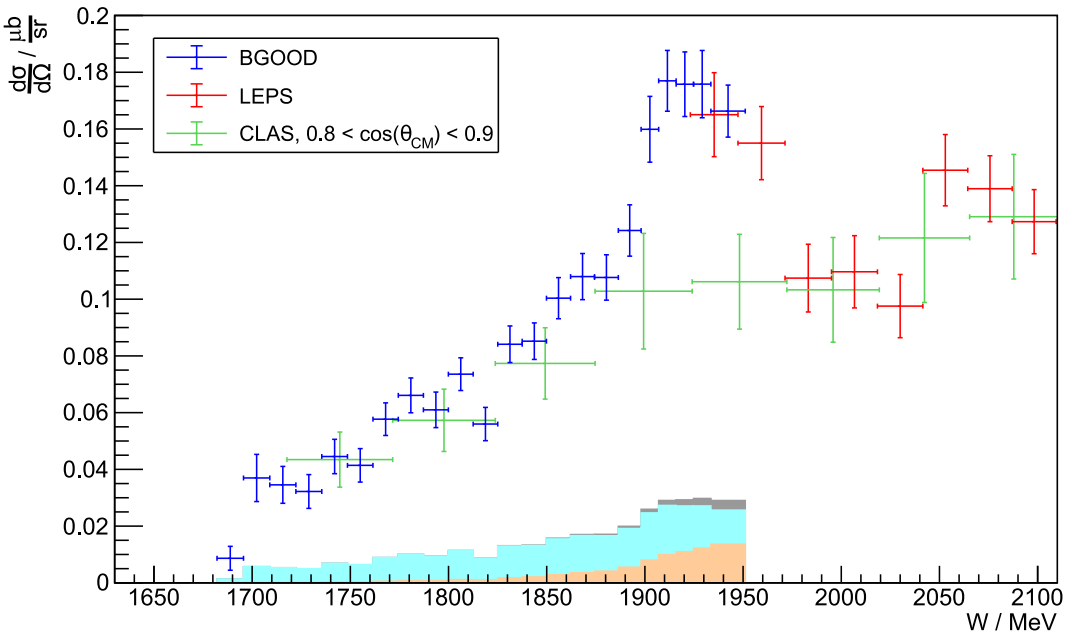

Figure 6.1: DCS of the reaction $\gamma n \to K^+ \Sigma^-$ in an angular range of $\cos(\theta_{\mathrm{CM}}) > 0.9$ in dependence of the CM energy W. The data of this analysis is shown in blue. A dataset from LEPS [51] is shown in red and a dataset from CLAS [50] in green, where the CLAS dataset has been measured at the less forward angle $0.8 < \cos(\theta_{\mathrm{CM}}) < 0.9$. Horizontal bars depict the bin widths while vertical bars depict the statistical errors. The absolute systematic fitting uncertainty $\delta^{\mathrm{Fitting}}_{\mathrm{Syst.}}$ is shown at the bottom in orange, the systematic scaling uncertainty $\delta^{\mathrm{Scaling}}_{\mathrm{Syst.}}$ in cyan and the total combined systematic uncertainty $\delta^{\mathrm{Total}}_{\mathrm{Syst.}}$ in grey.

The absolute systematic fitting uncertainty $\delta^{\text{Fitting}}_{\text{Syst.}}$ is shown at the bottom in orange, the systematic scaling uncertainty $\delta^{\text{Scaling}}_{\text{Syst.}}$ in cyan and the total systematic uncertainty $\delta^{\text{Total}}_{\text{Syst.}}$, which is the sum in quadrature, in grey. Practically the entire kinematic range covered by the present analysis has never been explored before. The W resolution is unprecedented and approximately twice as good as those achieved by LEPS and CLAS. For similar bins of W, the statistical error of the DCS is about half the size of the one of CLAS and two thirds of the one of LEPS.

The very first W bin is centred at $W = 1\,689\,\text{MeV}$ and encompasses the production threshold at $W = 1\,691\,\text{MeV}$, where the DCS starts at a relatively low value of $\frac{d\sigma}{d\Omega} = 0.009\,\frac{\mu\text{b}}{\text{sr}}$. From $W = 1\,702\,\text{MeV}$ to $W = 1\,892\,\text{MeV}$, the DCS then increases approximately linearly, reaching $0.124\,\frac{\mu\text{b}}{\text{sr}}$. The most striking feature of the obtained data is a sudden jump of the DCS in-between 1 892 MeV to 1 911 MeV, where the DCS increases from $0.124\,\frac{\mu\text{b}}{\text{sr}}$ to $0.177\,\frac{\mu\text{b}}{\text{sr}}$. This is an increase by $0.053\,\frac{\mu\text{b}}{\text{sr}}$, which corresponds to 43%, withing a W range of just 19 MeV. This increase can not be attributed to the statistical or systematic uncertainties. The biggest contributor to the systematic uncertainty is an overall scaling uncertainty that can not affect the extent of the jump. For the very last data point at 1 942 MeV, the DCS slightly drops to $0.166\,\frac{\mu\text{b}}{\text{sr}}$.

The last two data points overlap the W range of the LEPS data. The agreement between the data from this analysis and the LEPS data is very good, as the data points match within statistical errors. Combining this dataset with the LEPS dataset reveals that the sudden increase at about 1 900 MeV is followed by a sudden decrease at about 1 970 MeV of similar magnitude, revealing a peak centred around approximately 1 930 MeV. The DCS data measured by LEPS later rises again at 2 040 MeV, albeit not as strong as before. The comparison to the CLAS data must be done with reservation, as the angular ranges are slightly different. Up to a W of 1 892 MeV, the data points of this analysis lay within statistical errors of the CLAS data. The sudden jump of the DCS is not present in the CLAS dataset, the DCS stays at approximately $0.105\,\frac{\mu\text{b}}{\text{sr}}$ and agrees with the LEPS data after the sudden jump has declined again. This is attributed to the different angular ranges, which becomes apparent when considering the t dependence. For an interaction of two particles, where the initial state consists of particles 1 and 2 and the final state consists of particles 3 and 4, the Mandelstam variable t can be determined by using the four-momenta p_i as follows:

$$t = (p_1 - p_3)^2 = (p_2 - p_4)^2 \,.$$

The Mandelstam variable t corresponds to the square of the momentum transfer between the initial state particles. Figure 6.2 shows the same BGOOD data that were presented in figure 6.1, but converted to $\frac{d\sigma}{dt}$ in dependence of t. The same conversion was done for the LEPS and CLAS data for the W ranges shown in the inset of the figure. Additionally, LEPS data for the angular range $0.8 < \cos(\theta_{\text{CM}}) < 0.9$ are presented. The systematic uncertainties are shown at the bottom of the figure with the same colouring scheme as previously in figure 6.1. For the conversion to $\frac{d\sigma}{dt}$, expressions for t and dt are needed. These terms are assessed by generating $\gamma n \to K^+\Sigma^-$ events in simulation and determining the mean t for each bin of W. For a better repeatability of the conversion between $\frac{d\sigma}{d\Omega}$ and $\frac{d\sigma}{dt}$, the Fermi momentum of the initial state is neglected. For each bin of W, the t distribution is approximately uniformly distributed between the values t_a and t_b. The corresponding standard deviation is:

$$\sigma_t^{\text{Uniform}} = \frac{1}{\sqrt{12}} \cdot (t_b - t_a) = \frac{1}{\sqrt{12}} \cdot dt \,.$$

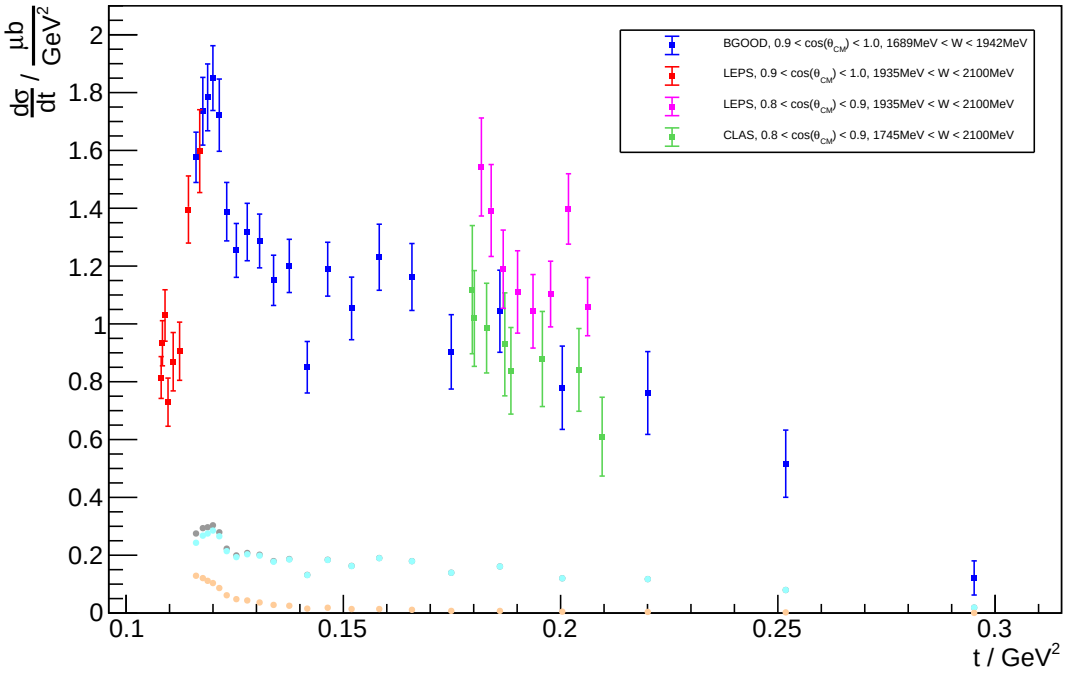

Figure 6.2: Conversion of the DCS data from figure 6.1 [51][50] to $\frac{d\sigma}{dt}$ in dependence of t. Note the W ranges in the inset. Additionally, LEPS data at $0.8 < \cos(\theta_{\mathrm{CM}}) < 0.9$ are presented in magenta. The systematic uncertainties are shown at the bottom using the same colouring scheme as in figure 6.1.

Here, $(t_b - t_a)$ can be taken as a measure for dt. Rearranging the terms leads to following expression:

$$dt = \sqrt{12} \cdot \sigma_t^{\mathrm{Uniform}} \, .$$

Knowing t and dt then allows for the conversion to $\frac{d\sigma}{dt}$ which is presented in figure 6.2. The figure has to be read from the right side to the left side: As W increases, t decreases. The peak that was seen around $W \approx 1\,930\,\mathrm{MeV}$ is then seen around $t \approx 0.119\,\mathrm{GeV}^2$. The figure provides a clear explanation for why the peak is not present in the CLAS dataset and only partially in the LEPS dataset: The low-t region around $0.119\,\mathrm{GeV}^2$ is not accessible by CLAS as their acceptance does not cover extreme forward angles and it is only partially accessible by LEPS as their acceptance covers extreme forward angles, but only starting from about $W = 1\,935\,\mathrm{MeV}$. This finding implies that a broad coverage over the low-t range is of importance, stressing the unique abilities of the BGOOD experiment. Crucially, low values of t correspond to low momentum transfers to the target system, which are the kinematics for which dynamically-generated molecular-like states are expected to be found. Molecular-like states are thought to be only loosely bound and could not be formed for large momentum transfers.

These results shall be compared to various theoretical predictions for dynamically-generated molecular-like structures.

As layed out in the introduction, the P_c^+ pentaquarks that were discovered at LHCb in 2015 [36] were pre-

dicted by a model developed by Ramos and Oset [38], which also predicts certain structures in the strange sector. The $N^*(2030)$ resonance is expected to magnify the interference of amplitudes driven by intermediate $K^*\Lambda$ and $K^*\Sigma$ channels. A destructive interference of these channels is thought to cause a cusp-like structure in the cross section of $\gamma p \to K^0\Sigma^+$, which matches with experimental observations [41]. In contrast, a constructive interference is expected to cause a resonant peak in the cross section of $\gamma n \to K^0\Sigma^0$ near the $K^*\Lambda$ and $K^*\Sigma$ thresholds. Due to limited statistics, DCS data of $K^0\Sigma^0$ acquired by BGOOD can neither exclude nor confirm a structure at about 2 040 MeV [42]. As the reaction channel $K^0\Sigma^0$ is the charge conjugate of the channel $K^+\Sigma^-$, measuring the DCS of $K^+\Sigma^-$ is especially important to shine light onto this situation. At the time of writing, there is no prediction of Ramos and Oset specifically for the DCS of $K^+\Sigma^-$, but only for the total cross section of $K^0\Sigma^0$. For these reasons, a comparison of the experimental data and their model should be done with reservation. Nevertheless, figure 6.3 shows the same $\gamma n \to K^+\Sigma^-$ data as figure 6.1 together with the prediction of Ramos and Oset for the total cross section of $\gamma n \to K^0\Sigma^0$ in black, in which the model parameters were fine-tuned using $K^0\Sigma^+$ data. The scale has been chosen arbitrarily to roughly match the experimental data. From left to right, the vertical lines describe the production thresholds of $K\Sigma(1385)$, $K\Lambda(1405)$, $K^*\Lambda$ and $K^*\Sigma$.

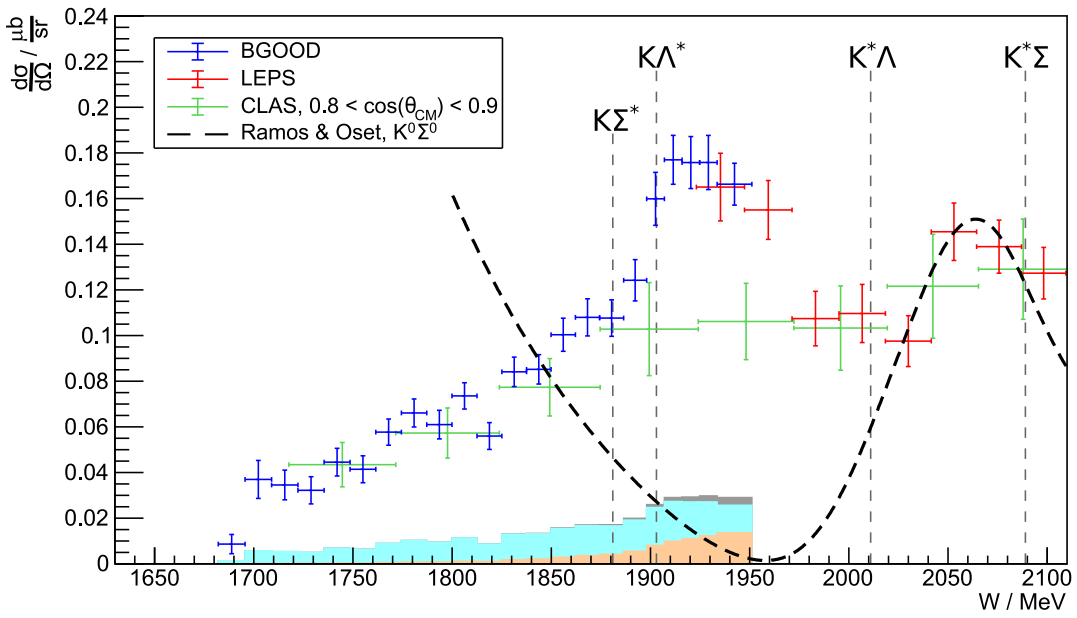

Figure 6.3: DCS as previously shown in figure 6.1 [51][50] together with the model of Ramos and Oset [38] for the total cross section of $\gamma n \to K^0\Sigma^0$ (black). The scale was chosen arbitrarily to roughly match the experimental data. From left to right, the vertical lines describe the production thresholds of $K\Sigma(1385)$, $K\Lambda(1405)$, $K^*\Lambda$ and $K^*\Sigma$.

Interestingly, when compared to the LEPS data, the theoretical prediction does indeed tend to agree with a sudden increase in the DCS just below the $K^*\Sigma$ threshold. The LEPS data jumps by approximately 0.04 $\frac{\mu b}{sr}$ at 2 040 MeV, which corresponds to an increase of about 40%. However, when compared to the data that was measured as a result of this thesis, it becomes apparent that the prediction is unable to describe the more prominent peak that can be seen around 1 930 MeV. The peak lies just above the production thresholds of $K\Sigma(1385)$ and $K\Lambda(1405)$, these possible coupled channels are not explicitly included in the calculations of

Ramos and Oset. A contamination of the signal with background reactions off the neutron has been excluded during the analysis, the contribution to the systematic uncertainty is of the order of 1%. The next section will discuss possible explanations of the peak beyond the prediction of Ramos and Oset.

In addition to the production thresholds of the aforementioned $K^{(*)}Y^{(*)}$ states, production thresholds of many more states can be found in proximity to the prominent peak centred around 1 930 MeV. The peak lies just below the production threshold of ϕn, which is located at 1 959 MeV as illustrated in figure 6.4 by a vertical line. Similarly to the dynamics suggested by Ramos and Oset, this could hint to a dynamically-generated ϕn bound state, leading to an increase in DCS below threshold and decrease above threshold, as there, ϕn can be produced freely. A test of this hypothesis would be to measure the DCS of $\gamma n \to \phi n$ and compare its value just above threshold to the extent of the drop in DCS of $\gamma n \to K^+\Sigma^-$. A match between these two values would hint towards dynamically-generated states driven by the ϕn system. At the time of writing, no such data on the neutron is available.

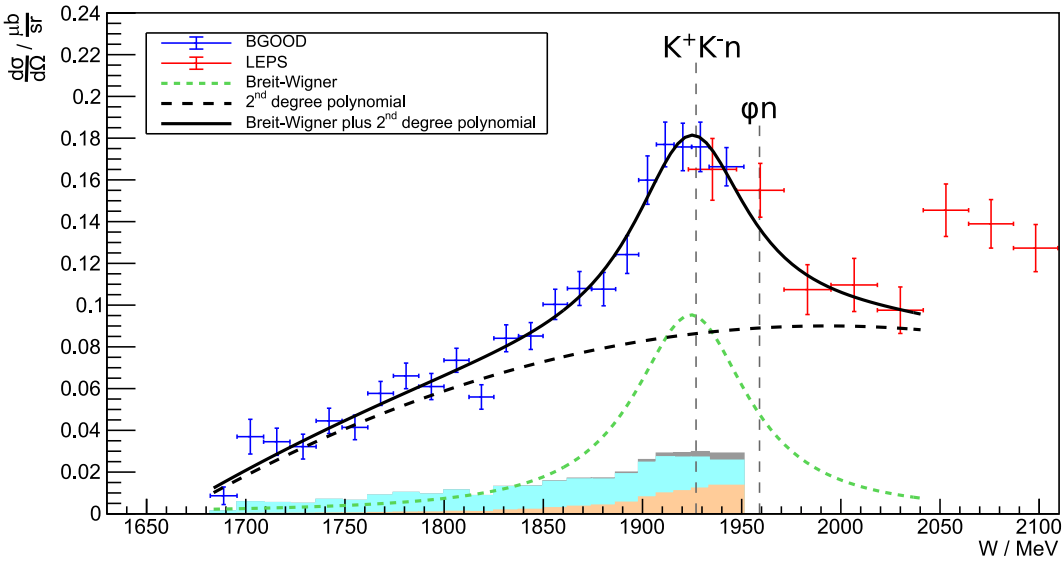

Figure 6.4: DCS as previously shown in figure 6.1 [51] together with a fit (solid black) composed of a Breit-Wigner distribution (green) and a second-degree polynomial (dashed black). Production thresholds of K^+K^-n as well as ϕn channels are described by vertical lines. The fitting range spans from threshold to $W = 2\,042$ MeV. The resulting Breit-Wigner mean is $M_{\text{Exp.}} = (1\,924.430 \pm 4.057)$ MeV with a width of $\Gamma_{\text{Exp.}} = (69.764 \pm 14.411)$ MeV, which appears consistent with the values predicted by Torres et al. [94] for a K^+K^-N bound state.

Gao et al. [95] advocated for the existence of a ϕN bound state denominated $N_{s\bar{s}}$ with quantum numbers $J^P = \frac{3}{2}^-$, which can be viewed as a hidden strange pentaquark state. The authors utilize a quark delocalization colour screening model to predict a mass of $M = 1\,949.597$ MeV and full decay width of $\Gamma = 4.094$ MeV, whereas just $\Gamma_{K\Sigma} = 0.060$ MeV is assigned to the $K\Sigma$ decay. This state would be located directly below the ϕn threshold. Due to the small decay width and given that a single W bin has a width of about 9 MeV, the present dataset can neither confirm nor exclude the existence of the $N_{s\bar{s}}$ state. Nevertheless, it is unlikely that the $N_{s\bar{s}}$ is responsible for the width of the entire peak centred around 1 930 MeV,

implying the need for further theoretical investigations.

Contrary to this pentaquark approach, predictions for a dynamically-generated molecular-like K^+K^-N bound state just below the K^+K^-N threshold exist [96][94][97]. The threshold is located at 1 927 MeV and also shown in figure 6.4. The bound state is expected to contain quantum numbers $I = \frac{1}{2}$ and $J^P = \frac{1}{2}^+$ and to contain a mixture of $a_0(980)N$ and $f_0(980)N$ components, where the $a_0(980)$ and $f_0(980)$ are thought to be molecular-like K^+K^- states themselves. The corresponding diagram for the process $\gamma n \to K^+\Sigma^-$ is presented in figure 6.5.

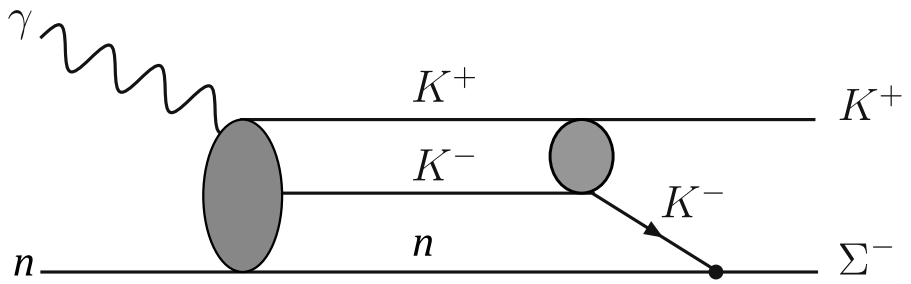

Figure 6.5: Diagram for the $\gamma n \to K^+\Sigma^-$ process via an intermediate K^+K^-n bound state. The $a_0(980)$ and $f_0(980)$ are thought to be molecular-like K^+K^- states themselves, illustrated by the right grey circle. Figure adapted for reactions off the neutron from reference [94].

The predicted mass and decay width vary between the individual models, Torres et al. [94] estimate a mass of $M_{\text{Theo.}} = 1\,924$ MeV with a width of about $\Gamma_{\text{Theo.}} = 60$ MeV based on measurements of $\gamma p \to K^+\Lambda$. Figure 6.4 shows the $K^+\Sigma^-$ data together with a fit, where the fitting range spans from threshold to 2 042 MeV. The fit is composed of a Breit-Wigner distribution shown in green and a second-degree polynomial shown as a dashed black line, where none of the fitting parameters have been restricted, letting the Breit-Wigner move freely. The final fit result is shown as the solid black line and matches well with the experimental data, mostly lying withing the statistical errors. The resulting Breit-Wigner mean is $M_{\text{Exp.}} = (1\,924.430 \pm 4.057)$ MeV with a width of $\Gamma_{\text{Exp.}} = (69.764 \pm 14.411)$ MeV, which appears consistent with the values predicted by Torres et al. [94]. Note that the authors of reference [94] are focusing on decays where the involved nucleon is a proton and they state that a coupling to $K\Lambda$ appears more likely than to $K\Sigma$, implying that adjustments may apply to the charge-conjugate counterpart $K^+\Sigma^-$. Unfortunately, no DCS data of $\gamma n \to K^+K^-n$ is available for comparison.

The most striking feature of the data is the peak at 1 924 MeV and more conventional models fail to describe it. Figure 6.6 shows the same experimental data as before now in comparison with theoretical predictions based on effective Lagrangian approaches in the tree-level Born approximation by Wei et al. [46][98]. Their model includes s-channel N, N^*, Δ, and Δ^* contributions, t-channel K and K^* exchanges and the u-channel Σ exchange. The model struggles to produce a fit that satisfies both the complementary $\gamma n \to K^0\Sigma^0$ dataset provided by the A2 Collaboration [47] and the one of the BGOOD collaboration [42] simultaneously, while being in good agreement with previous $\gamma n \to K^+\Sigma^-$ data. In addition to all previously available data of $K^+\Sigma^-$, fit A was based on data of $K^0\Sigma^0$ of the A2 Collaboration and fit B on data of $K^0\Sigma^0$ of the BGOOD collaboration. As apparent from figure 6.6, fit B has a better agreement with the newly produced $K^+\Sigma^-$ data. Up until $W = 1\,843$ MeV, the predicted DCS roughly lies within the statistical errors. At $W = 1\,980$ MeV,

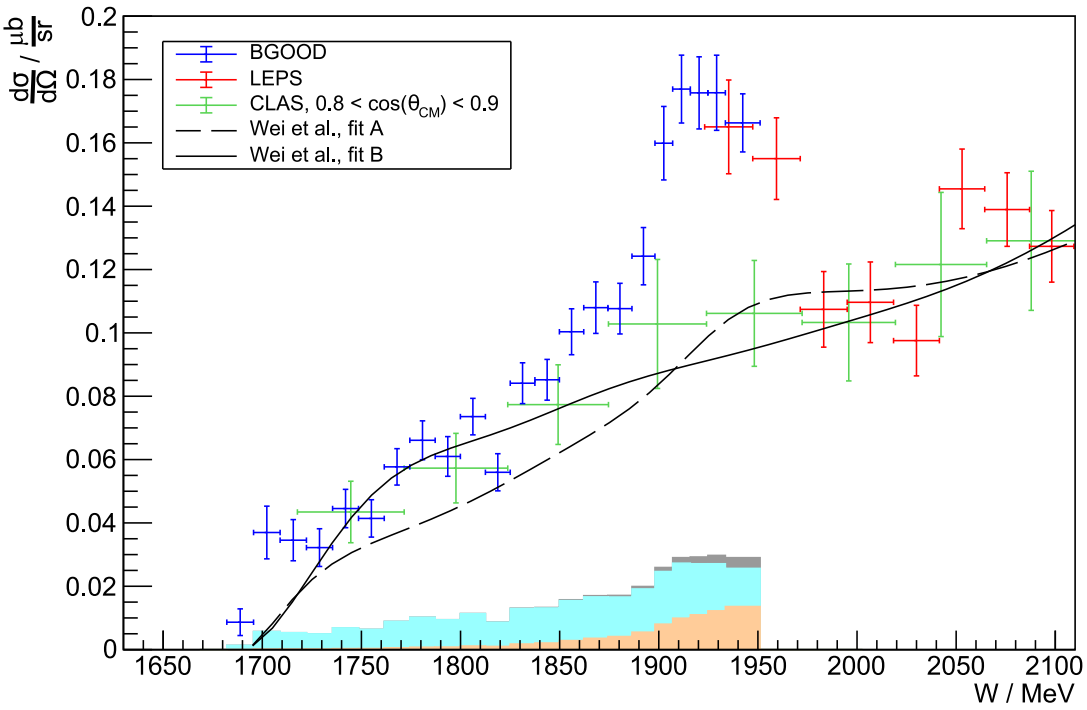

Figure 6.6: DCS as previously shown in figure 6.1 [51][50] together with theoretical predictions based on effective Lagrangian approaches by Wei et al. [46][98]. Data and theory tend to agree below $W = 1\,843\,\text{MeV}$ and above $W = 1\,980\,\text{MeV}$, but the peak around at $W = 1\,924\,\text{MeV}$ can not adequatly described even under consideration of the systematic uncertainties.

it tends to agree with the LEPS data. However, the most striking feature of this analysis, namely the sudden jump at about $W = 1\,900\,\text{MeV}$ which reveals a peak around $W = 1\,924\,\text{MeV}$, can not be adequately described by the model even under consideration of the systematic uncertainties.

Figure 6.7 shows another theoretical prediction based on an effective Lagrangian in an isobar model by Bydžovský et al. [48][99]. Contributions from a wide range of N, Δ and Σ s-channel resonances are considered together with K and K^* t-channel terms. Fit M was created by applying a conventional χ^2 minimization technique to the previously available data, while fit L uses a more elaborate 'least absolute shrinkage and selection operator' method, abbreviated as 'LASSO'. Fit L gives a better description of the data. From $W = 1\,793\,\text{MeV}$ to $W = 1\,892\,\text{MeV}$, the prediction lies within the statistical errors of the BGOOD data and then agrees later at $W = 1\,980\,\text{MeV}$ with the LEPS data. Similar to the model of Wei et al. [46][98], the peak around $W = 1\,924\,\text{MeV}$ is not described by the model.

The contribution of FSI to the final DCS has been estimated to be approximately 7% based on theoretical calculations by Salam and Arenhövel [89]. It shall be emphasized that the contribution could potentially be higher, as the theoretical FSI model was developed under simplified assumptions and relies partly on fits to experimental data, which, at the time of publication of the corresponding paper, was even more scarce than

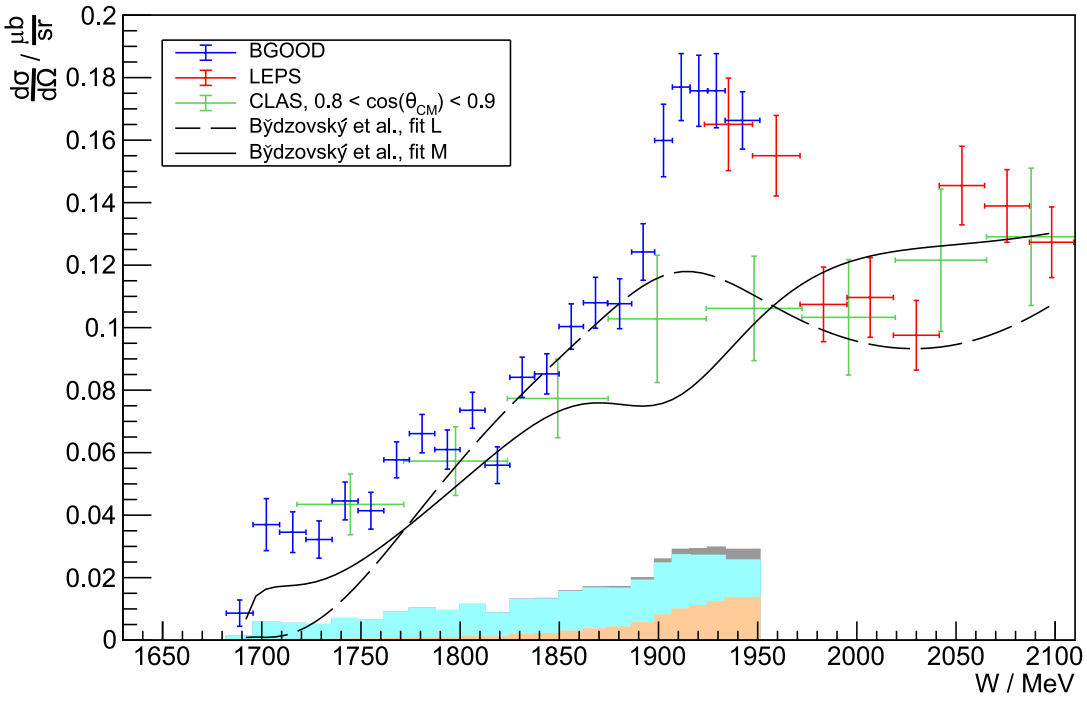

Figure 6.7: DCS as previously shown in figure 6.1 [51][50] together with theoretical predictions based on effective Lagrangian approaches by Bydžovský et al. [48][99]. Data and theory tend to agree between $W = 1\,793$ MeV and $W = 1\,892$ MeV and above $W = 1\,980$ MeV, but the peak around $W = 1\,924$ MeV is not adequatly described.

today. The contribution of FSI are not included in the systematic uncertainties shown at the bottom of the figures.

In summary of the preceding discussion, the following can be concluded:

The effective Lagrangian approaches of both Wei et al. [46][98] and Bydžovský et al. [48][99] fail to describe the prominent peak at 1 924 MeV and furthermore the secondary increase in DCS at 2 040 MeV. The prominent peak lies just below the ϕn threshold, below which Gao et al. [95] advocated for the existence of a ϕN bound state denominated $N_{s\bar{s}}$, which can be viewed as a hidden strange pentaquark. A predicted partial decay width of $\Gamma_{K\Sigma} = 0.060$ MeV for the $K\Sigma$ channels is too narrow to account for the width of the observed peak and is below the accessible W resolution. Fitting a Breit-Wigner along with a second-degree polynomial to the dataset shows a good agreement with a K^+K^-N bound state around 1 924 MeV as predicted by Torres et al. [96][94] and others [97]. The secondary increase in DCS at 2 040 MeV is shown by the LEPS dataset [51] and to some extent by the CLAS dataset [50]. A promising interpretation of this jump is in the context of the theoretical model of Ramos and Oset [38], in which the $N^*(2030)$ resonance is expected to magnify the constructive interference of amplitudes driven by intermediate $K^*\Lambda$ and $K^*\Sigma$ channels, causing a resonant peak in the total cross section of $\gamma n \to K^0\Sigma^0$ at around 2 040 MeV. This would be in analogy to the P_c^+ pentaquarks that were discovered at LHCb in 2015 [36].

CHAPTER 7

Summary and Outlook

The idea of hadrons being composed of more than three quarks is experiencing a renaissance within the last decade, as in 2015, LHCb discovered the first unambiguous pentaquark denominated P_c^+ [36] and could later establish the pentaquark states $P_c(4312)^+$, $P_c(4440)^+$ and $P_c(4457)^+$ [36][37]. These pentaquarks are located close to production thresholds of $\Sigma_c^{(*)}\bar{D}^{(*)}$ states. If the formation of pentaquarks is not a unique feature of the heavy quark sector, but a universal feature of the strong interaction, similar structures might exist in the strange sector. Naturally, the exchange of the c quark of the $\Sigma_c^{(*)}\bar{D}^{(*)}$ states with a s quark would lead to $\Sigma^{(*)}K^{(*)}$ states. Indeed, the same model that predicted the pentaquarks discovered by LHCb also predicts certain structures in the strange sector [38]. One of such states is the $N^*(2030)$ resonance, which is thought to be a dynamically-generated $K^*\Sigma$ state. For the reaction $\gamma n \to K^0\Sigma^0$, it is expected to magnify the constructive interference of amplitudes driven by intermediate $K^*\Lambda$ and $K^*\Sigma$ channels, and thus giving rise to a resonant peak in the spectrum just below the $K^*\Sigma$ threshold. Data for the differential cross section of $\gamma n \to K^0\Sigma^0$ has previously been measured at BGOOD but remained inconclusive regarding a structure at $W = 2\,040\,\mathrm{MeV}$ due to limited statistical precision [42]. Similar structures might be expected in the charge-conjugate channel $\gamma n \to K^+\Sigma^-$, which provides motivation for the presented measurement.

Hadrons being composed of more than three quarks could manifest in compactly bound pentaquark formations or in relatively loosely bound molecular-like states of colourless subsystems. Due to the small binding energy, the production of the latter generally requires low momentum transfers. These can be realized in low-t processes. This implies that for $\gamma n \to K^+\Sigma^-$, the K^+ would take most of the momentum and go to forward angles. Due to its combination of a large-aperture forward spectrometer complemented by a central BGO calorimeter with almost 4π angular acceptance, the BGOOD experiment is ideally suited for such investigations.

The goal of this thesis was to measure the differential cross section of $\gamma n \to K^+\Sigma^-$ in an angular range of $\cos(\theta_{\mathrm{CM}}) > 0.9$. First, a measurement of the normalized K^+Y yield was performed utilizing a deuterium target. The contribution to the normalized K^+Y yield stemming from background reactions off the bound proton was determined by performing the same analysis on a hydrogen target and correcting for the Fermi motion. For the yield extraction of the two datasets, different selection criteria were applied before performing a maximum likelihood fit to the time of flight mass spectrum in order to get a clean separation between K^+ and π^+. The K^+ peak was modeled using the Geant4 simulation, while the π^+ peak was determined by measuring the π^- peak, which has the same shape but lacks any K^- contribution. After subtraction of the background stemming from the proton, dividing by the reconstruction efficiency and the solid angle element lead to the desired differential cross section. The contribution of background reactions off the neutron to the

systematic uncertainty was modeled by comparing the reconstruction efficiency of $K^+\Sigma^-$ to the ones of the background reactions and making the reasonable assumption that the differential cross sections are approximately of the same magnitude. The contribution of potential final state interaction effects to the differential cross section was estimated to be of the order of roughly 7% based on theoretical calculations, albeit the calculations were unavoidably based on scarce data.

The final differential cross section was measured at centre-of-mass energies ranging from threshold, which is located at $W = 1\,691$ MeV, up to $W = 1\,942$ MeV. Practically the entire kinematic range covered by the performed analysis has never been explored before. The W resolution is unprecedented and approximately twice as good as those achieved by LEPS [51] and CLAS [50]. For similar bins of W, the statistical error of the differential cross section is about half the size of the one of CLAS and two thirds of the one of LEPS. The most striking feature of the obtained data is a sudden jump of the differential cross section in-between 1 892 MeV and 1 911 MeV. Combining the acquired data with a dataset of LEPS [51] reveals that this sudden jump is actually a peak.

The fact that the prominent peak is not seen in the CLAS dataset and only partially in the LEPS dataset can likely be understood by the t dependency: The peak is located around a Mandelstam t of approximately $0.119\,\mathrm{GeV}^2$, which is a low-t value that is not accessed in the CLAS analysis and only partially in the LEPS analysis. Not only does this stress the importance of mapping out the low-t region and emphasize the unique abilities of the BGOOD experiment, it is also the t region which is of uttermost importance for the formation of dynamically-generated molecular-like states, as they are loosely bound and thus require low momentum transfers, which correspond to low values of t.

The acquired data in combination with LEPS data can be described well by a fit consisting of a Breit-Wigner distribution and a second-degree polynomial. The fit lies mostly within the statistical errors. The Breit-Wigner has a resulting mean of $M = (1\,924.430 \pm 4.057)$ MeV with a width of $\Gamma = (69.764 \pm 14.411)$ MeV, which appears consistent with theoretical predictons of a K^+K^-N bound state located around 1 924 MeV [96][94][97]. The secondary increase of the differential cross section around 2 040 MeV which can be seen in the LEPS dataset actually coincides with the position of the constructive interference of intermediate $K^*\Lambda$ and $K^*\Sigma$ channels just below the $K^*\Sigma$ threshold as predicted for the total cross section of $\gamma n \to K^0\Sigma^0$ by the same theoretical model that predicted the P_c^+ pentaquarks [38].

In order to formulate a firm argument in favour of or against the interpretation of both peaks as dynamically-generated molecular-like states in the strange sector, both the experimental field and the theoretical field need to go hand in hand: On the experimental side, more differential cross section data are needed at extreme forward angles, especially around the W regions of interest around 1 924 MeV and 2 040 MeV. Mapping out the low-t region might be a promising approach to gain new insights into dynamically-generated molecular-like states. On the theoretical side, providing predictions specifically for the differential cross section of $\gamma n \to K^+\Sigma^-$ at $\cos(\theta_{\mathrm{CM}}) > 0.9$ as well as using the newly acquired data to fine-tune the model parameters would be valuable.

For the future, an improvement of the performed analysis could be achieved by determining the exact neutron detection efficiency of the BGO calorimeter in both real data and simulation, which could lower the estimated systematic uncertainty of the chosen charge signature selection. A natural first step would be to replicate the GRAAL analysis [87] of the neutron detection efficiency for the current hardware setup of BGOOD. Furthermore, implementing a calibration of the barrel might improve the π identification in the central detector.

Bibliography

[1] E. Fermi and C. N. Yang, *Are Mesons Elementary Particles?*, Phys. Rev. **76** (12 1949) 1739, URL: https://link.aps.org/doi/10.1103/PhysRev.76.1739 (cit. on p. 1).

[2] S. Sakata, *On a Composite Model for the New Particles**, Progress of Theoretical Physics **16** (1956) 686, URL: https://doi.org/10.1143/PTP.16.686 (cit. on p. 1).

[3] C. Levinson, H. Lipkin and S. Meshkov, *Unitary symmetry and nucleon-antinucleon annihilation*, Physics Letters **1** (1962) 307, URL: https://www.sciencedirect.com/science/article/pii/0031916362904043 (cit. on p. 1).

[4] M. Gell-Mann, *The Eightfold Way: A Theory of Strong Interaction Symmetry*, Caltech Synchrotron Laboratory Report **CTSL-20, TID-12608** (1961), URL: https://www.osti.gov/servlets/purl/4008239/ (cit. on p. 1).

[5] S. Okubo, *Note on Unitary Symmetry in Strong Interactions*, Progress of Theoretical Physics **27** (1962) 949, URL: https://doi.org/10.1143/PTP.27.949 (cit. on p. 1).

[6] S. Okubo, *Note on Unitary Symmetry in Strong Interaction. II: Excited States of Baryons*, Progress of Theoretical Physics **28** (1962) 24, URL: https://doi.org/10.1143/PTP.28.24 (cit. on p. 1).

[7] V. E. Barnes et al., *Observation of a Hyperon with Strangeness Minus Three*, Phys. Rev. Lett. **12** (8 1964) 204, URL: https://link.aps.org/doi/10.1103/PhysRevLett.12.204 (cit. on p. 1).

[8] M. Gell-Mann, *A schematic model of baryons and mesons*, Physics Letters **8** (1964) 214, URL: https://www.sciencedirect.com/science/article/pii/S0031916364920013 (cit. on pp. 1, 5).

[9] G. Zweig, *An SU(3) model for strong interaction symmetry and its breaking. Version 2*, Developments in the Quark Theory of Hadrons **1** (1964) 22, URL: https://cds.cern.ch/record/570209 (cit. on p. 1).

[10] Nobel Prize Outreach AB 2025, *The Nobel Prize in Physics 1969*, URL: https://www.nobelprize.org/prizes/physics/1969/summary/ (visited on 12/01/2025) (cit. on p. 1).

[11] H. Fritzsch and M. Gell-Mann, *Light cone current algebra*,
International conference on duality and symmetry in hadron physics (1971) 317,
URL: https://arxiv.org/abs/hep-ph/0301127 (cit. on p. 1).

[12] M. Y. Han and Y. Nambu, *Three-Triplet Model with Double* SU(3) *Symmetry*,
Phys. Rev. **139** (4B 1965) B1006,
URL: https://link.aps.org/doi/10.1103/PhysRev.139.B1006 (cit. on p. 1).

[13] K. Niu, E. Mikumo and Y. Maeda, *A Possible Decay in Flight of a New Type Particle*,
Progress of Theoretical Physics **46** (1971) 1644,
URL: https://doi.org/10.1143/PTP.46.1644 (cit. on p. 1).

[14] J. J. Aubert et al., *Experimental Observation of a Heavy Particle J*,
Phys. Rev. Lett. **33** (23 1974) 1404,
URL: https://link.aps.org/doi/10.1103/PhysRevLett.33.1404
(cit. on p. 1).

[15] J. E. Augustin et al., *Discovery of a Narrow Resonance in e^+e^- Annihilation*,
Phys. Rev. Lett. **33** (23 1974) 1406,
URL: https://link.aps.org/doi/10.1103/PhysRevLett.33.1406
(cit. on p. 1).

[16] S. W. Herb et al.,
Observation of a Dimuon Resonance at 9.5 GeV in 400-GeV Proton-Nucleus Collisions,
Phys. Rev. Lett. **39** (5 1977) 252,
URL: https://link.aps.org/doi/10.1103/PhysRevLett.39.252
(cit. on p. 1).

[17] F. Abe et al.,
Observation of Top Quark Production in $\overline{p}p$ Collisions with the Collider Detector at Fermilab,
Phys. Rev. Lett. **74** (14 1995) 2626,
URL: https://link.aps.org/doi/10.1103/PhysRevLett.74.2626
(cit. on p. 1).

[18] H. D. Politzer, *Reliable Perturbative Results for Strong Interactions?*,
Phys. Rev. Lett. **30** (26 1973) 1346,
URL: https://link.aps.org/doi/10.1103/PhysRevLett.30.1346
(cit. on p. 1).

[19] D. J. Gross and F. Wilczek, *Ultraviolet Behavior of Non-Abelian Gauge Theories*,
Phys. Rev. Lett. **30** (26 1973) 1343,
URL: https://link.aps.org/doi/10.1103/PhysRevLett.30.1343
(cit. on p. 1).

[20] D. E. Soper, *Basics of QCD perturbation theory*, Flavor Physics for the Millennium (2000) 267,
URL: https://arxiv.org/abs/hep-ph/0011256 (cit. on p. 3).

[21] G. Sterman et al., *Handbook of perturbative QCD*, Rev. Mod. Phys. **67** (1 1995) 157,
URL: https://link.aps.org/doi/10.1103/RevModPhys.67.157 (cit. on p. 3).

[22] H. Schmieden, *First Results from the BGO-OD Experiment at ELSA*,
Few-Body Systems **59** (6 2018) 135,
URL: https://doi.org/10.1007/s00601-018-1453-0 (cit. on pp. 3–5).

[23] U. Löring, B. Metsch and H. Petry, *The light-baryon spectrum in a relativistic quark model with instanton-induced quark forces: The non-strange-baryon spectrum and ground states*, The European Physical Journal A **10** (2001) 395, URL: http://dx.doi.org/10.1007/s100500170105 (cit. on pp. 3, 4).

[24] U. Löring, B. Metsch and H. Petry, *The light-baryon spectrum in a relativistic quark model with instanton-induced quark forces: The strange-baryon spectrum*, The European Physical Journal A **10** (2001) 447, URL: http://dx.doi.org/10.1007/s100500170106 (cit. on p. 4).

[25] E. Klempt and J.-M. Richard, *Baryon spectroscopy*, Rev. Mod. Phys. **82** (2 2010) 1095, URL: https://link.aps.org/doi/10.1103/RevModPhys.82.1095 (cit. on p. 4).

[26] K. G. Wilson, *Confinement of quarks*, Phys. Rev. D **10** (8 1974) 2445, URL: https://link.aps.org/doi/10.1103/PhysRevD.10.2445 (cit. on p. 4).

[27] R. L. Workman et al., *Review of Particle Physics*, PTEP **2022** (2022) 083C01, URL: https://academic.oup.com/ptep/article/2022/8/083C01/6651666 (cit. on pp. 5, 50, 51, 55, 59, 61).

[28] R. J. Jaffe, *Multiquark hadrons. I. Phenomenology of $Q^2\overline{Q}^2$ mesons*, Phys. Rev. D **15** (1 1977) 267, URL: https://link.aps.org/doi/10.1103/PhysRevD.15.267 (cit. on p. 5).

[29] A. Manohar and H. Georgi, *Chiral quarks and the non-relativistic quark model*, Nuclear Physics B **234** (1984) 189, URL: https://www.sciencedirect.com/science/article/pii/0550321384902311 (cit. on p. 5).

[30] H. J. Lipkin, *New possibilities for exotic hadrons — anticharmed strange baryons*, Physics Letters B **195** (1987) 484, URL: https://www.sciencedirect.com/science/article/pii/0370269387900554 (cit. on p. 5).

[31] M. H. Alston et al., *Study of Resonances of the $\Sigma - \pi$ System*, Phys. Rev. Lett. **6** (12 1961) 698, URL: https://link.aps.org/doi/10.1103/PhysRevLett.6.698 (cit. on p. 5).

[32] K. Nakamura and Particle Data Group, *Review of Particle Physics*, Journal of Physics G: Nuclear and Particle Physics **37** (2010) 075021, URL: https://dx.doi.org/10.1088/0954-3899/37/7A/075021 (cit. on p. 5).

[33] R. H. Dalitz and S. F. Tuan, *Possible Resonant State in Pion-Hyperon Scattering*, Phys. Rev. Lett. **2** (10 1959) 425, URL: https://link.aps.org/doi/10.1103/PhysRevLett.2.425 (cit. on p. 5).

[34] C. Patrignani, *Review of Particle Physics*, Chinese Physics C **40** (2016) 100001, URL: https://dx.doi.org/10.1088/1674-1137/40/10/100001 (cit. on p. 5).

[35] T. Nakano et al.,
Evidence for a Narrow $S = +1$ Baryon Resonance in Photoproduction from the Neutron,
Phys. Rev. Lett. **91** (1 2003) 012002,
URL: https://link.aps.org/doi/10.1103/PhysRevLett.91.012002
(cit. on p. 5).

[36] R. Aaij et al.,
Observation of $J/\psi p$ Resonances Consistent with Pentaquark States in $\Lambda_b^0 \to J/\psi K^- p$ Decays,
Phys. Rev. Lett. **115** (7 2015) 072001,
URL: https://link.aps.org/doi/10.1103/PhysRevLett.115.072001
(cit. on pp. 5, 6, 87, 92, 93).

[37] R. Aaij et al., *Observation of a Narrow Pentaquark State, $P_c(4312)^+$, and of the Two-Peak Structure of the $P_c(4450)^+$*, Phys. Rev. Lett. **122** (22 2019) 222001,
URL: https://link.aps.org/doi/10.1103/PhysRevLett.122.222001
(cit. on pp. 5, 6, 93).

[38] A. Ramos and E. Oset, *The role of vector-baryon channels and resonances in the $\gamma p \to K^0 \Sigma^+$ and $\gamma n \to K^0 \Sigma^0$ reactions near the $K^* \Lambda$ threshold*, Physics Letters B **727** (2013) 287,
URL: https://www.sciencedirect.com/science/article/pii/S0370269313008058
(cit. on pp. 5, 7, 88, 92–94).

[39] M.-L. Du et al.,
Interpretation of the LHCb P_c States as Hadronic Molecules and Hints of a Narrow $P_c(4380)$,
Phys. Rev. Lett. **124** (7 2020) 072001,
URL: https://link.aps.org/doi/10.1103/PhysRevLett.124.072001
(cit. on p. 6).

[40] T. Jude et al., *The BGOOD experiment at ELSA, exotic structures in the light quark sector?*,
EPJ Web Conf. **291** (2024) 01004,
URL: https://doi.org/10.1051/epjconf/202429101004 (cit. on p. 6).

[41] R. Ewald et al.,
Anomaly in the $K_S^0 \Sigma^+$ photoproduction cross section off the proton at the K^* threshold,
Physics Letters B **713** (2012) 180, URL: https://www.sciencedirect.com/science/article/pii/S0370269312006259
(cit. on pp. 6, 7, 88).

[42] K. Kohl et al., *Measurement of the $\gamma n \to K^0 \Sigma^0$ differential cross section over the K^* threshold*, Eur. Phys. J. A **59** (2023) 254, URL: https://link.springer.com/article/10.1140/epja/s10050-023-01133-1
(cit. on pp. 7, 8, 88, 90, 93).

[43] G. Scheluchin et al., *Photoproduction of $K^+ \Lambda(1405) \to K^+ \pi^0 \Sigma^0$ extending to forward angles and low momentum transfer*, Physics Letters B **833** (2022) 137375, URL: https://www.sciencedirect.com/science/article/pii/S0370269322005093
(cit. on pp. 7, 9).

[44] E. Wang, J.-J. Xie, W.-H. Liang, F.-K. Guo and E. Oset,
Role of a triangle singularity in the $\gamma p \to K^+ \Lambda(1405)$ reaction, Phys. Rev. C **95** (1 2017) 015205,
URL: https://link.aps.org/doi/10.1103/PhysRevC.95.015205
(cit. on p. 9).

[45] T. Jude et al., *Observation of a cusp-like structure in the $\gamma p \to K^+ \Sigma^0$ cross section at forward angles and low momentum transfer*, Physics Letters B **820** (2021) 136559, URL: https://www.sciencedirect.com/science/article/pii/S0370269321004998
(cit. on pp. 7, 9).

[46] N.-C. Wei, A.-C. Wang and F. Huang,
Combined analysis of the $\gamma n \to K^0 \Sigma^0$ and $\gamma n \to K^+ \Sigma^-$ reactions,
Phys. Rev. D **107** (11 2023) 114018,
URL: https://link.aps.org/doi/10.1103/PhysRevD.107.114018
(cit. on pp. 7, 90–92).

[47] C. S. Akondi et al., *Experimental study of the $\gamma p \to K^0 \Sigma^+$, $\gamma n \to K^0 \Lambda$, and $\gamma n \to K^0 \Sigma^0$ reactions at the Mainz Microtron*, Eur. Phys. J. A **55** (2019) 202, URL:
https://link.springer.com/article/10.1140/epja/i2019-12924-x
(cit. on pp. 7, 90).

[48] P. Byd žovský, A. Cieplý, D. Petrellis, D. Skoupil and N. Zachariou,
Model selection for $K^+ \Sigma^-$ photoproduction within an isobar model,
Phys. Rev. C **104** (6 2021) 065202,
URL: https://link.aps.org/doi/10.1103/PhysRevC.104.065202
(cit. on pp. 7, 91, 92).

[49] F. Lee, T. Mart, C. Bennhold, H. Haberzettl and L. Wright,
Quasifree kaon photoproduction on nuclei, Nuclear Physics A **695** (2001) 237, URL: https://www.sciencedirect.com/science/article/pii/S0375947401010983
(cit. on p. 7).

[50] S. A. Pereira et al., *Differential cross section of $\gamma n \to K^+ \Sigma^-$ on bound neutrons with incident photons from 1.1 to 3.6 GeV*, Physics Letters B **688** (2010) 289, URL: https://www.sciencedirect.com/science/article/pii/S0370269310004788
(cit. on pp. 8, 85, 87, 88, 91, 92, 94).

[51] H. Kohri et al., *Differential Cross Section and Photon-Beam Asymmetry for the $\vec{\gamma}\, n \to K^+ \Sigma^-$ Reaction at $E_\gamma = 1.5 - 2.4$ GeV*, Phys. Rev. Lett. **97** (8 2006) 082003,
URL: https://link.aps.org/doi/10.1103/PhysRevLett.97.082003
(cit. on pp. 8, 85, 87–89, 91, 92, 94).

[52] S. Alef et al., *The BGOOD experimental setup at ELSA*, Eur. Phys. J. A **56** (2020) 104,
URL: https://link.springer.com/article/10.1140/epja/s10050-020-00107-x (cit. on pp. 11–20, 30).

[53] W. Hillert, *The Bonn electron stretcher accelerator ELSA: Past and future*,
Eur. Phys. J. A **28S1** (2006) 139,
URL: https://doi.org/10.1140/epja/i2006-09-015-4 (cit. on pp. 11, 12).

[54] ELSA, *ELSA Overview*,
URL: https://www.pi.uni-bonn.de/elsa/medien/elsa-2022-05_20240828_en-1.png/images/image/leadimagesize (visited on 12/01/2025) (cit. on p. 12).

[55] ELSA, *Technical description of the accelerator*,
URL: https://www.pi.uni-bonn.de/elsa/en/accelerator/technical-description-of-accelerator (visited on 12/01/2025) (cit. on p. 12).

[56] A. Bella, *Linearly polarised photon beams at the BGO-OD experiment at ELSA*,
PhD thesis: Rheinische Friedrich-Wilhelms-Universität Bonn, 2016,
URL: https://hdl.handle.net/20.500.11811/6897 (cit. on p. 15).

[57] S. Alef, *Scintillating fibre detector and kinematic fitting for the BGO-OD experiment*,
MA thesis: Universität Bonn, 2015,
URL: https://www.pi.uni-bonn.de/schmieden/medien/medien-ergebnisse/masterarbeit_stefan-alef.pdf (cit. on p. 15).

[58] B.-E. Reitz,
Coherent bremsstrahlung with the scintillating fiber detector of the BGO-OD tagging system,
MA thesis: Universität Bonn, 2015,
URL: https://www.pi.uni-bonn.de/schmieden/medien/medien-ergebnisse/masterarbeit_bjoern-ericreitz.pdf (cit. on p. 15).

[59] F. Messi, *The Tagging System of the BGO-OD experiment*,
PhD thesis: Rheinische Friedrich-Wilhelms-Universität Bonn, 2015,
URL: https://hdl.handle.net/20.500.11811/6480 (cit. on pp. 16, 17).

[60] G. Scheluchin, *Meson photoproduction on the proton using the BGO-OD detector complemented by a new Scintillating Ring (SciRi)*, MA thesis: Universität Bonn, 2015,
URL: https://www.pi.uni-bonn.de/schmieden/medien/medien-ergebnisse/masterarbeit_georgscheluchin.pdf (cit. on p. 17).

[61] G. Scheluchin, *$\Lambda(1405)$ photoproduction with the BGO-OD experiment*,
PhD thesis: Rheinische Friedrich-Wilhelms-Universität Bonn, 2020,
URL: https://hdl.handle.net/20.500.11811/8373 (cit. on pp. 18, 27).

[62] S. Böse,
Aufbau und Test eines Szintillationsfaser-Detektors für das neue Vorwärtsspektrometer an ELSA,
PhD thesis: Rheinische Friedrich-Wilhelms-Universität Bonn, 2016,
URL: https://hdl.handle.net/20.500.11811/6728 (cit. on p. 18).

[63] T. Frese, *In situ field measurement of the Open Dipole magnet at the BGO-OD experiment*,
MA thesis: Universität Bonn, 2012,
URL: https://www.pi.uni-bonn.de/schmieden/medien/medien-ergebnisse/diplomarbeit_torstenfrese.pdf (cit. on p. 19).

[64] T. Schwan, *Test und Inbetriebnahme der Driftkammern für das BGO-OD-Spektrometer*,
MA thesis: Universität Bonn, 2010,
URL: https://www.pi.uni-bonn.de/schmieden/medien/medien-ergebnisse/diplomarbeit_timoschwan.pdf (cit. on p. 19).

[65] P. Meiß, *The Time Of Flight Spectrometer of the BGO-OD Experiment*, MA thesis: Universität Bonn, 2013, URL: https://www.pi.uni-bonn.de/schmieden/medien/medien-ergebnisse/diplomarbeit_petermeiss.pdf (cit. on p. 19).

[66] K. Kohl, *Absolute Photon Flux Measurement at the BGO-OD-Experiment*, MA thesis: Universität Bonn, 2016, URL: https://www.pi.uni-bonn.de/schmieden/medien/medien-ergebnisse/masterarbeit_katrinkohl.pdf (cit. on p. 19).

[67] D. Hammann, *The data acquisition for the BGO-OD experiment*, PhD thesis: Rheinische Friedrich-Wilhelms-Universität Bonn, 2016, URL: https://hdl.handle.net/20.500.11811/6838 (cit. on pp. 20, 21).

[68] O. Freyermuth, *Studies of ω Photoproduction off Proton at the BGO-OD Experiment*, PhD thesis: Rheinische Friedrich-Wilhelms-Universität Bonn, 2017, URL: https://hdl.handle.net/20.500.11811/7263 (cit. on pp. 20–23, 25).

[69] ROOT Team, *ROOT Manual*, URL: https://root.cern/manual/ (visited on 13/01/2025) (cit. on pp. 21, 63).

[70] ROOT Team, *RooFit Manual*, URL: https://root.cern/manual/roofit/ (visited on 31/01/2025) (cit. on pp. 21, 63).

[71] C. Schmidt, A. Suele and U. T. et al., *Extended Pluggable Objectoriented ROOT(ified) Analysis) for the CBELSA/TAPS experiment*, 4233 (cit. on p. 21).

[72] Geant4 Collaboration, *Geant4 Documentation*, URL: https://geant4.web.cern.ch/docs/ (visited on 13/01/2025) (cit. on p. 22).

[73] Bonn-Gatchina Partial Wave Analysis, *Single meson photoproduction observables off proton*, URL: https://pwa.hiskp.uni-bonn.de/BG2019_obs_int.htm (visited on 13/01/2025) (cit. on pp. 34, 35).

[74] The CB-ELSA Collaboration et al., *Photoproduction of η-mesons off protons*, Eur. Phys. J. A **33** (2007) 133, URL: https://doi.org/10.1140/epja/i2007-10455-9 (cit. on p. 34).

[75] V. Crede et al., *Photoproduction of η and η' mesons off protons*, Phys. Rev. C **80** (5 2009) 055202, URL: https://link.aps.org/doi/10.1103/PhysRevC.80.055202 (cit. on p. 34).

[76] E. F. McNicoll et al., *Experimental study of the $\gamma p \to \eta p$ reaction with the Crystal Ball detector at the Mainz Microtron (MAMI-C)*, Phys. Rev. C **82** (3 2010) 035208, URL: https://link.aps.org/doi/10.1103/PhysRevC.82.035208 (cit. on pp. 34, 35).

[77] D. Werthmüller et al., *Quasifree photoproduction of η mesons off protons and neutrons*, Phys. Rev. C **90** (1 2014) 015205, URL: https://link.aps.org/doi/10.1103/PhysRevC.90.015205 (cit. on p. 34).

[78] R. Machleidt, *High-precision, charge-dependent Bonn nucleon-nucleon potential*, Phys. Rev. C **63** (2 2001) 024001, URL: https://link.aps.org/doi/10.1103/PhysRevC.63.024001 (cit. on pp. 41, 42, 49).

[79] M. Lacombe et al., *Parametrization of the Paris $N - N$ potential*, Phys. Rev. C **21** (3 1980) 861, URL: https://link.aps.org/doi/10.1103/PhysRevC.21.861 (cit. on p. 41).

[80] M. M. Nagels, T. A. Rijken and J. J. de Swart, *Low-energy nucleon-nucleon potential from Regge-pole theory*, Phys. Rev. D **17** (3 1978) 768, URL: https://link.aps.org/doi/10.1103/PhysRevD.17.768 (cit. on p. 41).

[81] R. B. Wiringa, R. A. Smith and T. L. Ainsworth, *Nucleon-nucleon potentials with and without $\Delta(1232)$ degrees of freedom*, Phys. Rev. C **29** (4 1984) 1207, URL: https://link.aps.org/doi/10.1103/PhysRevC.29.1207 (cit. on p. 41).

[82] J. Groß, *$K^+\Sigma^-$ Photoproduction at the BGO-OD Experiment*, MA thesis: Universität Bonn, 2019, URL: https://www.pi.uni-bonn.de/schmieden/medien/medien-ergebnisse/masterarbeit-johannesgross.pdf (cit. on p. 50).

[83] T. Jude et al., *$K^+\Lambda$ and $K^+\Sigma^0$ photoproduction with fine center-of-mass energy resolution*, Physics Letters B **735** (2014) 112, URL: https://www.sciencedirect.com/science/article/pii/S0370269314004109 (cit. on p. 50).

[84] R. Cecil, B. Anderson and R. Madey, *Improved predections of neutron detection efficiency for hydrocarbon scintillators from 1 MeV to about 300 MeV*, Nuclear Instruments and Methods **161** (1979) 439, URL: https://www.sciencedirect.com/science/article/pii/0029554X79904178 (cit. on p. 51).

[85] Geant4 Collaboration, *G4EmStandardPhysics Class Reference*, URL: https://geant4.kek.jp/Reference/11.3.1/classG4EmStandardPhysics.html (visited on 10/05/2025) (cit. on p. 53).

[86] R. Di Salvo et al., *The GRAAL experiment: Beam polarization asymmetries in pseudoscalar meson photoproduction*, Czech. J. Phys. **49S2** (1999) 43, URL: https://link.springer.com/article/10.1007/s10582-999-0084-6 (cit. on p. 53).

[87] O. Bartalini et al., *Neutron detection efficiency of BGO calorimeter at GRAAL*, Nuclear Instruments and Methods in Physics Research Section A: Accelerators, Spectrometers, Detectors and Associated Equipment **562** (2006) 85, URL: https://www.sciencedirect.com/science/article/pii/S0168900206002269 (cit. on pp. 53, 54, 81, 94).

[88] U.S. Department of Commerce: National Institute of Standards and Technology, *NIST Chemistry WebBook, SRD 69*, URL: https://webbook.nist.gov/chemistry/name-ser/ (visited on 13/01/2025) (cit. on pp. 68, 69).

[89] A. Salam and H. Arenhövel, *Interaction effects in K^+ photoproduction on the deuteron*, Phys. Rev. C **70** (4 2004) 044008, URL: https://link.aps.org/doi/10.1103/PhysRevC.70.044008 (cit. on pp. 75–78, 91).

[90] T. A. Rijken, V. G. J. Stoks and Y. Yamamoto, *Soft-core hyperon-nucleon potentials*, Phys. Rev. C **59** (1 1999) 21, URL: https://link.aps.org/doi/10.1103/PhysRevC.59.21 (cit. on p. 76).

[91] P. M. M. Maessen, T. A. Rijken and J. J. de Swart, *Soft-core baryon-baryon one-boson-exchange models. II. Hyperon-nucleon potential*, Phys. Rev. C **40** (5 1989) 2226, URL: https://link.aps.org/doi/10.1103/PhysRevC.40.2226 (cit. on p. 76).

[92] D. Drechsel, O. Hanstein, S. Kamalov and L. Tiator, *A unitary isobar model for pion photo- and electroproduction on the proton up to 1 GeV*, Nuclear Physics A **645** (1999) 145, URL: https://www.sciencedirect.com/science/article/pii/S0375947498005727 (cit. on p. 76).

[93] S. Alef et al., *$K^+\Lambda$ photoproduction at forward angles and low momentum transfer*, Eur. Phys. J. A **57** (2021) 80, URL: https://doi.org/10.1140/epja/s10050-021-00392-0 (cit. on pp. 79, 80).

[94] A. Martinez Torres, K. P. Khemchandani, U.-G. Meissner and E. Oset, *Searching for signatures around 1920-MeV of a N* state of three hadron nature*, Eur. Phys. J. A **41** (2009) 361, URL: https://doi.org/10.1140/epja/i2009-10834-2 (cit. on pp. 89, 90, 92, 94).

[95] H. Gao et al., *Search for a hidden strange baryon-meson bound state from ϕ production in a nuclear medium*, Phys. Rev. C **95** (5 2017) 055202, URL: https://link.aps.org/doi/10.1103/PhysRevC.95.055202 (cit. on pp. 89, 92).

[96] A. M. Torres, K. P. Khemchandani and E. Oset, *Solution to Faddeev equations with two-body experimental amplitudes as input and application to $J^P = 1/2^+$, $S = 0$ baryon resonances*, Phys. Rev. C **79** (6 2009) 065207, URL: https://link.aps.org/doi/10.1103/PhysRevC.79.065207 (cit. on pp. 90, 92, 94).

[97] D. Jido and Y. Kanada-En'yo, *$K\overline{K}N$ molecule state with $I = 1/2$ and $J^P = 1/2^+$ studied with a three-body calculation*, Phys. Rev. C **78** (3 2008) 035203, URL: https://link.aps.org/doi/10.1103/PhysRevC.78.035203 (cit. on pp. 90, 92, 94).

[98] N.-C. Wei, A.-C. Wang, F. Huang, *Private communication*,
School of Nuclear Science and Technology, University of Chinese Academy of Sciences, 2024
(cit. on pp. 90–92).

[99] D. Skoupil, *Private communication*, Nuclear Physics Institute, Czech Academy of Sciences, 2024
(cit. on pp. 91, 92).

APPENDIX **A**

Obtained Data

W / MeV	$\pm\Delta W$ / MeV	$(\frac{d\sigma}{d\Omega})$ / $\frac{\mu b}{sr}$	$\pm\Delta(\frac{d\sigma}{d\Omega})$ / $\frac{\mu b}{sr}$	$\delta^{\text{Scaling}}_{\text{Syst.}}$ / $\frac{\mu b}{sr}$	$\delta^{\text{Fitting}}_{\text{Syst.}}$ / $\frac{\mu b}{sr}$	$\delta^{\text{Total}}_{\text{Syst.}}$ / $\frac{\mu b}{sr}$
1688.855	6.745	0.00865276	0.00421087	0.00133410	0.00003172	0.00133448
1702.295	6.695	0.03697200	0.00831851	0.00570042	0.00015980	0.00570266
1715.630	6.640	0.03454560	0.00650089	0.00532631	0.00017581	0.00532921
1728.865	6.595	0.03220500	0.00595532	0.00496544	0.00019274	0.00496917
1742.000	6.540	0.04453860	0.00605842	0.00686706	0.00031309	0.00687419
1755.030	6.490	0.04142050	0.00589830	0.00638629	0.00034156	0.00639542
1767.970	6.450	0.05769810	0.00574516	0.00889602	0.00055750	0.00891347
1780.815	6.395	0.06608950	0.00613600	0.01018980	0.00074740	0.01021720
1793.565	6.355	0.06098640	0.00626572	0.00940301	0.00080627	0.00943752
1806.230	6.310	0.07356500	0.00576216	0.01134240	0.00113577	0.01139910
1818.805	6.265	0.05598340	0.00586525	0.00863164	0.00100827	0.00869033
1831.290	6.220	0.08410910	0.00644701	0.01296810	0.00176514	0.01308770
1843.690	6.180	0.08519290	0.00643357	0.01313520	0.00208115	0.01329910
1856.010	6.140	0.10035400	0.00725048	0.01547290	0.00285087	0.01573330
1868.250	6.100	0.10796600	0.00813294	0.01664640	0.00356321	0.01702350
1880.410	6.060	0.10765600	0.00799519	0.01659870	0.00412366	0.01710320
1892.270	5.800	0.12421500	0.00904526	0.01915180	0.00550189	0.01992640
1902.540	4.470	0.15988900	0.01160020	0.02465200	0.00803136	0.02592730
1911.460	4.450	0.17697700	0.01071520	0.02728660	0.00991605	0.02903250
1920.340	4.430	0.17578100	0.01138490	0.02710220	0.01098080	0.02924230
1929.180	4.410	0.17581400	0.01186080	0.02710740	0.01223890	0.02974230
1942.350	8.760	0.16630300	0.00917355	0.02564100	0.01360360	0.02902620

Table A.1: Obtained DCS data for $\gamma n \to K^+\Sigma^-$ in an angular range of $\cos(\theta_{\text{CM}}) > 0.9$. The parameter $\pm\Delta W$ describes half of a bin width, meaning $2 \cdot (+\Delta W)$ is a full bin width. The statistical error $+\Delta(\frac{d\sigma}{d\Omega})$ is equal to $-\Delta(\frac{d\sigma}{d\Omega})$. The total systematic uncertainty is $\delta^{\text{Total}}_{\text{Syst.}} = \sqrt{{\delta^{\text{Scaling}}_{\text{Syst.}}}^2 + {\delta^{\text{Fitting}}_{\text{Syst.}}}^2}$.

APPENDIX B

Flow Diagrams

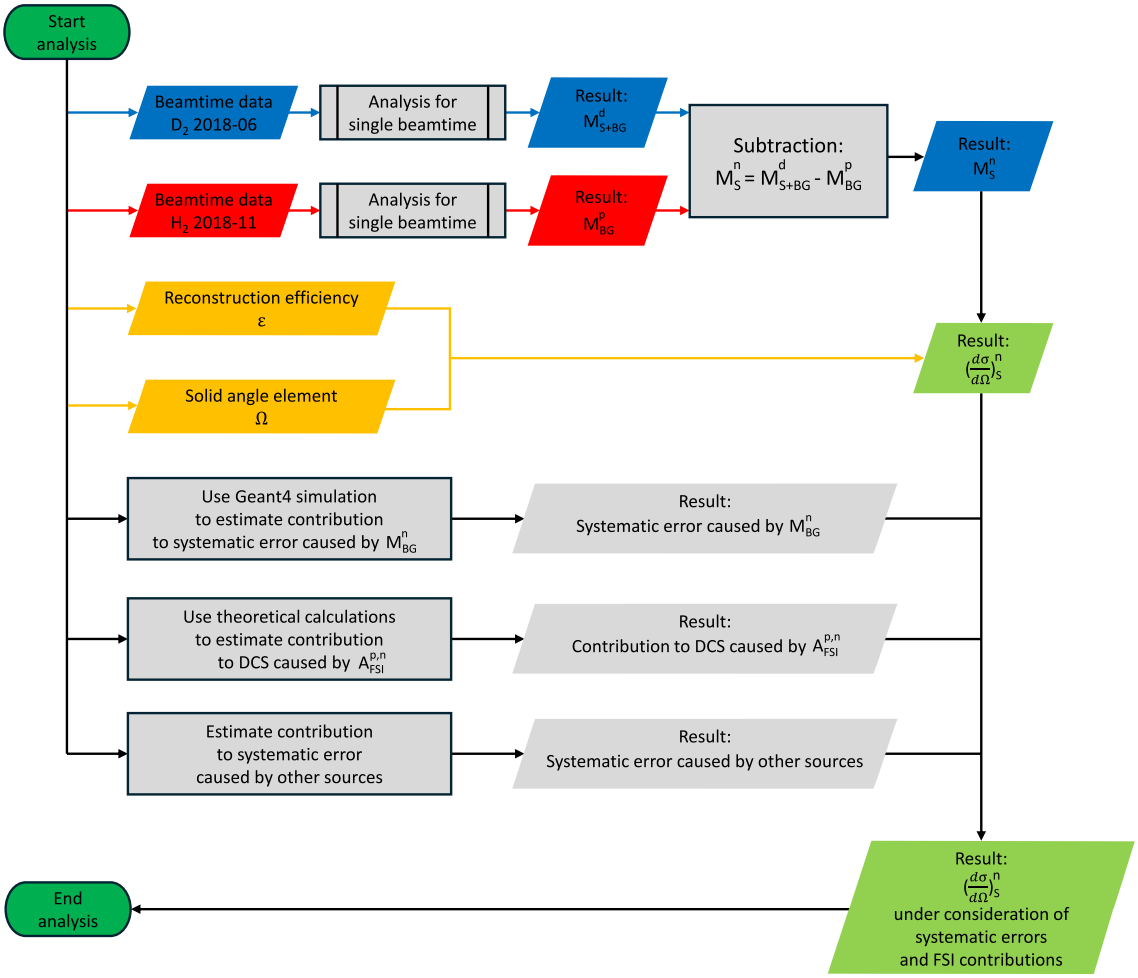

Figure B.1: Flow diagram showing the methodology of the general DCS analysis, starting with the dark green box at the top and ending with the one at the bottom. D_2 data are shown in blue, H_2 data in red and scaling parameters in yellow. Note that the process 'Analysis for single beamtime' is illustrated by another flow diagram, B.2.

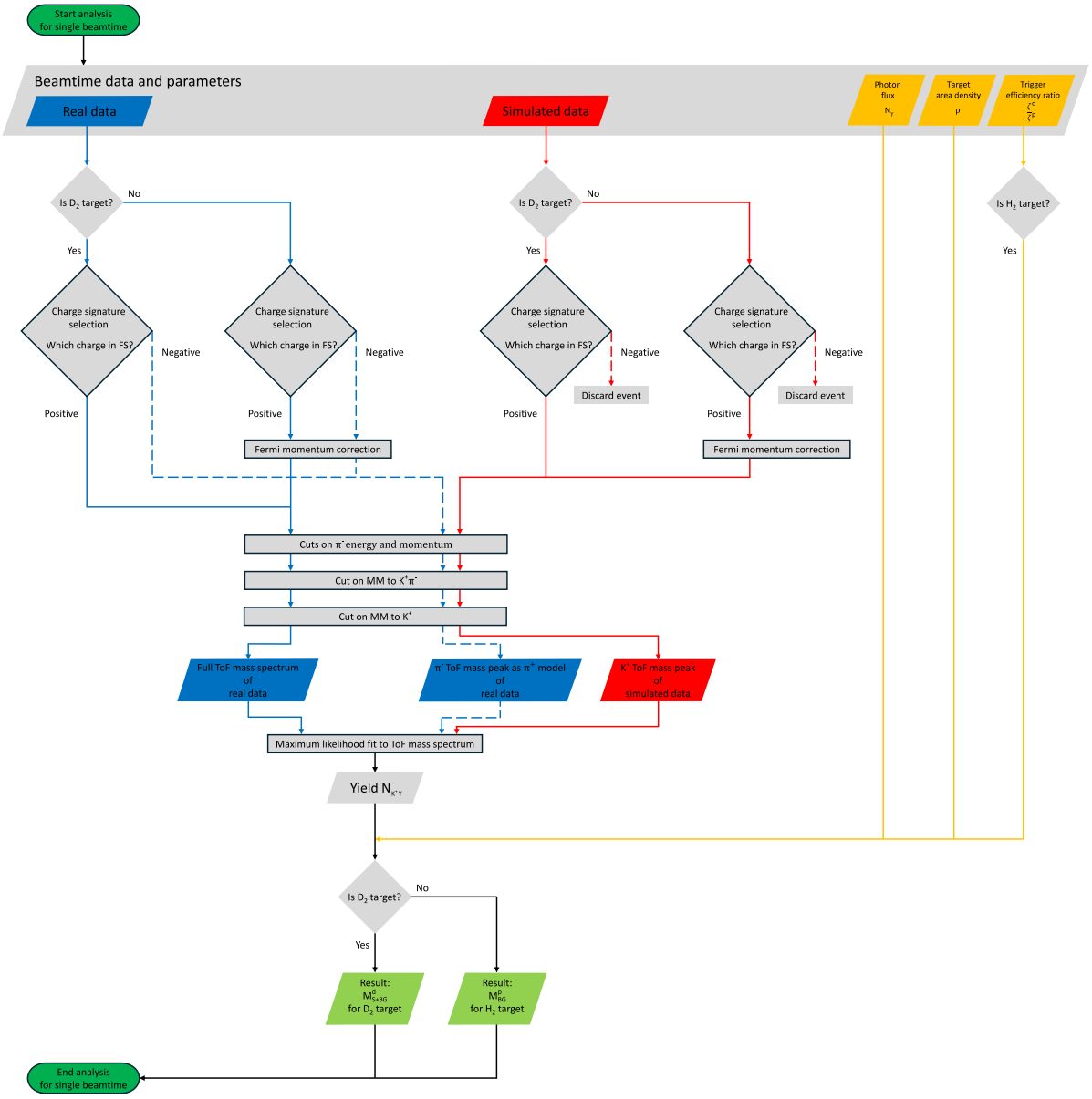

Figure B.2: Flow diagram showing the methodology of the specific DCS analysis of a single beamtime, starting with the dark green box at the top and ending with the one at the bottom. Real data is presented in blue, simulated data in red and scaling parameters in yellow. This flow diagram is referenced by the prior diagram B.1.

APPENDIX C

W Dependency of Selection Criteria

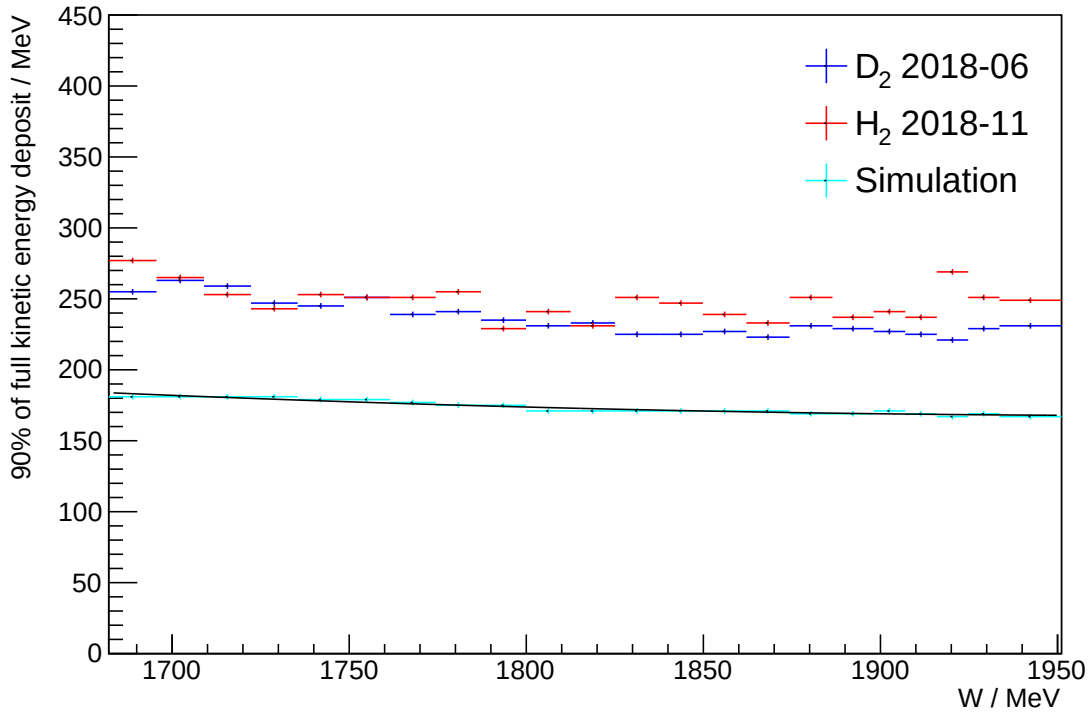

Figure C.1: The cut on the maximum kinetic energy deposit E_{kin} of π^- in the BGO as described in section 4.2.2.2 depending on W. The y-axis describes the kinetic energy at which the cumulative distribution surpasses 90% of its full integral. The difference of real data and simulation is expected due to the background contribution in real data. The black line is a second-degree polynomial fit to the simulated data, which is used to apply the W-dependent cut. The fitted function is of the form: $E_{90\%}(W) = 856.769\,\text{MeV} - 0.693934 \cdot W + 0.000174714 \cdot W^2 \frac{1}{\text{MeV}}$.

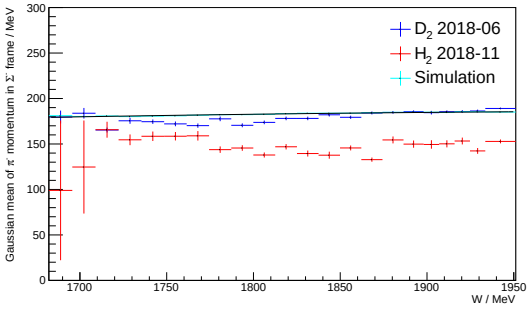

(a) Mean

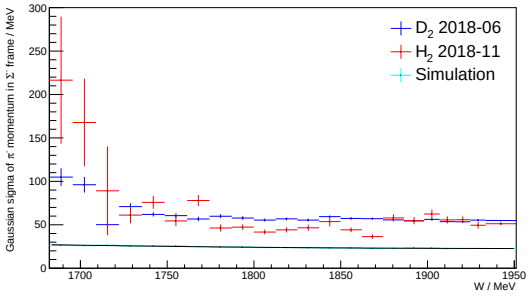

(b) Sigma

Figure C.2: The cut on the momentum of the π^- in the Σ^- frame $|\vec{p}_{\pi^- \text{in } \Sigma^-}|$ as described in section 4.2.2.2 depending on W. Figure (a) shoes the Gaussian mean, figure (b) the sigma. In (a), the difference of the real data sets is expected, as the hydrogen data set only consists of background. In (b), the first bins of the hydrogen data suffer from low statistics. The sigma of the simulated data is much narrower than for the real data, as it consists of pure signal. The black line is a second-degree polynomial fit to the simulated data, which is used to apply the W-dependent cut. The fitted function for the Gaussian mean is of the form: $\mu_{|\vec{p}|}(W) = 8.29125\,\text{MeV} + 0.169588 \cdot W - 4.03871 \cdot 10^{-5} \cdot W^2 \frac{1}{\text{MeV}}$ and the fitted function for the Gaussian sigma of the form: $\sigma_{|\vec{p}|}(W) = 241.547\,\text{MeV} - 0.223395 \cdot W + 5.70059 \cdot 10^{-5} \cdot W^2 \frac{1}{\text{MeV}}$. A 2-$\sigma$ cut is chosen.

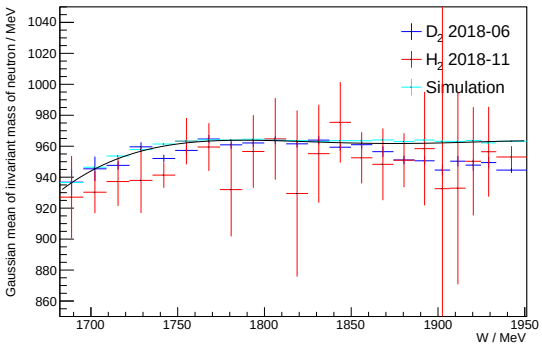

(a) Mean

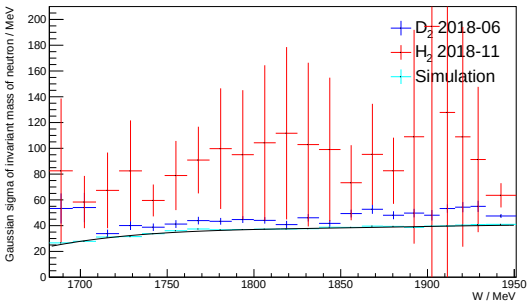

(b) Sigma

Figure C.3: The cut on the MM to $K^+\pi^-$ as described in section 4.2.2.3 depending on W. Figure (a) shoes the Gaussian mean, figure (b) the sigma. The match between the deuterium data and simulation is good and only slightly affected by background. The hydrogen data set suffers from low statistics. The black line is a fourth-degree polynomial fit to the simulated data, which is used to apply the W-dependent cut. The fitted function for the Gaussian mean is of the form: $\mu_{m_n}(W) = -472\,439\,\text{MeV} + 1013.16 \cdot W - 0.812575 \cdot W^2 \frac{1}{\text{MeV}} + 0.00028945 \cdot W^3 \frac{1}{\text{MeV}^2} - 3.86388 \cdot 10^{-8} \cdot W^4 \frac{1}{\text{MeV}^4}$ and the fitted function for the Gaussian sigma of the form: $\sigma_{m_n}(W) = -113\,524\,\text{MeV} + 242.852 \cdot W - 0.194757 \cdot W^2 \frac{1}{\text{MeV}} + 6.94122 \cdot 10^{-5} \cdot W^3 \frac{1}{\text{MeV}^2} - 9.27563 \cdot 10^{-9} \cdot W^4 \frac{1}{\text{MeV}^4}$. A 2-$\sigma$ cut is chosen.

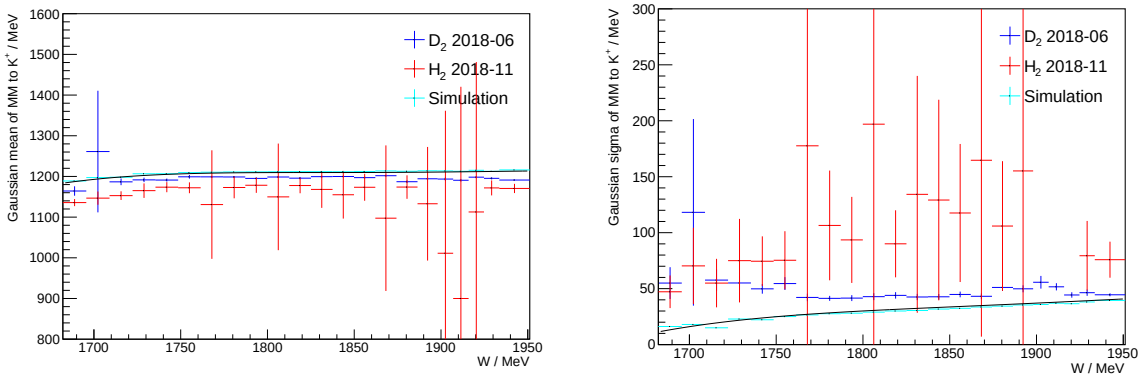

(a) Mean

(b) Sigma

Figure C.4: The cut on the MM to the K^+ as described in section 4.2.2.4 depending on W. Figure (a) shoes the Gaussian mean, figure (b) the sigma. The match between the deuterium data and simulation is good and only slightly affected by background. The hydrogen data set suffers from low statistics, furthermore, the fact that the Λ peak overlaps with the Σ^0 peak affects the fit quality. The black line is a fourth-degree polynomial fit to the simulated data, which is used to apply the W-dependent cut. The fitted function for the Gaussian mean is of the form: $\mu_{\Sigma^-}(W) = -291\,200\,\text{MeV} + 623.365 \cdot W - 0.497999 \cdot W^2 \frac{1}{\text{MeV}} + 0.000176693 \cdot W^3 \frac{1}{\text{MeV}^2} - 2.34915 \cdot 10^{-8} \cdot W^4 \frac{1}{\text{MeV}^4}$ and the fitted function for the Gaussian sigma of the form: $\sigma_{\Sigma^-}(W) = -76\,529.4\,\text{MeV} + 161.102 \cdot W - 0.127154 \cdot W^2 \frac{1}{\text{MeV}} + 4.45985 \cdot 10^{-5} \cdot W^3 \frac{1}{\text{MeV}^2} - 5.86264 \cdot 10^{-9} \cdot W^4 \frac{1}{\text{MeV}^4}$. A 2-$\sigma$ cut is chosen.

APPENDIX D

Fit Results

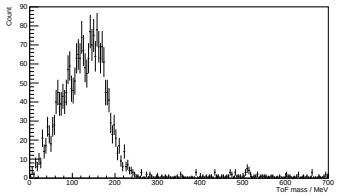

(a) $W = (1\,688.855 \pm 6.745)$ MeV

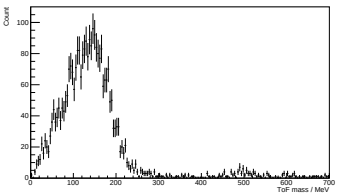

(b) $W = (1\,702.295 \pm 6.695)$ MeV

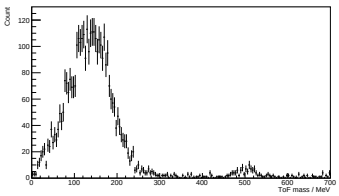

(c) $W = (1\,715.630 \pm 6.640)$ MeV

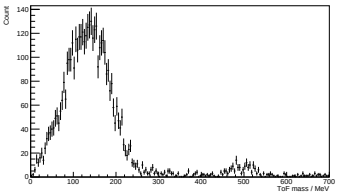

(d) $W = (1\,728.865 \pm 6.595)$ MeV

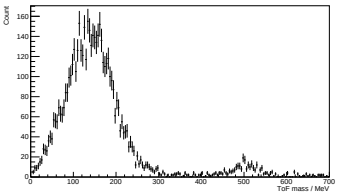

(e) $W = (1\,742.000 \pm 6.540)$ MeV

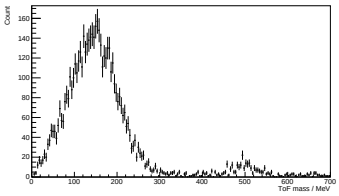

(f) $W = (1\,755.030 \pm 6.490)$ MeV

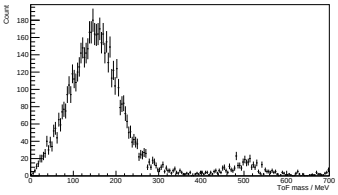

(g) $W = (1\,767.970 \pm 6.450)$ MeV

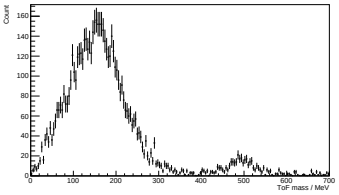

(h) $W = (1\,780.815 \pm 6.395)$ MeV

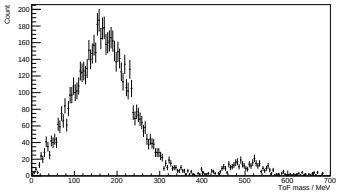

(i) $W = (1\,793.565 \pm 6.355)$ MeV

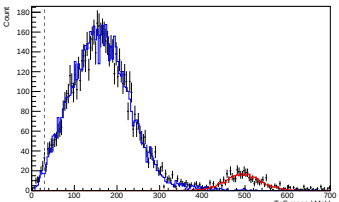

(j) $W = (1\,806.230 \pm 6.310)$ MeV

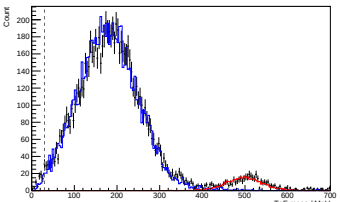

(k) $W = (1\,818.805 \pm 6.265)$ MeV

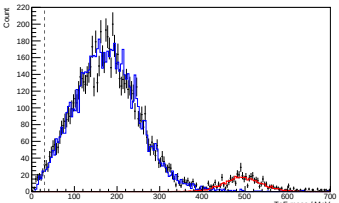

(l) $W = (1\,831.290 \pm 6.220)$ MeV

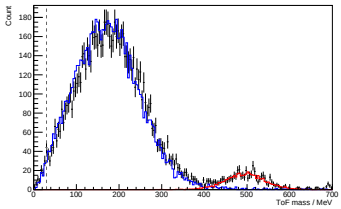

(m) $W = (1\,843.690 \pm 6.180)$ MeV

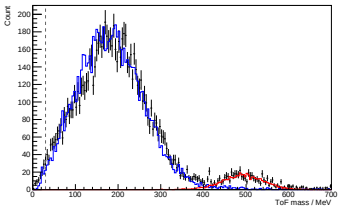

(n) $W = (1\,856.010 \pm 6.140)$ MeV

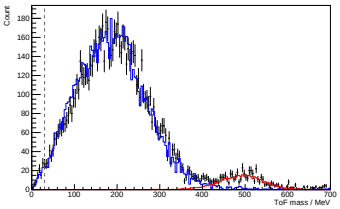

(o) $W = (1\,868.250 \pm 6.100)$ MeV

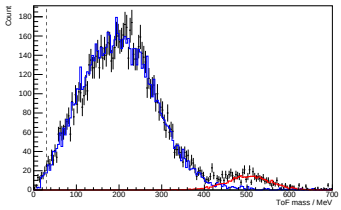

(p) $W = (1\,880.410 \pm 6.060)$ MeV

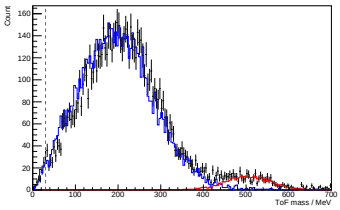

(q) $W = (1\,892.270 \pm 5.800)$ MeV

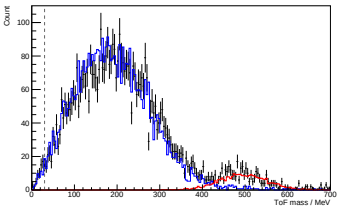

(r) $W = (1\,902.540 \pm 4.470)$ MeV

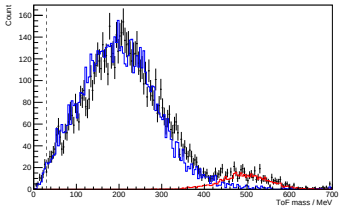

(s) $W = (1\,911.460 \pm 4.450)$ MeV

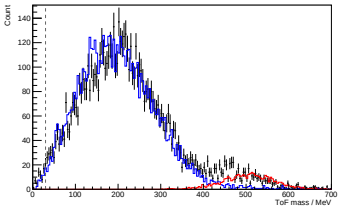

(t) $W = (1\,920.340 \pm 4.430)$ MeV

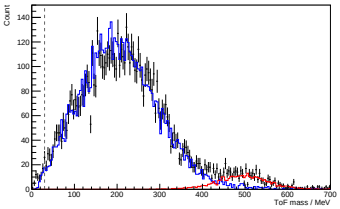

(u) $W = (1\,929.180 \pm 4.410)$ MeV

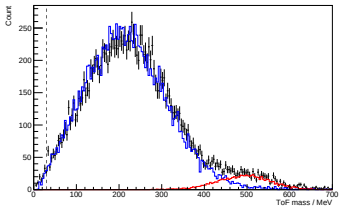

(v) $W = (1\,942.350 \pm 8.760)$ MeV

Figure D.1: Maximum likelihood fit to the ToF mass spectrum of deuterium beamtime 2018-06 for all bins of W. Real data shown in black, fitted π^+ model in blue and simulated K^+ peak in red. Fits become necessary from inclusive $W = 1\,806.230$ MeV on upward. The fitting region is restricted to above 30 MeV as depicted by the vertical line. As the π^+ peak broadens, a distinction of the two peaks gets increasingly harder from $W = 1\,911.460$ MeV on upward. See also figure 4.23.

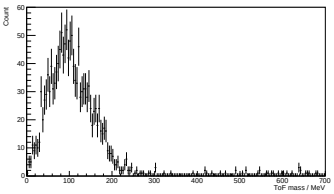

(a) $W = (1\,688.855 \pm 6.745)$ MeV

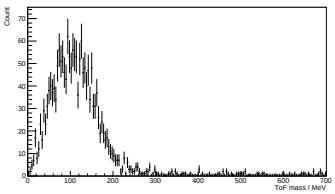

(b) $W = (1\,702.295 \pm 6.695)$ MeV

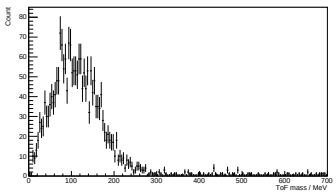

(c) $W = (1\,715.630 \pm 6.640)$ MeV

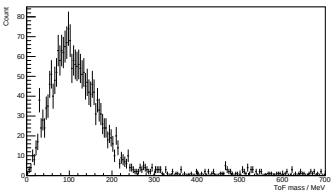

(d) $W = (1\,728.865 \pm 6.595)$ MeV

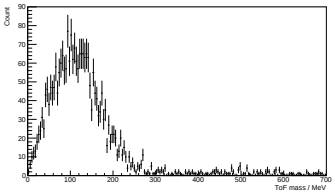

(e) $W = (1\,742.000 \pm 6.540)$ MeV

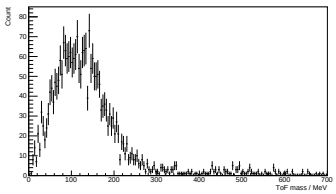

(f) $W = (1\,755.030 \pm 6.490)$ MeV

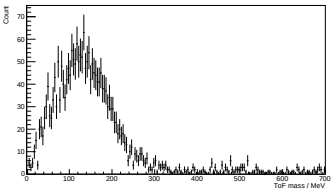

(g) $W = (1\,767.970 \pm 6.450)$ MeV

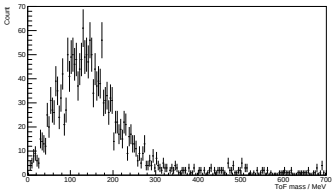

(h) $W = (1\,780.815 \pm 6.395)$ MeV

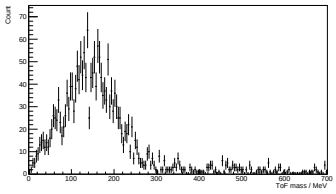

(i) $W = (1\,793.565 \pm 6.355)$ MeV

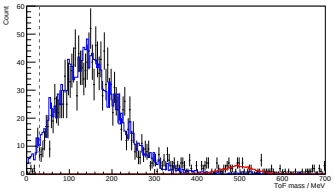

(j) $W = (1\,806.230 \pm 6.310)$ MeV

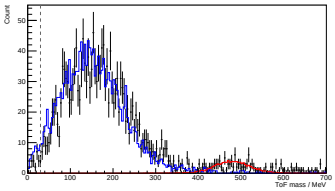

(k) $W = (1\,818.805 \pm 6.265)$ MeV

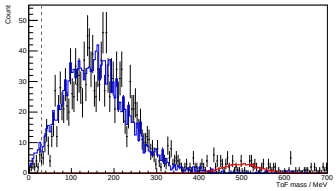

(l) $W = (1\,831.290 \pm 6.220)$ MeV

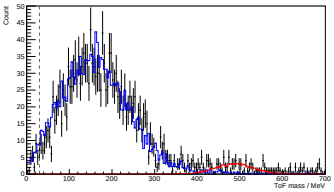

(m) $W = (1\,843.690 \pm 6.180)$ MeV

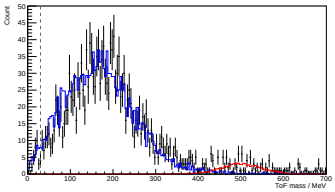

(n) $W = (1\,856.010 \pm 6.140)$ MeV

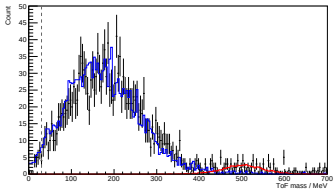

(o) $W = (1\,868.250 \pm 6.100)$ MeV

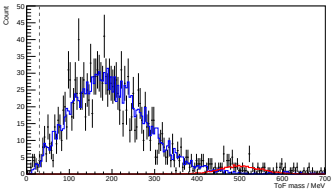

(p) $W = (1\,880.410 \pm 6.060)$ MeV

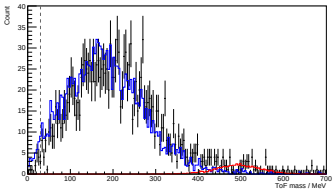

(q) $W = (1\,892.270 \pm 5.800)$ MeV

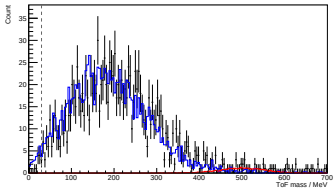

(r) $W = (1\,902.540 \pm 4.470)$ MeV

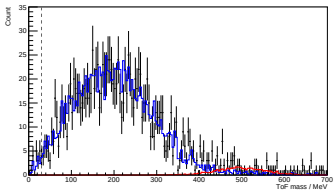

(s) $W = (1\,911.460 \pm 4.450)$ MeV

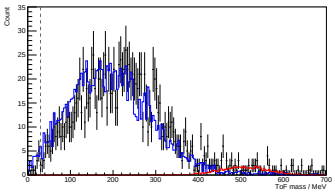

(t) $W = (1\,920.340 \pm 4.430)$ MeV

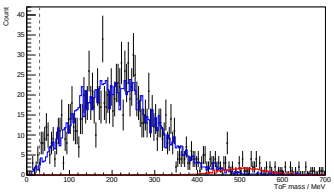

(u) $W = (1\,929.180 \pm 4.410)$ MeV

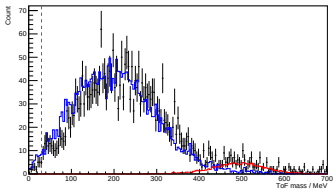

(v) $W = (1\,942.350 \pm 8.760)$ MeV

Figure D.2: Maximum likelihood fit to the ToF mass spectrum of hydrogen beamtime 2018-11 for all bins of W. Real data shown in black, fitted π^+ model in blue and simulated K^+ peak in red. Fits become necessary from inclusive $W = 1\,806.230$ MeV on upward. The fitting region is restricted to above 30 MeV as depicted by the vertical line. As the π^+ peak broadens, a distinction of the two peaks gets increasingly harder from $W = 1\,911.460$ MeV on upward. As expected, the K^+ peak is much smaller compared to the deuterium beamtime. See also figure 4.24.

List of Figures

List of Tables

Acknowledgements

I thank Prof. Dr. Hartmut Schmieden for his trust in my capabilities to perform an analysis of such a complex scientific problem and for entrusting me with the role of technical coordinator of the BGOOD experiment.

Furthermore, I thank all members of the BGOOD collaboration who gave me advice during the time of writing.

Special thanks go to Dr. Georg Scheluchin and Dr. Oliver Freyermuth for sharing their vast knowledge of hardware and software with me and even caring about the experiment after officially having left the collaboration, sometimes even at three o'clock in a Saturday night.

Last but not least, I thank the ELSA staff who worked tiredlessly to provide BGOOD with stable beam conditions.